Host-guest chemistry pretargeted positron emission tomography

By

Vilma Inkeri Jarintyttö Jallinoja

Dissertation

Submitted to the Faculty of the

Graduate School of Vanderbilt University

in partial fulfillment of the requirements

for the degree of

DOCTOR OF PHILOSOPHY

in

Chemical and Physical Biology

December 17th, 2022

Nashville, Tennessee

Approved:

Todd Peterson, Ph.D.

Rizia Bardhan, Ph.D.

Marjan Rafat, Ph.D.

Charles Caskey, Ph.D.

ACKNOWLEDGMENTS

TABLE OF CONTENTS

LIST OF TABLES

LIST OF FIGURES

LIST OF ABBREVATIONS

ACN; acetonitrile

Adma; adamantane

CB[n]; cucurbit[n]uril

CA; clearing agent

DCM; dichloromethane

DMSO; dimethyl sulfoxide

DNA; deoxyribonucleic acid

DOL; degree of labeling

eq.; equivalent

ESI; electrospray ionization

Fc; crystallizable fragment region

Fc; ferrocene

[^{18}F]FDG; ^{18}F-fluorodeoxyglucose

FL; fluorescein

FPLC; fast protein liquid chromatography

^{1}H-NMR; proton nuclear magnetic resonance

HRMS; high-resolution mass spectrometry

IEDDA; inverse electron demand Diels-Alder

IgG; immunoglobulin G

mAb; monoclonal antibody

MeOH; methanol

MIP; maximum intensity projection

MORF; morpholino oligomer

NaOH; sodium hydroxide

PBS7.4; Phosphate buffered saline, pH=7.4

PET; positron emission tomography

p.i.; post injection

PNA; peptide nucleic acid

RCP; radiochemical purity

RCY; radiochemical yield

RIT; radioimmunotherapy

RNA; ribonucleic acid

RP-HPLC; reverse phase high performance liquid chromatography

rpm; rounds per minute

RT; room temperature

SEC; size exclusion chromatography

%ID/g; percentage of injected dose per gram

1. INTRODUCTION

The goal of this work was the development of a host-guest chemistry pretargeting platform for positron emission tomography (PET). Pretargeting is an alternative technique of using macromolecules (e.g. monoclonal antibodies; mAbs and nanoparticles) in nuclear imaging and therapy to reduce to overall radiation dose, which is commonly high with the use macromolecules relative to small molecule radiopharmaceuticals. Traditionally in macromolecule-based nuclear medicine, the macromolecule is directly radiolabeled with a relatively long-lived radionuclide to match the long biological half-life of the macromolecule. Unfortunately, this often leads to dose limiting toxicities (*e.g.* hematopoietic toxicity) which has been a major hindering component in using macromolecules in clinical setting, despite of their many exceptional attributes such as the extremely high target specificity of mAbs.

Pretargeting is a two-step strategy which involves first the administration of a bio-targeting macromolecule followed by an injection of a radiolabeled small molecule, radioligand which is designed to radiolabel the macromolecule *in vivo via* specific interaction occurring between these two "bioorthogonal" agents. The previously studied pretargeting methodologies all lack either in stability, modularity or biocompatibility of the pretargeting agents and there remains an unmet need for an efficient and a widely applicable pretargeting technology.

We hypothesized that utilizing host-guest complexation as the specific pretargeting interaction is the ideal approach for performing pretargeted nuclear medicine. More specifically we investigated the use of two different high affinity host-guest pairs, cucurbit[7]uril-ferrocene and cucurbit[7]uril-adamantane. Both guest ligands, ferrocene

and adamantane possess high association constants towards the cucurbit[7]uril host molecule.

The first aim was to develop the pretargeting agents: we synthesized a cucurbit[7]uril host molecule conjugated carcinoembryonic antigen (CEA) targeting antibody to serve as the primary, macromolecule agent and a library of radiolabeled ferrocene and adamantane guest molecules which would act as the radioligand candidates. The aim included the characterization of the modified antibody and guest radioligands to establish their potential for future *in vivo* studies. The family of radioligands was synthesized with the goal of optimizing the pharmacokinetic profile of the radioligand to result in the best pretargeting performance.

The second aim involved first comparing the radioligands' *in vivo* profile in healthy mice and study the biodistribution of the chosen CEA targeting antibody in tumor bearing mice. The efficacy of the proposed pretargeting system was examined in tumor bearing mice for pretargeted PET by assessing the *in vivo* profile of the different guest radioligands along with the cucurbit[7]uril modified antibody. This was examined with *in vivo* biodistribution, PET imaging and dosimetry studies.

Based on the presented work the host-guest chemistry driven pretargeting strategy results in specific and high target uptake and high-quality PET images of the pretargeted antibody. The robustness, modularity and efficacy of the examined methodology provides an excellent strategy for antibody-based nuclear medicine and holds a lot of potential for improving the future landscape of clinical pretargeting technologies.

2. LITERATURE

2.1 ANTIBODY BASED NUCLEAR MEDICINE

Ever since the discovery of antibodies in the late nineteenth century as "magic bullets" with high specificity towards a specific agent was understood, there has been great interest in understanding their role in the immune system. However, it was the first successful production of mAbs in 1975 that provided a pathway to utilize antibodies in clinical applications in a meaningful and precise manner.[1] The origin of radioimmunoimaging and radioimmunotherapy (RIT) occurred soon after, in the late 1970s, with the first immunoimaging studies in humans exploring the use of an ^{131}I-labeled CEA targeting immunoglobulin G (IgG) as a diagnostic tool to locate cancer tissues of varying origins.[2,3] Deploying antibodies with high target specificity (K_d ~ 1-10 nM) together with the tools of radiochemistry, detailed information on the expression and location of disease specific antigens can be discovered non-invasively and as therapeutic agents antibodies can be utilized as vectors to deliver toxic radiation to cancer tissue. So far radioimmunoimaging has been applied to the imaging of many biological targets including, for example, cancer tissue, the immune system, infections, and inflammation.[4] The growing number of clinically approved new antibody therapeutics and the increasing number and accessibility to relatively long-lived radionuclides have accelerated the exploration of radiolabeled antibodies in the clinics. However there are certain inherent challenges associated with the use of radiolabeled antibodies, which have factored in the number of clinically approved antibody agents in nuclear medicine. mAbs are relatively large in size (150 kDa) which results in them possessing long biological half-lives.

3

Additionally, the crystallizable fragment (Fc) portion of the antibody construct, which negates the interaction with the neonatal Fc receptor, further elongates the biological half-life of full-length antibodies. (**Figure 1**) These two factors result in full-length antibodies possessing biological half-lives varying from 6 to even 31 days in human.[5] The long resident time of these macromolecules in the blood pool unfortunately results in high radiation doses in the healthy tissue which is a major limitation for the use of directly radiolabeled antibodies. Due to the intrinsic radiosensitive nature of bone barrow tissue, hematological toxicity is the most common dose limiting factor of an antibody-based radiopharmaceutical.[6]
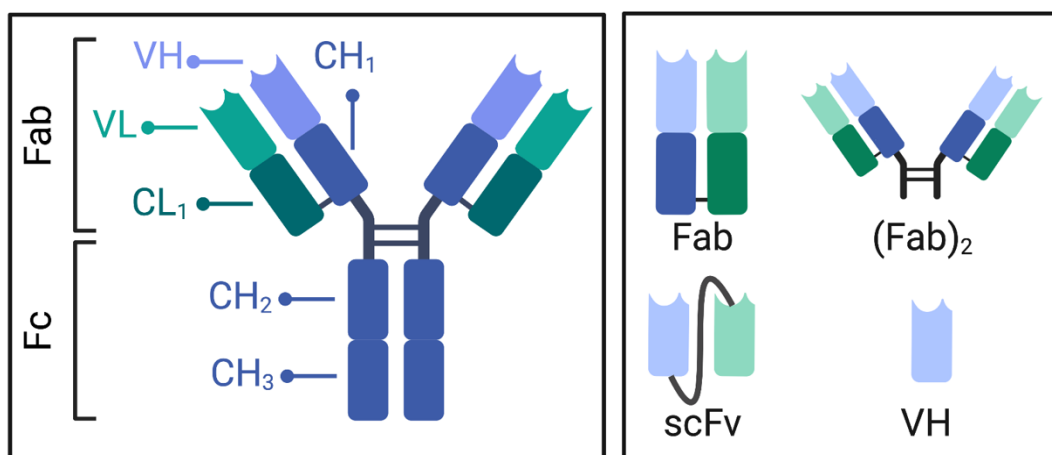
Figure 1. Structures of a full-length IgG antibody and antibody fragment types.

2.1.1 Methodologies

Antibodies and their fragments

Out of all antibody types, IgG is the most common antibody construct studied in nuclear medicine due to the molecule's perfect balance of target uptake and clearance time.[7] There are two main categories of IgG based constructs that are currently explored, full-

length IgG molecules and antibody fragments. Full-length antibodies consist of two heavy and two light chains that are bound together via disulfide bonds. The IgG molecule can also be considered to consist of two antigen binding regions (Fab) and the Fc region, which results in a molecular weight of ~150 kDa. As the name implies, antibody fragments consist of only a part of the full-length IgG molecule. The molecular weight of antibody fragments varies (15-100 kDa) due to the vast difference in the number of different components the fragment may be constructed of. Most often, the Fc region is excluded from the antibody fragments to avoid its interaction with the neonatal Fc receptor and achieve the desired pharmacokinetic profile.
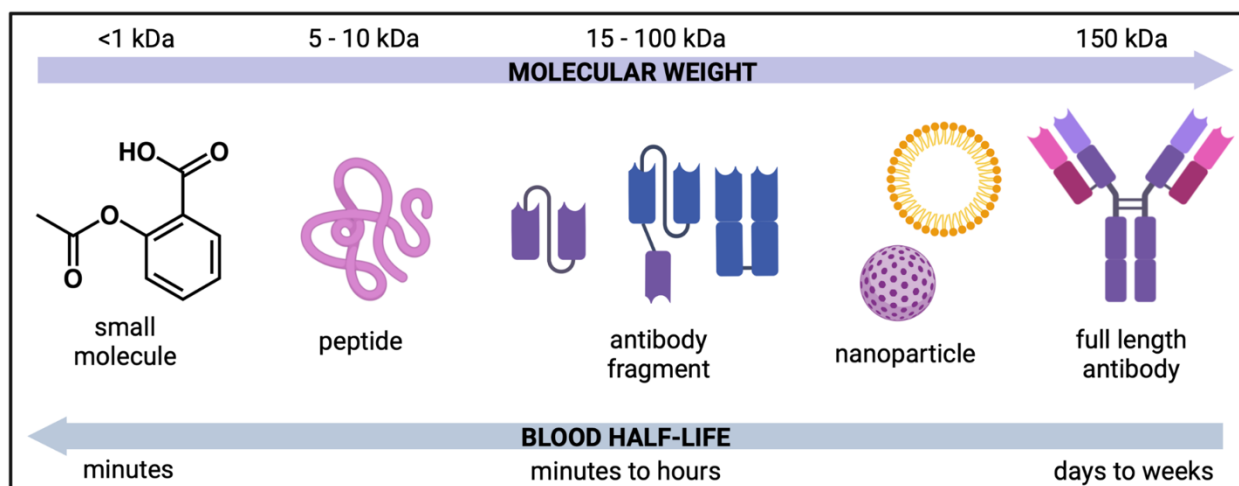
Figure 2. The blood half-life of different biologically active compound types with varying molecular weights.

The two main consequences the difference in the molecular weight has on the biological behavior of full-length antibodies and their fragments is in their blood half-life and route of excretion.[8] Generally, the larger the molecule is in its molecular weight, the longer it is

retained in the blood pool. (**Figure 2**) One of the main appeals of radiolabeled antibody fragments is their faster blood clearance that results in lowered whole-body radiation doses, which is the main toxicological concern when using full-length antibodies. As the smaller antibody agent exits the blood pool faster, it results also in lowered tumor uptake which could be a hindering element for using fragmented antibodies for RIT. An additional challenge for RIT with antibody fragments (<60 kDa) is their renal excretion, often resulting in high kidney uptake which can be a dose limiting factor due to the radiosensitivity nature of kidneys. However there are efforts in adjusting the excretion profile of antibody fragments. A recent clinical trial demonstrated that modifying an [124]I-labeled diabody (55 kDa) with PEG-linkers, resulted in lowered kidney retention and the imaging construct proved to be safe and effective agent for imaging of glycoprotein 72 positive cancers.[9]

Conjugation strategies

With most radionuclides, the radiolabeling of an antibody occurs indirectly. The biomolecule is first modified with a bifunctional metal chelator by amide, thiourea or thiol couplings followed by the radiolabeling. The most commonly utilized reactive conjugation sites of an antibody are the lysine amino acid residues and the free thiol groups that are exposed after reducing the disulfide bonds between the two heavy chains. The free amines and thiols are then reacted with bifunctional chelator modified with moieties of carboxylic acids, activated esters, isothiocyanates or maleimides.[10] (**Figure 3**)
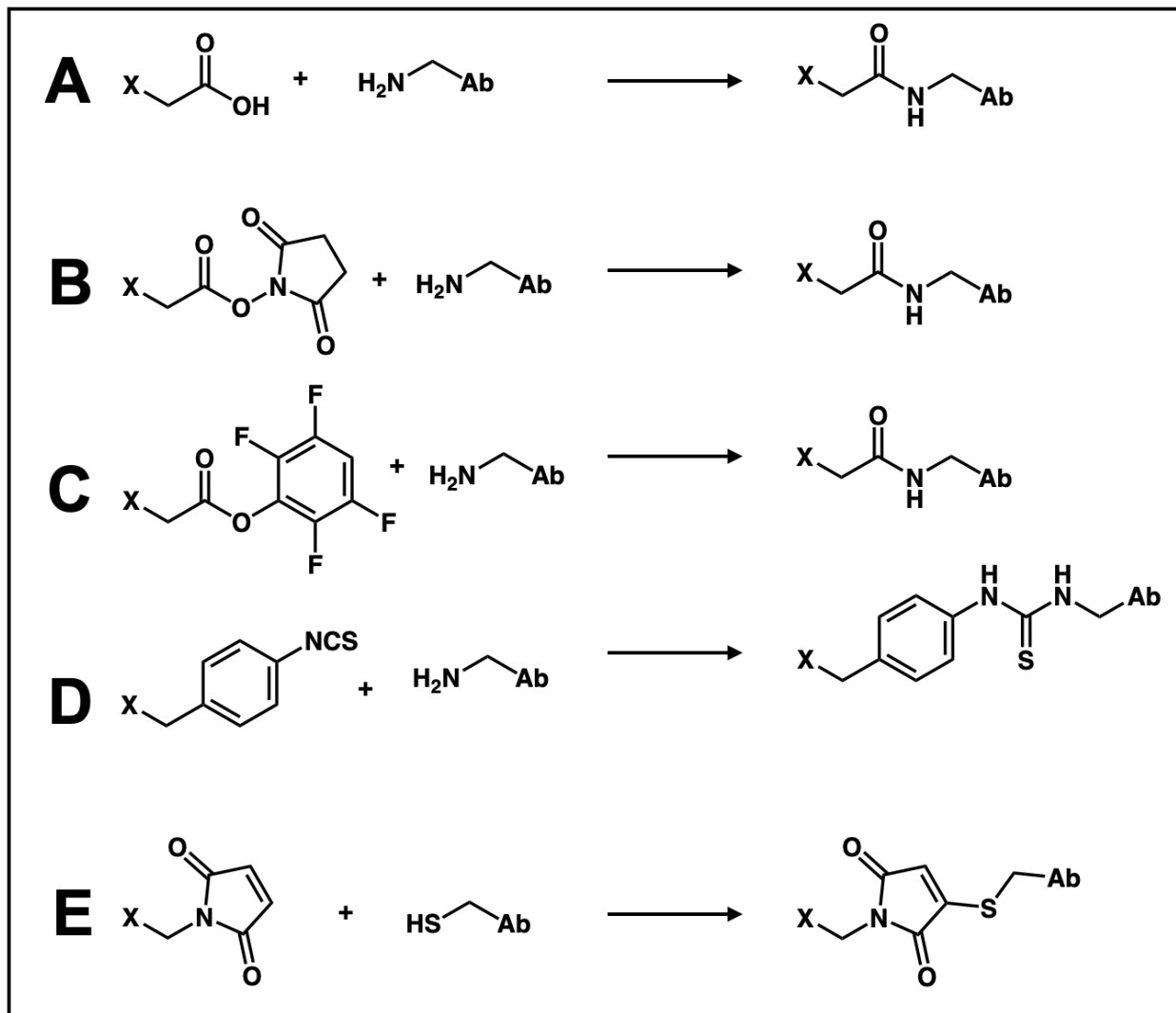
Figure 3. The commonly used bioconjugation reactions for antibody modifications. Coupling of lysine amino acid residue with a carboxylic acid (**A**), an N-hydroxysuccinimide ester (**B**), a tetrafluoro phenyl ester (**C**) or an isothiocyanate (**D**) or a reaction of free thiol with maleimide (**E**). Ab; antibody, X; conjugate such as a metal chelator.

The lysine based bioconjugation methods are considered non-site specific. (**Figure 3A-D**) In theory, the covalently coupled modification can be conjugated to any of the available

lysine residues on the antibody molecule, which could result in compromised immunoreactivity of the antibody in the event the conjugation occurs at the antigen binding region. The cysteine-based conjugation approach is an example of a site-selective conjugation method due to the orderly location of the 4-8 cysteine residues in each antibody. (**Figure 3E**) There are several reported site-specific conjugation approaches. These types of approaches were developed because they have the potential to achieve similar or higher degrees of labeling than direct labeling strategies while minimally impacting the immunoreactivity of the agent. Furthermore, they may produce more well-defined constructs owing to the reproducibility and specificity with respect to the number and location of conjugated moieties.[11,12] One example of an enzyme mediated site-specific antibody conjugation approach involves modifying the antibody first *via* oligosaccharide chains located at the CH2 region of the antibody.[13] The oligosaccharides are first reacted enzymatically with an azide functionalized monosaccharide. The covalently bonded azide moiety is then reacted further with the desired chemical groups. Due to their smaller size, the bioconjugation of antibody fragments *via* site-specific strategy is especially relevant. In general, there is evidence that targeting with either full-length or fragmented antibodies, better *in vivo* performance is acquired by modifying the constructs site-specifically.[14-16]

Radiolabeling strategies

The common factor with the radionuclides used in immunoimaging and RIT is their relatively long physical half-life of several days. (**Table 1**) The long biological half-life of an antibody is matched with a radionuclide with a similar physical half-life in order to

monitor the *in vivo* profile of the macromolecule over the course of its residence time in the whole body. The radionuclides used can be divided into radiometals and different radioisotopes of iodine. At this point, there are several kinds of therapeutic radionuclides with varying decay profiles that have been heavily investigated for RIT. The alpha-emitters are a later addition to the pool of available radionuclides for RIT, and due to their higher linear energy transfer (80 keV/mm) and shorter pathlength (0.04-0.1 mm) compared to those of the beta-emitters (0.2 keV/mm and 0.05-12 mm) they hold a lot of potential and interest in the field of RIT.[17]

Table 1. Commonly investigated radionuclides for antibody based nuclear medicine.

radionuclide	half-life	mode of decay	utilization
indium-111	2.8 d	γ	SPECT
zirconium-89	3.3 d	β^+	PET
copper-64	13 h	β^+	PET
yttrium-90	2.7 d	β^-	therapy
lutetium-177	6.7 d	β^- & γ	therapy, SPECT
actinium-225	10 d	α	therapy
iodine-124	4.2 d	β^+	PET
iodine-131	8.0 d	β^-	therapy

Radioiodination can be performed either through electrophilic or nucleophilic reaction in one step approach. However, radiolabeling with radiometals is always a two-step process which often involves conjugation the antibody first with a radiometal chelator, which is then radiolabeled. Another approach is to first radiolabel a bifunctional chelator which is later conjugated to the antibody. The latter strategy is mostly only used when the chosen metal chelator requires the use of high temperatures for the radiolabeling procedure.[18]

Whatever radionuclide or radiolabeling approach is used to synthesize a radiolabeled antibody certain labeling conditions need to be met: Antibodies being biological molecules with a highly meticulous three-dimensional structure defined by the intra- and intermolecular interactions between the amino acid residues, these macromolecules maintain their biological activity only if they are kept in certain temperature (<40 °C) and pH range (pH 5-9). The increasing interest in applying antibodies in nuclear medicine has also accelerated the research on developing new metal chelators able to radiolabel radiometals rapidly in room temperatures.[10]

2.1.2 Clinical use in cancer treatment

Despite the high medical potential antibodies possess in nuclear medicine due to their high target specificity there are several obstacles these agents have faced in their clinical studies. For immunoimaging and RIT most of the challenges stem from the slow pharmacokinetics of the full-length antibody molecules. For diagnostic applications the major drawback is non-sufficient tumor-to-background ratio due to not high enough antigen expression at the target site and high background signal from non-tumor tissue such as liver. Moreover, with the slow target accumulation of full-length antibodies and the long presence of the radioactivity in the body, multiple scans in a short time period are not easily feasible.[19] Despite the vast number of clinical trials on different directly radiolabeled antibodies for instance for cancers of gastric, colorectal, breast, prostate and pancreas, so far there have been only a few clinically approved agents for immunoimaging. In the 1990s five [111]In- and ^{99m}Tc-labeled full-length antibodies and antibody fragments were FDA approved as single photon emission computer tomography

imaging agents for cancers of varying origins.[20] The production of all of these imaging agents was eventually discontinued due to the lack of their efficacy and sensitivity. For example the TAG-72 targeting ^{111}In-labeled murine mAb Oncoscint was pulled from clinical use due to better efficacy with ^{18}F-fluorodeoxyglucose ([^{18}F]FDG).

Nowadays one of the primary roles of immunoimaging is as a complementary tool for RIT. Many of the current clinical trials of directly radiolabeled antibodies are primarily examined for targeted radiotherapy and include the use of diagnostic antibodies only in conjunction with its therapeutic analog. For instance, a prostate specific membrane antigen targeting ^{111}In-J591 antibody is investigated in a phase 2 study as a diagnostic tool for its therapeutic pair, ^{177}Lu-J591 for prostate cancer treatment (NCT00859781). In another current example, for the treatment of kidney cancer a carbonic anhydrase IX targeting [89]Zr-girentuximab is studied as part of phase 2 clinical trial as the diagnostic pair for ^{177}Lu-girentuximab (NCT05239533).

The success of RIT in human use has proven to be very dependent on the expression profile of the target antigen and the radiosensitivity of the tumor tissue. For these reasons, treatment of hematological cancers such as leukemia and lymphoma with radioimmunotherapy has demonstrated to result in high rate of complete remissions and duration of response.[6] Several excellent antigen targets have been established, such as CD20, CD22 and HLA-DR, which are expressed only in a small number of non-target healthy tissue but highly expressed in B cell lymphomas. So far, the only two FDA approved directly radiolabeled antibodies for targeted radiotherapy are ^{131}I-tositumomab and ^{90}Y-ibritumomab which both target CD20 and are meant for the treatment of relapsed

B cell malignancies. ^{131}I-tositumomab was later withdrawn in 2014 from clinical production due to its limited use.

Notoriously RIT has shown to result in clinical response only in patients with certain non-solid tumors. Over three decades of clinical RIT studies of solid tumors have consistently shown to be unsuccessful. This is partly due to the higher radioresistance of solid tumor tissue. Additionally a five to ten-fold radiation doses (3500-10 000 cGy) are required for a clinical response in solid tumors due to the tumor mass' larger size. This often leads to the therapeutic index to be insufficient due to the dose limiting toxicities. In the case targeted radiotherapy, therapeutic index is defined as the amount of radiation dose delivered to the tumor to the dose received by the radiosensitive tissue. Additionally for certain solid tumors, such as pancreas, prostate and colon, the tumor tissue is often located in areas of poor accessibility for the antibody to get accumulated in high enough amounts when intravenous dosing of the agent is used. The most success with RIT of solid tumors is seen when the radioimmunoconjugate is administered directly into the compartment where the tumor tissue is located. This approach is of course limited to only certain types of cancer cases such as malignant brain tumors (intrathecal administration).[21,22] The radiation doses received with intra-compartmental injection are usually ten times as high compared to intravenous injections.[6]

Two approaches have been proposed to address the problems facing clinical translation of antibody based nuclear medicine applications: antibody fragments and pretargeting. Due to the faster clearance of the antibody fragments from the blood pool they could potentially lead to better tumor-to-background ratios. Additionally, antibody fragments have demonstrated higher penetration of the tumor tissue compared to full-length

antibodies, which again, could improve the therapeutic response. However, antibody fragments have lower target accumulation and shorter target retention times compared to full-length antibodies, which could potentially hamper their clinical use. Additionally the molecular weight of antibody fragments under 60 kDa directs their excretion to occur *via* the renal system potentially leading to dose limiting kidney toxicities. In the case of slow renal excretion, this could especially hamper the clinical use of antibody fragments for targeted radiotherapy where the physical half-life of the used radionuclides tends to be several days.

Pretargeted nuclear medicine is another alternative approach which could address the challenges currently existing in the field of immunoimaging and radioimmunotherapy. Since pretargeting leads to more rapid delivery of the radiation source to the target site and faster excretion of the unbound radioligand, larger doses could theoretically be administered with pretargeted radioimmunotherapy with substantially reduced hematological toxicities. Additionally with the pretargeting approach and with the use of antibody fragments, shorter imaging protocols could be applied making these alternative approaches more suitable for clinical use.

On average, more than ten new cancer antibody therapeutics enter late-stage clinical trials every year.[23] As the role of antibodies in cancer therapeutics increase, the potential for using antibody-based nuclear medicine agents in profiling patients' tumor antigen landscape to predict therapeutic response becomes consequential and significant. The approval rate of directly radiolabeled antibodies for clinical use has been low with less than ten FDA approved radioimmunoconjugates in total, with only one of them still being in clinical production. According to a survey done by Schaefer et al. in the United States,

one of the bigger concerns for oncologists and hematologists in the use of one of the clinically approved radioimmunoconjugates, ^{131}I-tositumomab, is the possible bone marrow damage that could preclude patients from further therapy.[24] As our understanding of how to effectively implement pretargeted technologies and antibody fragment nuclear medicine expands, the preclinical data strongly suggests these types of toxicities can be avoided, alleviating some of the concerns of physicians that want to utilize these strategies in the clinic.

2.2 PRETARGETED NUCLEAR MEDICINE

Pretargeted nuclear medicine is an alternative strategy for macromolecule based nuclear imaging and therapy, with the aim to reduce the high whole-body radiation dose commonly associated with the use of directly radiolabeled macromolecules.[25,26] As discussed previously, due to the large size of macromolecules (e.g. full-length mAbs, nanoparticles), they possess slow pharmacokinetics and long biological half-lives. Upon using directly radiolabeled macromolecules as targeting vectors in nuclear medicine, the slow target accumulation results in unnecessary radiation to the healthy tissue. This excess radiation dose is especially harmful to radiation sensitive tissue, such as bone marrow. As a result of this, despite the high specificity mAbs possess as targeting tools, the dose limiting hematopoietic toxicity has hindered the clinical approval and use of these agents in the clinics.[6,27]

2.2.1 Concept

Pretargeting approach evades the high radiation dose of macromolecule driven nuclear medicine by radiolabeling the macromolecule with a small molecule (radioligand) only once it is bound at the target site. The *in vivo* radiolabeling of the macromolecule occurs *via* highly specific interaction in a bio-orthogonal fashion between the macromolecule and the radioligand. Pretargeting procedure includes four steps (**Figure 4**): Administration of the modified macromolecule (1), allowing the macromolecule to accumulate to the target site and be excreted from the non-target tissue over several days (2), administration of the macromolecule targeting radioligand (3), allowing the radioligand to accumulate to the target, bind or react with the antibody and be excreted from the non-target tissue within hours (4). Based on preclinical and clinical studies, pretargeting offers lower total body radiation doses compared to the use of conventional directly radiolabeled macromolecules.[28-31] This *in vivo* radiolabeling of the macromolecule results in lower whole-body radiation due to the fast pharmacokinetics of the small molecule which in turn enable the use of short-lived radionuclides which minimize the radiation dose further. The radionuclide being used is chosen based on the biological half-life of the targeting molecule. This means, for conventional macromolecule-based imaging radionuclides such as zirconium-89 ($t_{1/2}$= 3.3 d) and iodine-124 ($t_{1/2}$= 4.2 d) are commonly used. (**Table 1**) However, with pretargeting which utilizes small molecules, the molecule can be radiolabeled with radionuclides which possess half-lives of only hours, such as fluorine-18 ($t_{1/2}$= 110 min) and gallium-68 ($t_{1/2}$= 68 min).

The length of the lag time between the administration of the macromolecule and radioligand agent plays a vital role of the pretargeting scheme. The lag time is determined

based on the blood half-life of the macromolecule being used. In the case of full-length antibodies, the biological half-life in human varies between 6-30 days.[5] The lag time needs to be long enough, usually >3 days, for most of the antibody to be excreted from the non-target tissue, specifically the blood, to avoid the radioligand from binding to the non-target bound antibody still circulating in the blood pool. To shorten the needed lag time, clearing agents (CA) of the antibodies have been extensively explored.[32-35] CA is administered after the macromolecule injection, usually at least 24 h post injection. The purpose of CA is to interact with the unbound modified macromolecule in the blood pool and transport it to either the liver or spleen. The use of a CA has shown to significantly reduce the amount of macromolecule in the blood stream, which then again reduces the undesired radioligand-macromolecule interaction in the blood pool. The CA consists of two components, a moiety which interacts with the modified macromolecule and a construct, such as polystyrene bead coated albumin or galactose albumin, which delivers the CA bound macromolecule to liver or spleen.[34]
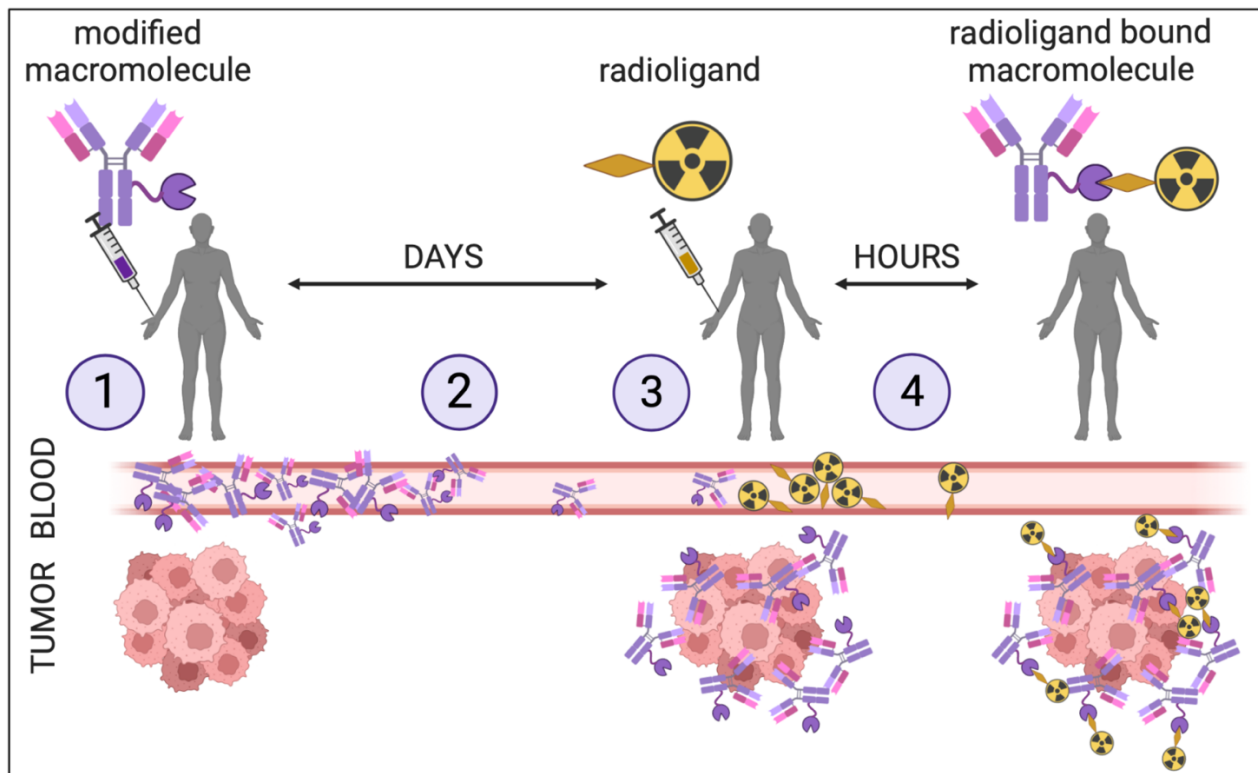
Figure 4. Illustration of the four steps of the pretargeting approach. The administration of the modified molecule such as a full-length antibody (1) and its accumulation to the target site over a several days (2). This is followed by an administration of radioligand (3) which binds to the macromolecule and the excess radioligand gets excretes from non-target tissue within hours (4).

There are four pretargeting methodologies that have been investigated in preclinical and/or clinical setting. All reported platforms consist of the same four steps (**Figure 4**), but differ in the type of specific interaction which occurs between the macromolecule and the radioligand. (**Figures 5-8**) In principle, the concept of pretargeting could be applied to the use of any macromolecule in nuclear medicine. In practice however, most of the preclinical and all of the clinical studies have been produced using fragmented or full-

length antibodies. Due to the vast amount research on pretargeting platforms with antibodies, the next chapter's focus covering pretargeting from that perspective.

2.2.2 Methodologies

<u>Bispecific antibody-hapten platform</u>

The concept of pretargeting was first introduced in 1985. Reardan *et al*. proposed an antibody nuclear imaging approach which relied on an *in vivo* radiolabeling of a bispecific antibody (bsAb) *via* radiolabeled hapten.[36] The strategy first reported on over 30 years ago is one of the two pretargeting platforms that have been translated to clinical studies and to this day, the approach is still investigated in clinical studies.[27]

In this pretargeting system, the bsAb consists of at least one target-specific binding region and radiolabeled hapten binding region. (**Figure 5**) At this point, three main types of bsAbs with varying structures have been designed for pretargeting use. The first one includes the use of an engineered fragmented antibody where a biological target binding Fab' is conjugated to a hapten binding Fab'.[37] (**Figure 5A**) The second one includes the use of an IgG full-length antibody which is fused with a hapten specific scFv to the C-terminus of the light chain of the IgG molecule.[38] (**Figure 5C**) Finally, the third bsAb pretargeting agent consists of two target binding Fab' regions which are fused with a third, hapten specific Fab' moiety through disulfide bonds (Tri-Fab').[39,40] (**Figure 5B**)

In addition to three different types of bsAb constructs, there are two kinds of hapten structures which have been proposed; a radiometal chelate complex and a histamine-succinyl-glycine (HSG) peptide based hapten. For the former hapten type, the Fab' region is engineered to bind a radiolabeled chelator such as [^{177}Lu]Lu-DOTA-Bn or [^{111}In]In-

DOTA-Bn.[38,41,42] One of the major disadvantages of the radiometal chelator complex hapten approach is that switching the radiometal or the chelator changes the molecular configuration which requires often the development of a new hapten specific Fab' region for each chelator-metal combination. In turn this makes the approach less modular and feasible to be applied directly with variety of different diagnostic and therapeutic radionuclides. To address the disadvantage of radiometal chelator complex haptens, an alternative hapten molecule type has been explored, the HSG peptide hapten. The HSG region binds with the Fab' or scFv and the HSG is radiolabeled *via* a linker so it does not hamper its binding.
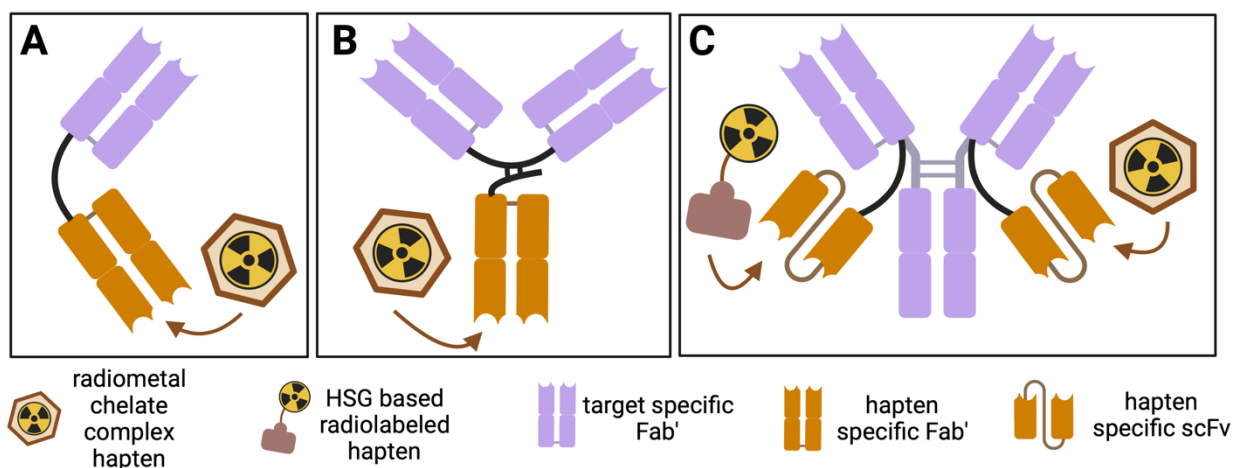
Figure 5. The structure of the bispecific antibody (bsAb) constructs and the hapten molecules for pretargeted nuclear medicine.

The work with the HSG based radiohapten along with the use of a Tri-Fab' bsAb has resulted in the best clinical outcomes of the bsAb-hapten platform for the past 15 years.[39,40,43-45] To date, the evaluation of the Tri-Fab-HSG-hapten approach in humans has included the use of only one antibody construct, a carcinoembryonic antigen (CEA) targeting humanized Tri-Fab bsAb called TF2.[44,45] Some of the most promising and

exciting clinical pretargeting work so far has been produced using the TF2 along with a gallium-68 labeled HSG hapten called ^{68}Ga-IMP288: In metastatic colorectal cancer patients, pretargeted ^{68}Ga-IMP288 resulted in higher sensitivity and specificity in detecting tumor lesions compared to [^{18}F]FDG.[40] The CEA targeted pretargeting pair was also shown to be highly capable of detecting lesions in patients with HER2-negative metastatic breast cancer.[46] In that setting, the pretargeted immuno-PET showed higher overall sensitivity (94.7%) relative to FDG-PET (89.6%). These results underline that antibody based pretargeting is possible with the pretargeting approach and highlight that an antibody based nuclear imaging can provide important information on the molecular structure of a tissue with high sensitivity.

Despite the decades of work on the bsAb-hapten pretargeting methodology and the ongoing promising clinical work with the different IMP288 analogs for diagnostic and therapeutic use, the platform inherently possesses one major challenge, the lack of modularity. The development of the HSG-haptens has been an improvement in this regard, but each bsAb agent targeting a different antigen of interest needs to be designed and engineered even if a clinical mAb already exists. The development of novel working bsAb agents is a time-consuming and costly process. Additionally, the bsAb constructs have faced a lot of challenges in their clinical translation and currently only two bispecific antibodies are approved for the clinical use.[47] Due to the increasing need for antibody based imaging and therapeutic nuclear agents, ideally the pretargeting agents need to be developed and manufactured efficiently and affordably in order to access a wide variety of different tumor antigens.

<u>Streptavidin/avidin-biotin platform</u>

Two years after the introduction of the bsAb based pretargeting concept, in 1987 Hnatowich *et al*. reported the use of another pretargeting approach which relied on the high affinity avidin-biotin association.[48] Later on streptavidin-biotin driven pretargeting has been explored also, even in clinical setting. The streptavidin/avidin-biotin pretargeting approach utilizes the well-established high affinity non-covalent interaction between a streptavidin/avidin protein and a biologically active biotin small molecule as the pretargeting interaction. Streptavidin originates from bacterium Streptomyces and avidin is produced in nature in birds, reptiles and amphibians. Both proteins' interaction is tetrameric and can bind in total of four biotin molecules, where the formed interaction is considered to be one of the strongest non-covalent interactions recorded in nature. (K ~ 10^{14} M^{-1}).

One of the most successful approaches for streptavidin-biotin pretargeting has been to conjugate a full length mAb with a streptavidin/avidin protein and use a radiolabeled biotin as the radioligand agents of the pretargeting approach. (**Figure 6B**) By switching the location of streptavidin/avidin and biotin, the purpose of pretargeting is defeated due to the slower pharmacokinetics of streptavidin (~ 66 000 Da) compared to biotin (224 ~Da). (**Figure 6A**) One of the challenges of having the streptavidin modified mAb is the binding of the endogenous biotin to the streptavidin in the blood pool. To minimize the saturation of the streptavidin binding sites, three-step pretargeting approaches involving the use of different types of CAs have been explored heavily to shorten the lag times needed to use. Indeed, almost all the clinical trials that have been performed using a three-step method have included the use of a streptavidin and/or avidin or a biotin-galactose based CA.[49-51]

Interestingly, despite the use of the three-step approach and the evidence of its effect in reducing the antibody concentration in the blood pool, hematological toxicity has appeared as a reoccurring difficulty in many clinical streptavidin-biotin based radioimmunotherapy studies.[32,52,53]
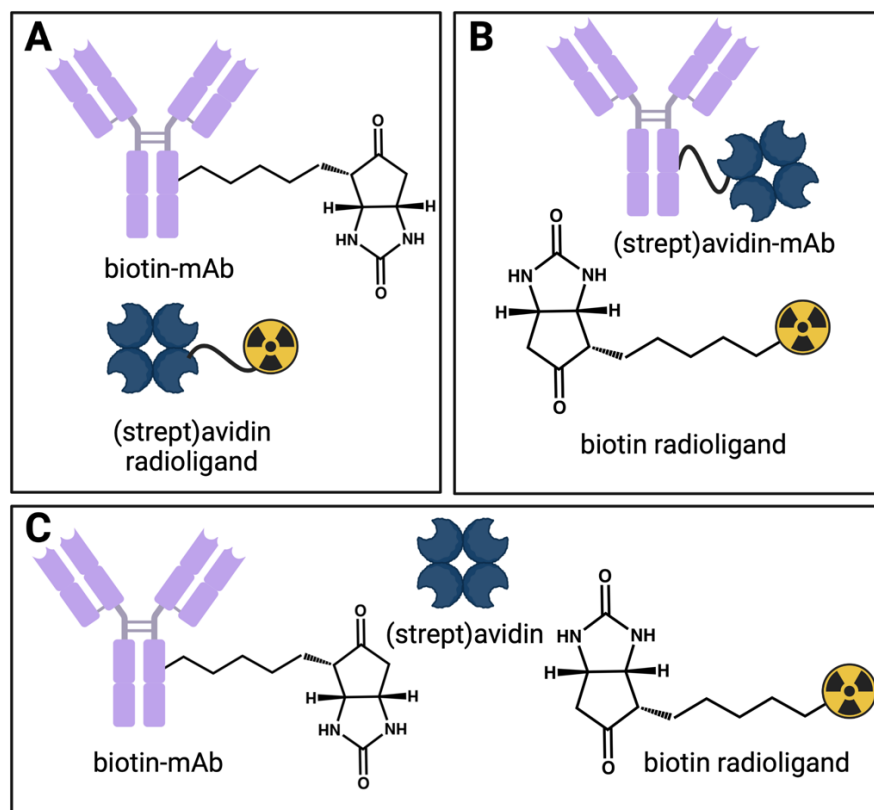
Figure 6. The streptavidin/avidin – biotin pretargeting agents.

The one major obstacle which has been discovered in the platform's clinical studies over and over again, is the immunogenicity of the streptavidin/avidin antibody agents which was observed in all the clinical trials which monitored the immunogenicity of the agents.[49-51, 54-58] Despite the over two decades worth of clinical studies, the immunogenicity concern has not been addressed while concurrently the clinical exploration of the platform has ceased in the past 20 years, with the last reported study occurring in 2005.[59]

Oligonucleotide hybridization platform

In the early 1990s, a third pretargeting approach was introduced to the pretargeting platform family by Kuijpers *et al.* in which the pretargeting interactions relies on oligonucleotide hybridization between the pretargeting agents.[60] Due to the vulnerable *in vivo* stability of deoxyribonucleic acid (DNA) and ribonucleic acid (RNA), the pretargeting agents used for the oligonucleotide hybridization approach are more stable synthetic derivatives of naturally occurring oligomers: Morpholino oligomer (MORF) consists of nucleobases linked by nonionic phosphorodiamidates. (**Figure 7A**) The other synthetic oligonucleotide explored for pretargeting is peptide nucleic acid (PNA), where a pseudopeptide backbone made up of repetitive N-(2-aminoethyl)-glycine units are linking the nucleobases to each other. (**Figure 7B**) Both MORFs and PNAs are resistant to nuclease and are highly water soluble making them appropriate for *in vivo* use. The MORF and PNA predicated pretargeting approach has only been studied in preclinical setting with modest outcomes. The best results, high tumor uptake values along with good tumor to background ratios, are associated with the use of PNA modified affibodies as the targeting agent.[61-63] Due to the low molecular weight and faster pharmacokinetics of antibody fragments such as affibodies (6.5 kDa), performing a two-step pretargeting with them could be argued as unrewarding as a direct labeling with short-lived radionuclides should provide low radiological toxicity in a straightforward manner. Additionally, because of high renal re-absorption of affibodies, pretargeting studies using affibody agents systematically results in high kidney dose, which is not ideal for pretargeted RIT due the radiosensitivity of kidneys. The preclinical studies using PNA or MORF modified full length antibodies have resulted in modest to low target uptake.[64-66]
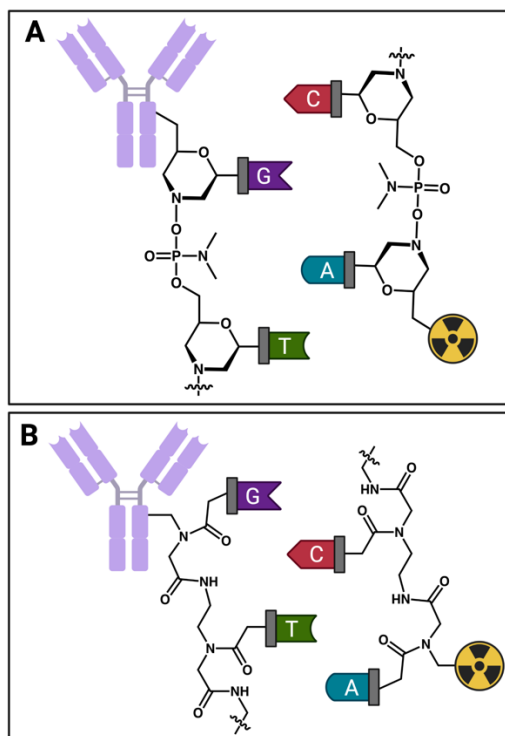
Figure 7. Oligonucleotide pretargeting agents. The morpholino oligomer (MORF) modified antibody and radioligand (**A**) and peptide nucleic acid (PNA) modified antibody and radioligand (**B**).

Click-chemistry platform

The newest methodology investigated for pretargeted nuclear medicine employs click chemistry as the specific interaction between the pretargeting agents. The strategy was first reported by Rossin *et al.* in 2010.[67] Click chemistry pretargeting is the only reported pretargeting strategy that relies on a covalent interaction between the modified antibody and the radioligand. The great majority of click-chemistry driven pretargeting exploits the highly selective and modular inverse electron demand Diels Alder (IEDDA) cycloaddition reaction as the pretargeting interaction.[68] Most explored IEDDA pretargeting interaction occurs between a *trans*-cyclooctene (TCO) dienophile modified antibody and a tetrazene

diene (Tz) radioligand. (**Figure 8**) As with other click reactions, the reaction between the TCO and Tz is highly specific and high yielding, which makes it an intriguing methodology for pretargeting. Additionally, what sets IEDDA reaction apart from other click reactions is its second order rate constant of 10000-100000 $M^{-1}s^{-1}$, which is several magnitudes higher compared to other click reaction often employed in radiochemistry.[25,68,69] The two other investigated click reactions, the Staudinger-Bertozzi ligation's and strain-promoted alkyne-azide cycloaddition's reported rate constants reach only 0.001-0.008 $M^{-1}s^{-1}$ and 0.0024-0.96 $M^{-1}s^{-1}$ respectively. In preclinical pretargeting studies, the low reaction rate of Staudinger ligation has proved an unfeasible approach for *in vivo* pretargeting with no observed specific target uptake.[70]

trans-cyclooectene modified mAb

tetrazene radioligand
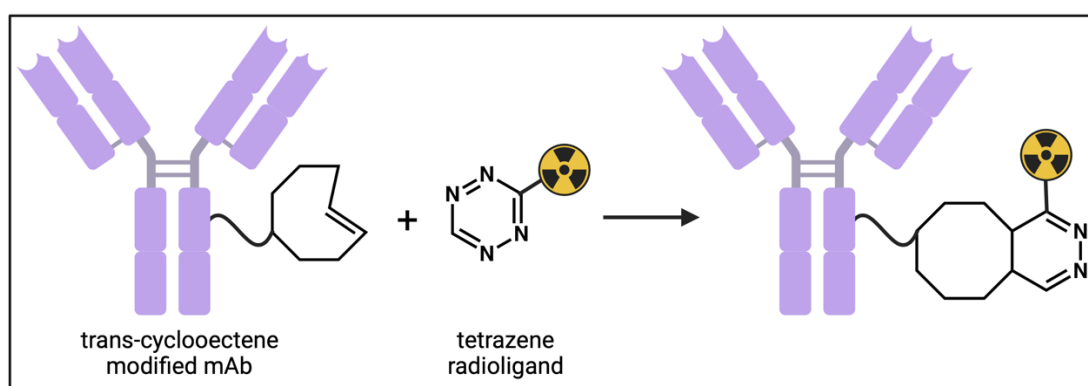
Figure 8. The inverse-electron demand Diels-Alder (IEDDA) click reaction interaction between the pretargeting agents.

While the clinical studies of the IEDDA based pretargeting studies are still pending, the platform has been studied widely for diagnostic,[25,71-73] for therapeutic[29,74-76] and theranostic[77,78] pretargeting applications in preclinical setting with excellent results of high target uptake and target-to-background ratios. One of the advantages and disadvantages of the approach is the high efficiency of the IEDDA reaction, which often leads to the Tz-

radioligand already "clicks" with remaining unbound TCO-mAb still circulating in the blood pool.[29,74] This usually results in higher overall target uptake over time but does increase the observed whole-body radiation doses. However based on the dosimetry studies of the pretargeting methodology, IEDDA pretargeting still demonstrated lower radiation doses to the whole body and importantly to the red marrow compared to the conventional directly radiolabeled antibody.[29,76]

The disadvantage and concern of the IEDDA pretargeting platform lies in the poor *in vivo* stability of the pretargeting components. *In vivo*, the TCO moiety undergoes isomerization to an unreactive form of the compound, cis-cyclooctene, with a reported half-life varying from 1-10 days.[79-81] Once the isomerization happens, the IEDDA reaction will not occur and the modified antibody does not get radiolabeled. So far in the preclinical studies, the *in vivo* stability of the TCO moiety has not been an issue and it has not hampered the interest there exists for the platform. The IEDDA pretargeting has demonstrated best results with lag times from 1 to 3 days. With longer lag time of 5 days, the tumor uptake does decrease significantly.[28,72] It should be noted that due to the slower pharmacokinetics and metabolism of a human compared to a mouse, longer lag times may be required for human use. It remains to be seen how well the IEDDA based pretargeting excels in clinical use despite the *in vivo* stability of the TCO.

2.2.3 Principles

Decades of preclinical and clinical pretargeting studies have provided the research field many opportunities to refine and highlight what an ideal pretargeting platform consists of.

As it was discussed in the section 2.2.2, all of the four pretargeting methodologies have their weaknesses or challenges which still need addressing.

Specificity and kinetics

Firstly, successful pretargeting relies on a specific interaction. No exogenous molecule should interfere with the pretargeting interactions. Additionally the pretargeting interaction should occur relatively quickly, due the limited target accumulation time of the radioligand.

Safety

Secondly, as with all clinically used agents, the toxicity of the pretargeting agents should be as low as possible. Luckily, due to the high sensitivity of PET imaging, nuclear imaging agents are injected in nanomolar to picomolar amount and toxicity is not often a hindering factor of these types of agents. In addition to toxicity, the pretargeting agents should not cause an immunogenic response. The use of agents with even low immunogenic nature limits significantly the number of administrations that can be performed.

Stability

Thirdly, both pretargeting agents should be highly stable *in vivo*. This is especially true for the modified antibody, which is administered into the body days before the subject is introduced to the radioligand. A poor stability of a pretargeting agent potentially results in lower target uptake but also limits the length of the lag time between the administration of the pretargeting agents. In turn, the length of the lag time determines the potential benefits gained from the pretargeting strategy in terms of the received radiation dose.

Investigation of the bsAb-hapten pretargeting strategy in a clinical study showed that lag time of 7 days resulted in better image quality and lower toxicity compared to a lag time of 5 days.[31] In another clinical bsAb-hapten pretargeting trial, it was shown that a lag time of 1 day resulted in significantly higher red marrow doses compared to a lag time of 5 days.[45] Both of these clinical trials highlight the importance of using longer lag times (>3 days).

Modularity and simplicity

Finally, the pretargeting platform should be as modular and convenient to use as possible. Modularity refers to how effortlessly and cost effectively both pretargeting agents can be adapted to a variety of different targets and used with different radionuclides for diagnostic and therapeutic purposes. Because the pretargeting approaches inherently consist already the use of two agents that are administered days apart, the addition of a third agent, such a CA to the pretargeting scheme could potentially hinder the clinical use and enthusiasm of the application. Additionally, the third agent would be an additional agent needing a separate clinical approval and dosing optimization, making the strategy less appealing for wide clinical use.

2.3 CUCURBITURIL AND GUEST MOLECULES AND THEIR INTERACTION

Host-guest chemistry is a form of supramolecular chemistry where at least one guest molecule binds to a cavity of a host molecule *via* multiple non-covalent bonds. Enabled by the different intermolecular forces between the host and the guest, the molecules are thought to have molecular recognition.[82] Host-guest chemistry is often considered as a

synthetic analog to natural receptor-ligand molecular recognition such as the streptavidin-biotin interaction. Host-guest pairs are categorized by their host molecules. The most studied host molecules in biomedicine, molecular engineering and nanotechnology applications include cucurbiturils, cyclodextrins, calixarenes and pillarenes.

2.3.1 Chemical and physical structure of the cucurbiturils

Cucurbit[n]urils (CB[n]) are cyclic host compounds that are composed of varying number of glycoluril monomers that are bonded by methylene bridges. (**Figure 9A**) The number of glycoluril units can vary and in total eight different homologues have been synthesized and characterized (CB[n], n= 5-8, 10, 13-15), CB[6] being the first one to be isolated and crystallized successfully in 1981.[82,83] The different CB[n] homologues are synthesized by reacting glycoluril with formaldehyde under acidic conditions in high temperatures (>100 °C). The glycolurils first form linear oligomeric molecules, which cyclize to form the cyclic CB[n]. By adjusting the temperature and reactions times, the fraction of synthesized CB[n] homologues changes.

Due to the difference in number of monomers within the different homologues the structural features vary between CB[n]s. (**Table 2**) The volume and dimensions of the CB[n] cavity define the types of guest molecules the homologue interacts with. For example, the CB[5] which is the smallest known homologue of the cucurbituril family mostly binds small guest ligands (e.g. alkali and alkaline earth ions) at its carbonyl portals relying only on the dipole-dipole and ion-dipole interactions.[84] As the diameter of the cavity increases the host molecule promotes the guest binding of larger and larger molecules at its inner cavity. For example CB[8] with a large cavity volume can even bind

another macrocyclic molecule, cyclen(1,4,7,10-tetra/-aza/-cyclo/-do/-decane), forming

complexes of macrocycles within macrocycles.[85]
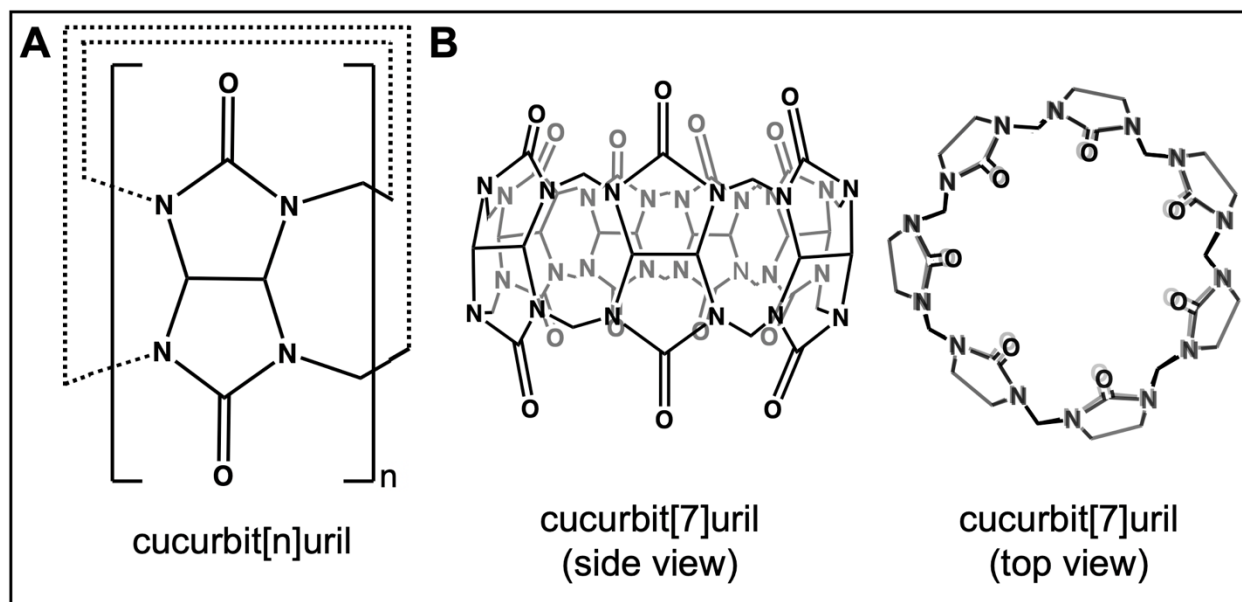
Figure 9. The chemical structure of the cucurbit[n]uril host molecule. Cucurbit[n]uril (**A**)

and cucurbit[7]uril (**B**).

Table 2. Structural and physical parameters of cucurbituril homologues.[86,87] CB[n];

cucurbit[n]uril

	CB[5]	CB[6]	CB[7]	CB[8]	CB[10]
portal diameter (Å)	2.4	3.9	5.4	6.9	9.5-10.6
cavity diameter (Å)	4.4	5.8	7.3	8.8	11.3-12.4
cavity volume (Å^3)	82	164	279	479	870
height (Å)	9.1	9.1	9.1	9.1	9.1
molecular weight (g/mol)	830	996	1163	1329	1661
solubility in water (mM)	20-30	0.02-0.03	30	0.01	<0.05

2.3.2 Thermodynamics of complex formation

CB[n]s form host-guest complexes with highest association constants known for synthetic non-covalent interaction pairs.[88] The favorable conditions for the guest binding can be explained based on the thermodynamics of the complex formation. In aqueous solution, free CB[n]s carry varying number of water molecules in their cavity (5-22 molecules) (**Figure 10**). The water molecules are considered to be 'high energy' due to the geometrical constraints caused by the cavity's limited space and the water molecules' disadvantaged positions for forming a full complement of hydrogen bonds. Additionally the cavity of the CB[n] has low polarizability which does not promote formation of van der Waals interactions between the water molecules and the CB[n] cavity.

From the thermodynamic standpoint upon the guest ligand binding the highly restrained water molecules are released which increases the entropy of the water molecules ($\Delta S^{\circ}_{solvation}$) which is in most cases cancelled by the loss in the entropy of the guest upon complex formation (ΔS°_{guest}). As a result, often the overall change in entropy upon guest binding is negative ($\Delta S^{\circ} < 0$). However the enthalpy changes (ΔH) associated with CB[n] guest complexation are negative which compensates the usual loss in entropy and makes the guest molecule binding thermodynamically favorable.[88,89]
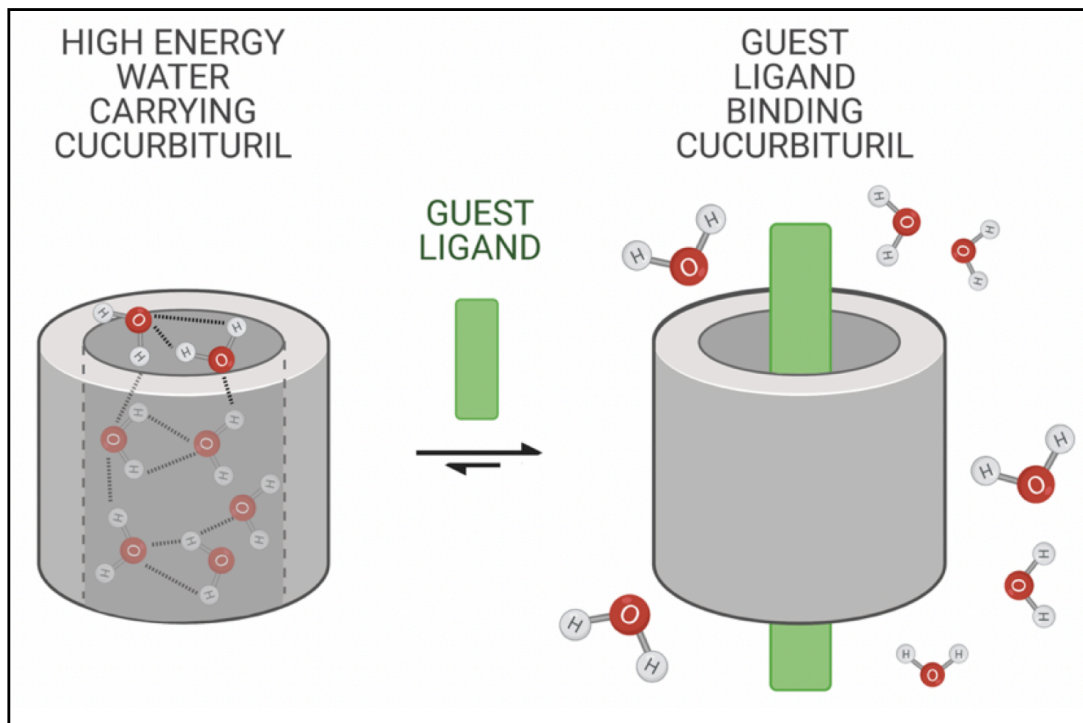
Figure 10. Binding of the guest molecule to the cavity of the cucurbit[n]uril host molecule.

To efficiently release all the water molecules from the cavity and the portal regions of the CB[n], the shape of the guest molecule needs to be complementary to the size and shape of the CB[n].[89] As more water molecules escape the cavity the overall entropy of the bulk water increases which makes the host-guest complex formation more favorable. It has been noted that with guest molecules with extremely high affinity to the cavity of the CB[7] homologue ($K_a > 10^{17}$ M^{-1}), slight changes in the guest molecule structure can result in additional entropy gains resulted from further desolvation of the carbonyl portals, increasing the binding of the guest molecule by several magnitudes.[90]

The guest binding of CB[n] is promoted by the hydrophobic effect and electrostatic forces. Inside of the CB[n] cavity can be considered to have low polarizability which promotes the

binding of guest ligands with a hydrophobic core. Additionally, the CB[n] has carbonyl ring portals on both sides of the ring. These functional groups, carrying a partial negative charge have shown to increase the affinity of guest ligands with full or partial positive charge.[82,91]

As mentioned, the release of the high energy water molecules from the CB[n] cavity results in initial high entropy gains. Again, the volume of the CB[n] cavity limits maximum entropy gains possible for each homologue. For example, the CB[7] holds more water molecules than CB[5] or CB[6] while having a cavity size which doesn't allow the water molecules to align to form hydrogen bonds as efficiently as CB[8]. These factors have shown to result in exceptionally high association constants between CB[7] and its guest ligands.

2.3.3 CB[n]-guest complexes in biomedicine

After the synthesis and crystal structure of several CB[n] homologues were determined and the physicochemical nature of these macrocyclic molecules was established around two decades ago, the research focus with the CB[n] molecules shifted to their applications. This work first started with studying the types of guest molecules that can bind to the different CB[n] cavities and building a library of guest molecules. There are now several hundreds of known molecules that possess varying binding to the different CB[n] homologous and at this point CB7-guest complexation has been studied for biomedical, nanotechnology, biotechnology and biochemical applications.[82]

For biomedicine purposes, the binding of several drug groups has been screened against different CB[n] molecules.[92] To date there are several known anti-pathogenic, anti-

neoplastic, hormones, enzyme inhibitors, neurotransmitters and local anesthetics with significant binding to a one or several CB[n] homologues. The encapsulation by the CB[n] molecule can enhance the solubility, delivery and stability of these small molecule drug compounds. [93-95] Due to the nature of the CB[n]-guest chemistry, the disassociation of the drug from the cavity can be controlled with redox chemistry or by using competing guest ligands. In some instances, the binding of the drug molecule to the CB[n] cavity has shown to even change the pKa of the drug, which in turn can be utilized to release the drug from the cavity with a change in pH.[96,97]
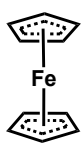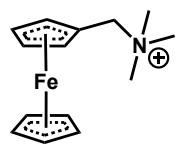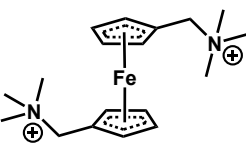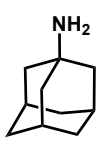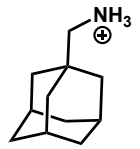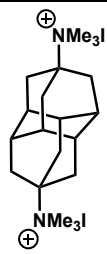
Due to the low solubility of some of the CB[n] homologues (**Table 1**), there has been an effort to form functionalized versions of the CB[n] molecules to adjust their solubility and to make them more compatible for *in vivo* use. Another benefit that has come from synthesizing functionalized CB[n] molecules, is the CB[n] derivatives that can be used for targeted drug delivery. By conjugating the CB[n] cavity to a biologically active molecule, it allows targeted delivery of the drug to the desired disease cell and potentially release the therapeutic drug only once at the target site. One reported example of exploiting targeted CB[n] molecules, involved the use of nanoparticles that were decorated with CB[6] molecules that were bound with either Nile red or spermidine conjugated folate.[98] The Nile red acted as a model of a hydrophobic drug and the folate was used as the targeting tool. Spermidine is another guest molecule of CB[6] which allowed the binding of the folate to the cavity of the CB6 surfaced nanoparticles. The formed constructs demonstrated specific uptake in folate receptor overexpressing HeLa cells. The nanoparticles underwent folate receptor-mediated endocytosis which resulted in the release of the Nile red in the cytosol.

Another recently reported CB[n] drug delivery and release system involved the use of CB[7]-PEG copolymers which were loaded with a known CB[7] guest, an anticancer drug oxaliplatin.[99] The cytotoxicity of the oxaliplatin was decreased when encapsulated by the CB7, but its cytotoxicity was recovered by the presence of the cancer cells that had high concentrations of spermine. Spermine which is also a guest molecule of CB[7], acted as a competitor guest to the oxaliplatin, which resulted in the release of the anticancer drug. In addition to oxaliplatin, other platinum complexes used as anti-cancer drugs such as cisplatin and carboplatin, have known binding affinities to CB7.[100] The encapsulation of these platinum complexes by the host molecule have gained interested due to the potential benefits it could have on the availability, delivery and toxicity of these drugs that play a major part already in clinical treatment of cancer. For all platinum complex drugs *in vivo* degradation by hydrolysis or through sulphur attack from thiols of proteins and peptides is a problem.[101] However, by encapsulating the drugs with a CB[7] molecule, the *in vivo* stability of these drugs is increased. Excitingly, the cytotoxicity of the drugs in most cases is not affected at all or decreased only slightly upon CB[7] binding.[102] In instances where the cytotoxicity is decreased, such as the case with the dropped cytotoxicity of CB[7] encapsulated oxaliplatin vs free oxaliplatin,[103] the observed changes could be related to the affinity of the CB[7]-drug complex or the changes in the internalization of the CB[7]-drug complex vs. free drug.[100] Again, this could be evaded with targeted delivery of the CB[7] molecule and by releasing the drug from the cavity at the target site with changes in the cell environment.

2.3.4 High affinity cucurbit[7]uril-guest pairs

Due to CB[7]'s exceptional capabilities in forming high affinity complexes and having one of the highest water solubilities of any of the CB[n] homologues (30 mM), it has made it highly investigated host molecule for biomedical applications. Since the early 2000s the number of reported high affinity guest ligands for CB[7] host molecule has been increasing. Three molecule types with the highest known affinity towards the CB[7] cavity are ferrocenes, adamantanes and diamantines.[82] Each molecule type reaches extremely high binding constants when there is a positive charge closely adjacent to the ferrocene, adamantane or diamantine guest moiety. (**Table 3**) Each of these guest molecules are hydrophobic which promotes their binding to the hydrophobic core of CB[7] through van der Waals interaction. On the other hand, the positive charge, such as quaternary ammonium, advances the guest molecule's binding via electrostatic ion-dipole interactions with the carbonyl groups located at the CB[7] portals.

Table 3. High affinity guest molecules of cucurbit[7]uril. $K_{a;}$ association constant

guest	1	2	3	4	5	6
chemical structure						
K_a (M^{-1})	$10^{5.6}$	$10^{12.6}$	$10^{15.5}$	$10^{12.6}$	$10^{14.9}$	10^{17}

The association constants, K_a, of different CB[7] guest ligands are determined with nuclear magnetic resonance (NMR), isothermal titration calorimeter (IR) or UV-Vis spectrophotometer.

2.3.5. The promise of the CB[7]-guest chemistry

The discovery of the CB[n] based host-guest chemistry for biomedicine applications is still in its early stages with only limited number of reported *in vivo* studies. But as it has been briefly presented here, the methodology holds a lot of potential and promise. Despite the still expanding group of different CB[n] homologues, the crown jewel of the family is the CB[7] homologue. There are several unique features that the CB[7] possesses that makes it a unique homologue and an intriguing tool for science. Firstly, the CB[7] has the highest solubility out of all the CB[n] molecules. (**Table 2**) Additionally the size of the CB7 cavity is big enough to encapsulate small molecules that are relatively large. For example the guest library of CB[5] is very limited due to its size and it mostly binds small cationic molecules at its carbonyl portals. Additionally the dimensions and volume of the CB[7] molecule creates an extremely unfavorable environment for water molecules when a guest ligand is not bound at its cavity. Partly due to this feature, there are several guest ligands with extremely high binding affinities to the CB[7] cavity, due to the entropy increases gained by the release of these molecules. The binding affinity of diamantine diammonium to the CB[7] cavity is the highest recorded of any CB[n]-guest pair (K_a= 7.2 $\times$ 10^{17} M^{-1}).[90]

Additionally, CB[7] is a highly biocompatible host molecule, as are many other CB[n] homologues. A recent toxicity study of CB[7] molecule reported that the *in vitro* activity of

CB[7] in CHO-K1 cells demonstrated an IC_{50} value of 0.53 ± 0.02 mM which corresponded to around 620 mg/kg of cell material.[104] Moreover, when the cells were incubated with a nonlethal dose of CB[7], no changes in the cellular integrity were detected. In the molecule's *in vivo* safety studies in mice, the maximum tolerated dose of intravenously administrated CB[7] was 250 mg/kg. To further expand the possibilities of CB7 based drug delivery systems, it has been reported that the CB7 molecules are internalized by certain cell types.[105]

3. SPECIFIC AIMS

Aim 1: Synthesis and characterization of the two pretargeting components; cucurbit[7]uril-conjugated monoclonal antibody and a series of ferrocene and adamantane based radioligands.

Aim 2: *In vivo* evaluation of the radioligands in healthy mice and evaluation of the pretargeting system for positron emission tomography (PET) in tumor bearing mice.

4. MATERIALS AND METHODS

All reagents were purchased from Sigma-Aldrich (Missouri, USA) unless stated otherwise. The reagents were used without any additional purification. p-SCN-Bn-NOTA x 3 HCl and p-SCN-Bn-Deferoxamine were purchased from Macrocyclics (Texas, USA). t-BOC-N-Amido-PEG3-Amine, t-Boc-N-amido-PEG7-amine and DBCO-C6-NHS ester were acquired from BroadPharm (California, USA). The cucurbit[7]uril-azide (CB7-N_3) was synthesized by the Chemical Synthesis Core of Vanderbilt University (Tennessee USA). The M5A (hT84.66-M5A) antibody was received from Dr. Paul Yazaki at City of Hope (California, USA). [^{68}Ga]GaCl$_3$ was purchased from the Vanderbilt University Institute of Imaging Science Research Radiochemistry Core Laboratory and [^{67}Ga]GaC$_6$H$_5$O$_7$ was acquired from Jubilant Radiopharma, (Pennsylvania, USA). The [^{89}Zr]Zr(C$_2$O$_4$)$_2$ and [^{64}Cu]CuCl$_2$ were purchased from Washington University School of Medicine MIR Cyclotron Facility (Missouri, USA). Cell culturing media solutions were purchased from either the Vanderbilt University Medical Center (VUMC) Molecular Cell Biology Resource Core or VWR International unless mentioned otherwise. The reagents for the SDS PAGE and Western Blotting were purchased from ThermoFisher Scientific. Phosphate buffered saline, pH=7.4 (PBS7.4) solution was prepared from phosphate-buffered saline powder pH 7.4. The water (H$_2$O) used for all the experiments was Milli-Q Water purified with a Millipore Milli-Q lab water system set up with Millipak Express 40 filters. Chelexed water was prepared from Milli-Q Water using Chelex 100 Chelating Resin (Bio-Rad).

All the cell lines were acquired from the American Tissue Culture Collection (ATCC, Virginia, USA). BxPC3 human pancreatic adenocarcinoma cells were maintained in

RPMI-1640 medium with 0.3 g/l glutamine, 25 mM HEPES, 1% (vol/vol) Penicillin-Streptomycin and 10% (vol/vol) fetal bovine serum. MIAPaCa-2 human pancreatic carcinoma cells were grown in DMEM/High glucose medium containing 4mM L-glutamine, 4.5 g/L glucose, and sodium pyruvate, 1% (vol/vol) Penicillin-Streptomycin,10% (vol/vol) fetal bovine serum and 2.5% (vol/vol) Horse Serum (donor herd) (Sigma-Aldrich). Both cells were kept in a 37 °C environment containing 5% CO_2 and extracted using 0.25% Trypsin-EDTA.

The female athymic nude mice (Crl:NU(NCr)-Foxn1nu and male athymic nude mice NU/J were purchased from The Jackson Laboratory (Maine, USA). All experiments involving laboratory animals were performed in accordance with either the Vanderbilt University Medical Center Institutional Animal Care and Use Committee or Institutional Animal Care and Use Committee at Stony Brook Medicine.

The instruments and chromatography methods used in the synthesis and characterization of all the compounds are detailed in the Appendix I.

Statistical analysis for all the biodistribution and *in vitro* experiment data was performed with 2-tailed unpaired t tests using GraphPad Prism (GraphPad Software, Inc.). A p-value between two groups of $p < 0.05$ was considered significant.

4.1 DEVELOPMENT OF GUEST RADIOLIGANDS

4.1.1 Synthesis of ferrocene radiolabeling precursors

Two ferrocene radiolabeling precursors, NOTA-PEG$_3$-Fc (**5**) and NOTA-PEG$_7$-Fc (**6**) were synthesized in three reactions. (**Figure 11**) **5** and **6** and their reaction intermediates, NBOC-PEG$_3$-NH-Fc (**1**), NBOC-PEG$_7$-NH-Fc (**2**), NBOC-PEG$_3$-Fc (**3**) and NBOC-PEG$_7$-

Fc (**4**) were characterized with proton nuclear magnetic resonance (^{1}H-NMR) and high-resolution mass spectrometry (HRMS). The chemical purity of the compounds was analyzed with a reverse phase high performance liquid chromatography (RP-HPLC) instrument using an analytical C18 column detecting wavelength of 254 nm.

<u>NBOC-PEG$_3$-NH-Fc (**1**) and NBOC-PEG$_7$-NH-Fc (**2**)</u>

Ferrocenecarboxaldehyde (110-130 mg; 0.52-0.62 mmol; 1.0 eq.), triethylamine (7.3 mg; 0.072 mmol) and t-boc-N-amido-PEG3-amine (42 mg; 0.14 mmol; 0.28 eq.) or t-boc-N-amido-PEG7-amine (73 mg; 0.16 mmol; 0.26 eq.) were dissolved in methanol (MeOH,15-40 mL) The reaction was stirred for 2 h at room temperature (RT) followed by addition of sodium triacetoxyborohydride (1.1-1.2 g; 5.3-5.7 mmol). The reaction was stirred overnight. The solution was evaporated to dryness. Dichloromethane (DCM, 20 mL) and H$_2$O (10 mL) were added to the vial. DCM phase was collected and H$_2$O phase washed with DCM 2-3 times. The organic phases were combined and dried with Na$_2$SO$_4$, and DCM was evaporated off. The crude product was redissolved DMSO:ACN:H$_2$O (1:1:1) solution. The undissolved material was filtered out and the supernatant was collected for purification. **1** and **2** were purified with RP-HPLC using a preparative C18 column. **1**: Chemical purity: 99.5 % **2**: Chemical purity 95.0 %

Characterization of **1**: ^{1}H-NMR (500 MHz, methanol-d$_4$) δ; 4.314 (s, 2 H), 4.212 (s, 2 H), 4.141 (s, 5 H), 3.922 (s, 2 H), 3.649-3.479 (m, 10 H), 3.413 (t, 2 H), 3.134 (t, 2 H), 3.020 (s, 2 H), 1.364 (s, 9 H) HRMS (ESI)(+) m/z calculated for C$_{24}$H$_{38}$FeN$_2$O$_5$ [M+H]$^+$: 491.2208, measured: 491.2204.

Characterization of **2**: ^{1}H-NMR (400 MHz, methanol-d$_4$); 4.449 (s, 2 H), 4.341 (s, 2 H), 4.256 (s, 5 H), 4.117 (s, 2 H), 3.751 (t, 2 H), 3.685-3.675 (m, 4 H), 3.669-3.654 (m, 10 H), 3.657-3.604 (m, 10 H), 3.527 (t, 2 H), 3.24 (t, 2 H), 3.197 (t, 2 H), 1.460 (s, 9 H). HRMS (ESI)(+) m/z calculated for $C_{32}H_{55}FeN_2O_9$ [M+H]$^+$: 667.3257 and measured: 667.3252.
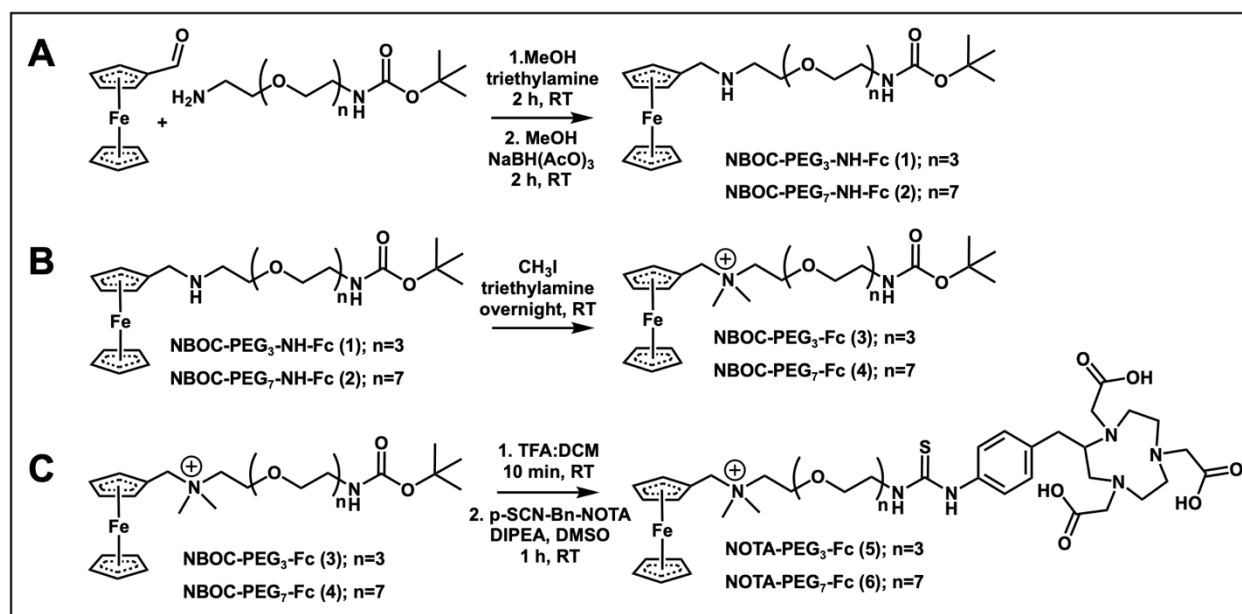
Figure 11. The reaction schemes for ferrocene radiolabeling precursors (**5,6**) in three steps (**A-C**).

NBOC-PEG$_3$-Fc (**3**) and NBOC-PEG$_7$-Fc (**4**)

1 (41 mg; 0.083 mmol) or **2** (32 mg; 0.048 mmol) was dissolved in iodomethane (30-60 mL) and triethylamine (7.3 mg, 0.072 mmol; 0.87-1.5 eq.). The solution was stirred overnight at RT. The solvent was evaporated off. **3** and **4** were purified with RP-HPLC using a semipreparative C18 column. **3**: Chemical purity: 96.9% **4**: Chemical purity 95.6 %.

Characterization of **3**: ^{1}H-NMR (500 MHz, methanol-d$_4$) δ; 4.456 (m, 2 H), 4.346 (s, 2 H), 4.193 (s, 5 H), 3.855 (s, 2 H), 3.617 (s, 4 H), 3.597-3.527 (m, 4 H), 3.430 (t, 2 H), 3.368

(t, 2 H), 3.144 (t, 2 H), 2.943 (s, 6 H), 2.851 (s, 1 H), 1.364 (s, 9 H), HRMS (ESI)(+)

$C_{26}H_{43}FeN_2O_5^+$ [M]$^+$ calculated: 519.2516, measured: 519.2516.

Characterization of **4**: ^{1}H-NMR (500 MHz, dichloromethane-d2); 4.535 (s, 2 H), 4.490 (s,

2 H), 4.425 (s, 2 H), 4.285 (s, 5 H), 3.978 (s, 2 H), 3.736-3.711 (m, 2 H), 3.697-3.681 (m,

2 H), 3.669-3.622 (m, 20 H), 3.556-3.510 (m, 4 H), 3.306 (s, 2 H), 3.084 (s, 6 H), 1.460

(s, 9 H). HRMS (ESI)(+) m/z calculated for $C_{34}H_{59}FeN_2O_9^+$ [M]$^+$: 695.3570, measured:

695.3564.

NOTA-PEG$_3$-Fc (**5**) and NOTA-PEG$_7$-Fc (**6**)

3 (28 mg, 0.054 mmol) or **4** (41 mg; 0.059 mmol) was dissolved in DCM (1-2 mL) and

trifluoroacetic acid (1-2 mL). The reaction was stirred for 10-15 min at RT. The reaction

was evaporated to dryness. The deprotected **3** or **4** was dissolved in DMSO (1mL) along

with p-SCN-Bn-NOTA (25 mg, 0.044 mmol; 0.74 eq. or 22 mg; 0.039 mmol; 0.66 eq.

respectively) and triethylamine (25 mg, 0.25 mmol; 4.2-4.6 eq.). The reaction was stirred

at RT for 60-90 min. **5** and **6** were purified with RP-HPLC with a semipreparative C18

column. **5**: Overall reaction yield: 20.3%. Chemical purity: 95.6 % **6**: Overall reaction yield

7.4 %. Chemical purity 98.2 %.

Characterization of **5**: ^{1}H-NMR (400 MHz, methanol-d$_4$) δ 7.30 (d, 4 H), 4.53 (s, 4 H), 4.51

(s, 2 H), 4.42 (s, 5 H), 3.89 (s, 2 H), 3.77 (s, 2H), 3.67 (s, 12 H), 3.60-3.33 (m, 7 H), 3.28-

3.06 (m, 8 H), 2.99 (s, 6 H), 2.94-2.49 (m, 4 H); HRMS (ESI)(+) $C_{41}H_{61}FeN_6O_9S^+$ [M]$^+$

calculated for: 869.3570, measured: 869.3559.

Characterization of **6**: ^{1}H-NMR (500 MHz, methanol-d4); 7.322 (d, 4 H), 4.540 (d, 4 H),

4.443 (s, 2 H), 4.286 (s, 5 H), 3.939 (s, 2 H), 3.790 (s, 2 H), 3.699 (s, 7 H), 3.683-3.607

(m, 24 H), 3.436 (s, 2 H), 3.216 (s, 4 H), 3.186 (s, 2 H), 3.019 (s, 2 H), 3.216 (s, 4 H),

2.678 (s, 8 H). HRMS (ESI)(+) m/z calculated for $C_{49}H_{77}FeN_6O_{13}S^+$ [M]$^+$: 1045.4613,

measured: 1045.4615.

4.1.2 Synthesis of adamantane radiolabeling precursors

Three adamantane radiolabeling precursors, NOTA-Adma (**10**), NOTA-PEG$_3$-Adma (**11**)

and NOTA-PEG$_7$-Adma (**12**) were synthesized in two steps. (**Figure 12**) **10**-**12** and their

reaction intermediates, NBOC-Adma (**7**), NBOC-PEG$_3$-Adma (**8**) and NBOC-PEG$_7$-Adma

(**9**) were characterized with ^{1}H-NMR and HRMS. The chemical purity of the UV active

compounds (**10**-**12**) and non-UV active compounds (**7**-**9**) was analyzed with a RP-HPLC

instrument using an analytical C18 column detecting wavelength of 254 nm or ^{1}H-NMR

respectively.
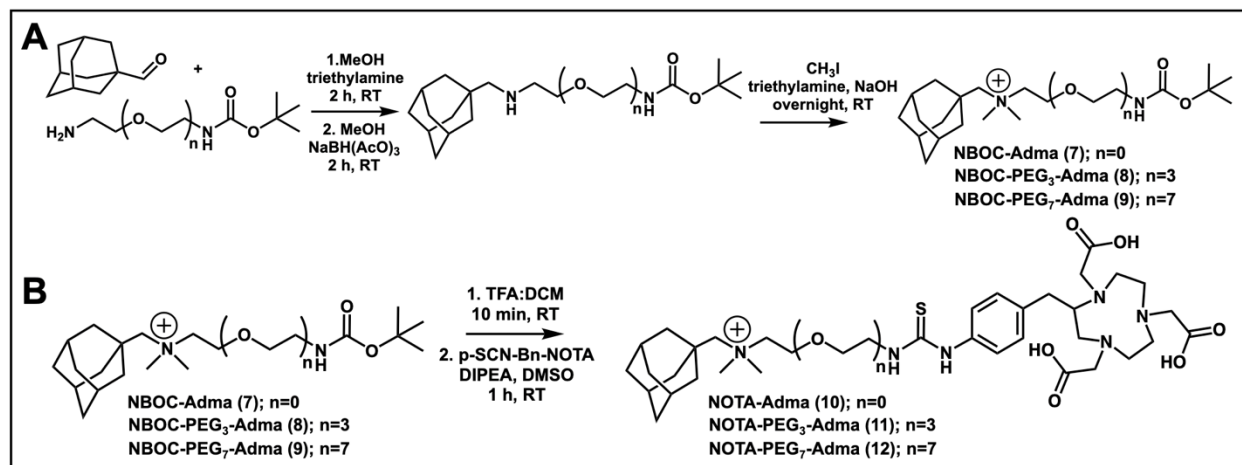
Figure 12. The reaction scheme for adamantane radiolabeling precursors (**10**-**12**).

<u>NBOC-Adma (**7**)</u>

Adamantane-1-carbaldehyde (310 mg; 1.9 mmol; 1.0 eq.), NBOC-ethylenediamine (290

mg; 1.8 mmol; 0.95 eq.) and triethylamine (15 mg; 0.14 mmol; 0.074 eq.) were dissolved

in MeOH (50 mL) and stirred for 30 min at RT before the addition of sodium

triacetoxyborohydride (590 mg; 2.8 mmol; 1.5 eq.). The reaction solution was stirred for 60 min in RT. The solvent was evaporated off. H_2O (50 mL) was added to the crude product material. The water phase was extracted with diethyl ether (3×40 mL) followed by combining and evaporating the organic phases to yield clear oily material. Iodomethane (30 mL) and NaOH (120 mg; 3.0 mmol; 1.6 eq.) were added to the reaction vial. The methylation reaction was stirred for 2 h, which was followed by evaporating the iodomethane and adding fresh iodomethane which was repeated once more. The solvent was evaporated off and replaced with DCM. Undissolved NaOH was filtered out and the DCM evaporated. The crude **7** was dissolved in ACN (7 mL) and purified with a RP-HPLC chromatography system using a C18 semipreparative column. Reaction yield: 60.0 %

Chemical purity: 95.8 %

Characterization of **7**: ^{1}H-NMR (500 MHz, methanol-d4); 3.580-3524 (m, 2 H), 3.518-3.472 (m, 2 H), 3.237 (s, 6 H), 3.182 (s, 2 H), 2.053 (s, 3 H), 1.863 (d, 6 H), 1.781 (q, 6 H), 1.454 (s, 9 H). HRMS (ESI)(+) m/z calculated for $C_{20}H_{37}N_2O_2^+$ [M]$^+$: 337.2850 and measured: 337.2849.

NBOC-PEG$_3$-Adma (**8**)

Adamantane-1-carbaldehyde (210 mg; 1.3 mmol; 1.0 eq.), t-boc-N-Amido-PEG3-Amide (360 mg; 1.2 mmol; 1.1 eq.) and triethylamine (21 mg; 0.21 mmol; 0.16 eq.) were dissolved in MeOH (50 mL). The reaction was stirred for 30 min at RT followed by an addition of sodium triacetoxyborohydride (510 mg; 2.4 mmol; 1.8 eq.). The reaction was stirred overnight at RT. The solvent was evaporated off followed by an addition of diethyl ether (10 mL). The undissolved material was filtered, and the diethyl ether phase was

collected and evaporated. The crude material was dissolved in iodomethane (20 mL) along with triethylamine (21 mg; 0.21 mmol; 0.16 eq.) and NaOH (110 mg; 2.8 mmol; 2 eq.). The methylation reaction was stirred at RT for 2 h. The iodomethane was evaporated and replaced with fresh iodomethane twice (20 mL). Finally iodomethane was evaporated off and replaced with DCM. NaOH was filtered out and the DCM evaporated. The crude **8** was dissolved in ACN (7 mL) and MeOH (3 mL). The dissolved material was injected to RP-HPLC chromatography system for purification with a C18 semipreparative column. Reaction yield 68.0 % Chemical purity: 99.8 %

Characterization of **8**: ^{1}H-NMR (500 MHz, methanol-d4); 3.977-3.928 (m, 2 H), 3.718-3.636 (m, 8 H), 3.629-3.595 (m, 2 H), 3.497 (t, 2 H), 3.274-3.237 (m, 6 H), 3.236-3.181 (m, 4 H), 2.048 (m, 3 H), 1.861 (d, 6 H), 1.776 (q, 6 H), 1.440 (s, 9 H). HRMS (ESI)(+) m/z calculated for $C_{26}H_{49}N_2O_5^+$ [M]+: 469.3636 and measured: 469.3639.

NBOC-PEG$_7$-Adma (**9**)

Adamantane-1-carbaldehyde (190 mg; 1.1 mmol; 1.0 eq.), t-Boc-N-amido-PEG7-amine (220 mg; 0.46 mmol; 0.42 eq.) and triethylamine (22 mg; 0.22 mmol; 0.20 eq.) were dissolved and stirred in MeOH (30 mL) at RT for 1 h. Sodium triacetoxyborohydride (540 mg; 2.6 mmol; 2.6 eq.) was added to the solution and stirring was continued for 2 h. The solvent was evaporated off and redissolved in diethyl ether (10 mL). Undissolved material was filtered off and washed twice with diethyl ether (2 x 10 mL). Diethyl ether phases were combined and concentrated. The crude material was mixed with iodomethane (10 mL) and NaOH (110 mg; 2.8 mmol; 2.8 eq.). The solution was stirred for 2 h which was followed by evaporation of the iodomethane. Fresh iodomethane was added and replaced

twice more and finally evaporated off. **13** was dissolved in ACN (4 mL) and purified with

a RP-HPLC C18 semipreparative column. Reaction yield: 31.3 % Chemical purity: 98.9%

Characterization of **9**: ^{1}H-NMR (500 MHz, methanol-d4); 3.972-3.933 (s, m H), 3.670-

3.672 (m, 2 H), 3.671-3.622 (m, 24 H), 3.621-3.598 (m, 2 H), 3.506 (t, 2 H), 3.246 (s, 6

H), 3.233-3.206 (m, 4 H), 2.046 (s, 3 H), 1.858 (d, 6 H), 1.770 (q, 6 H), 1.438 (s, 9 H).

HRMS (ESI)(+) m/z calculated for $C_{34}H_{65}N_2O_9^+$ [M]$^+$: 645.4685 and measured: 645.4679.

NOTA-Adma (**10**), NOTA-PEG$_3$-Adma (**11**) and NOTA-PEG$_7$-Adma (**12**)

7, 8 or **9** (45 mg; 0.13 mmol; 1.0 eq. / 52 mg; 0.11 mmol; 1.0 eq. / 21 mg; 0.033 mmol;

1.0 eq. respectively) was dissolved in DCM (3 mL) and trifluoro acetic acid (0.6 -2 mL).

The solution was stirred at RT for 15-20 min. The solution was evaporated to dryness.

The deprotected **7, 8** or **9** and p-SCN-Bn-NOTA (39 mg; 0.070 mmol 0.54 eq. / 17 mg;

0.030 mmol 0.27 eq. / 18 mg; 0.032 mmol; 0.97 eq. respectively) were dissolved in DMSO

(1 mL) mixed with N,N-diisopropylethylamine (1.2 eq.). The reaction was stirred for 40

min at RT. The crude product was diluted with ACN (2 mL). The product was purified with

a RP-HPLC C18 semipreparative column. **10**: Reaction yield: 24.2% Chemical purity:

97.6% **11**: Reaction yield 53.2% Chemical purity: 97.2% **12**: Reaction yield: 45.0%

Chemical purity: 95.8%

Characterization of **10**: ^{1}H-NMR (500 MHz, methanol-d4); 7.343 (d, 2 H), 7.292 (d, 2 H),

4.142 (t, 2 H), 3.992-3.704 (m, 4 H), 3.673 (t, 2 H), 3.477-3.322 (m, 4 H), 3.279 (s, 6 H),

3.228 (s, 4 H), 3.192-3.139 (m, 2 H), 3.138-3.003 (m, 2 H), 2.999-2.902 (m, 1 H), 2.900-

2.745 (m, 2 H), 2.744-2.540 (m, 2 H), 2.046 (s, 3 H), 1.868 (d, 6 H), 1.771 (q, 6 H). HRMS

(ESI)(+) m/z calculated for $C_{35}H_{55}N_6O_6S^+$ [M]$^+$: 687.3898 and measured: 687.3899.

Characterization of **11**: ^{1}H-NMR (500 MHz, methanol-d4); 7.378 (d, 2 H), 7.276 (d, 2 H), 4.017-3.916 (m, 4 H), 3.916-3.800 (m, 2 H), 3.699 (s, 2 H), 3.728-3.671 (m, 2 H), 3.670-3.650 (m, 8 H), 3.649-3.612 (m, 2 H), 3.434-3.325 (m, 4 H), 3.236 (s, 6 H), 3.209 (s, 4 H), 3.184-3.133 (m, 2 H), 3.131-2.951 (m, 2 H), 2.948-2.885 (m, 1 H), 2.882-2.740 (m, 2 H), 2.738-2.572 (m, 2 H), 2.033 (s, 3 H), 1.842 (d, 6 H), 1.762 (q, 6 H). HRMS (ESI)(+) m/z calculated for $C_{41}H_{67}N_6O_9S^+$ $[M]^+$: 819.4685 and measured: 819.4681.

Characterization of **12**: ^{1}H-NMR (500 MHz, methanol-d4); 7.377 (d, 2 H), 7.270 (d, 2 H), 4.024-3.911 (m, 4 H), 3.910-3.795 (m, 2 H), 3.770 (s, 2 H), 3.694-3.671 (m, 2 H), 3.664-3.614 (m, 24 H), 3.612-3.544 (m, 2 H), 3.429-3.320 (m, 4 H), 3.237 (s, 6 H), 3.214 (s, 4 H), 3.186-3.143 (m, 2 H), 3.141-2.985 (m, 2 H), 2.974-2.887 (m, 1 H), 2.886-2.737 (m, 2 H), 2.755-2.544 (m, 2 H), 2.041 (s, 3 H), 1.852 (d, 6 H), 1.771 (q, 6 H). HRMS (ESI)(+) m/z calculated for $C_{49}H_{83}N_6O_{13}S^+$ $[M]^+$: 995.5733 and measured: 995.5724.

4.1.3 Synthesis of fluorescein adamantane

1-Adamantanemethylamine (5.4 mg; 0.033 mmol; 1.0 eq.), triethylamine (3.1 mg; 0.031 mmol; 0.94 eq.) and NHS-Fluorescein (16 mg; 0.033 mmol; 1.0 eq. in 1 mL of DMSO) were dissolved in MeOH (500 μL). The reaction was stirred at RT for 1 h. Formed FL-Adma (**13**) was purified with RP-HPLC using a preparative C18 column. Reaction yield: 50.8% Chemical purity: 96.8%

Characterization of **13**: ^{1}H-NMR (500 MHz, methanol-d$_4$) δ 8.34 (s, 1 H), 8.08 (d, 1 H), 7.23 (d, 1 H), 6.61 (d, 2 H), 6.59-6.55 (m, 2 H), 6.47 (d, 1 H), 6.45 (d, 1 H), 3.07 (s, 2 H), 1.92 (s, 3 H), 1.73-1.61 (q, 6 H), 1.55 (m, 6 H) HRMS (ESI)(+) $C_{32}H_{29}NO_6$ $[M+H]^+$ calculated for: 524.2073, measured: 524.2068

4.1.4 Radiosynthesis of [67/68]Ga-labeled radioligands

[67]Ga-labeling of **5**

5 was radiolabeled with gallium-67 to form [^{67}Ga]Ga-NOTA-PEG$_3$-Fc (**14**) radioligand. (**Figure 13**) First, [^{67}Ga]GaC$_6$H$_5$O$_7$ was converted to [^{67}Ga]GaCl$_3$. [^{67}Ga]GaC$_6$H$_5$O$_7$ (59-160 MBq) solution was diluted using chelexed mQ water with 1/3 of its volume. The [^{67}Ga]GaC$_6$H$_5$O$_7$ solution was loaded onto a Sep-Pak Vac Silica cartridge 1cc/100 mg (Waters) which was pretreated with chelexed mQ water (2 mL). The silica cartridge was washed with chelexed mQ water (5 mL). Gallium-67 was eluted in two 0.50-0.60 mL fractions as [^{67}Ga]GaCl$_3$ using chelexed 0.1 M HCl solution.

[^{67}Ga]GaCl$_3$ solution (26-93 MBq; 0.50-1.0 mL) in 0.1 M HCl was adjusted to pH 5 using 1M NH$_4$OAc followed by addition of **5** in DMSO. The reaction was incubated at RT for 10 min. Radiolabeling efficiency was monitored with radio-HPLC using an analytical HPLC C18 column. **14** was purified using a Sep-Pak C18 Plus Light Cartridge (Waters) by diluting the reaction solution with mQ water (4 mL), loading the solution to the cartridge, washing the cartridge with mQ water (7 mL) and eluting the product in five fractions of 0.20 mL of 100% ethanol. The radiochemical purity of the compound was determined with radio-HPLC.

[68]Ga-labeling of **5** and **11**

5 and **11** were labeled with gallium-68 to synthesize [^{68}Ga]Ga-NOTA-PEG$_3$-Fc (**15**) and [^{68}Ga]Ga-NOTA-PEG$_3$-Adma (**21**). (**Figure 13**) [^{68}Ga]GaCl$_3$ was obtained by eluting the radionuclide from a [68]Ge/^{68}Ga generator (ITG) using 0.05 M HCl. [^{68}Ga]GaCl$_3$ eluate (1

mL; 200 - 820 MBq) in 0.05 M HCl was adjusted to pH 5 using 1M NH$_4$OAc followed by addition of **5** or **11** in DMSO (5.0 mg/mL solution). The solution was incubated at RT for 10 min. The labeling was monitored with radio-iTLC using 50 mM EDTA as the mobile phase and iTLC-SG strips (Agilent Technologies) as the solid phase. Due to initial high radiochemical yield, no further purification was needed. Solution of **15** or **21** was pH adjusted to 7 using PBS7.4. The quality control was done on radio-iTLC with the same method as the labeling monitoring.
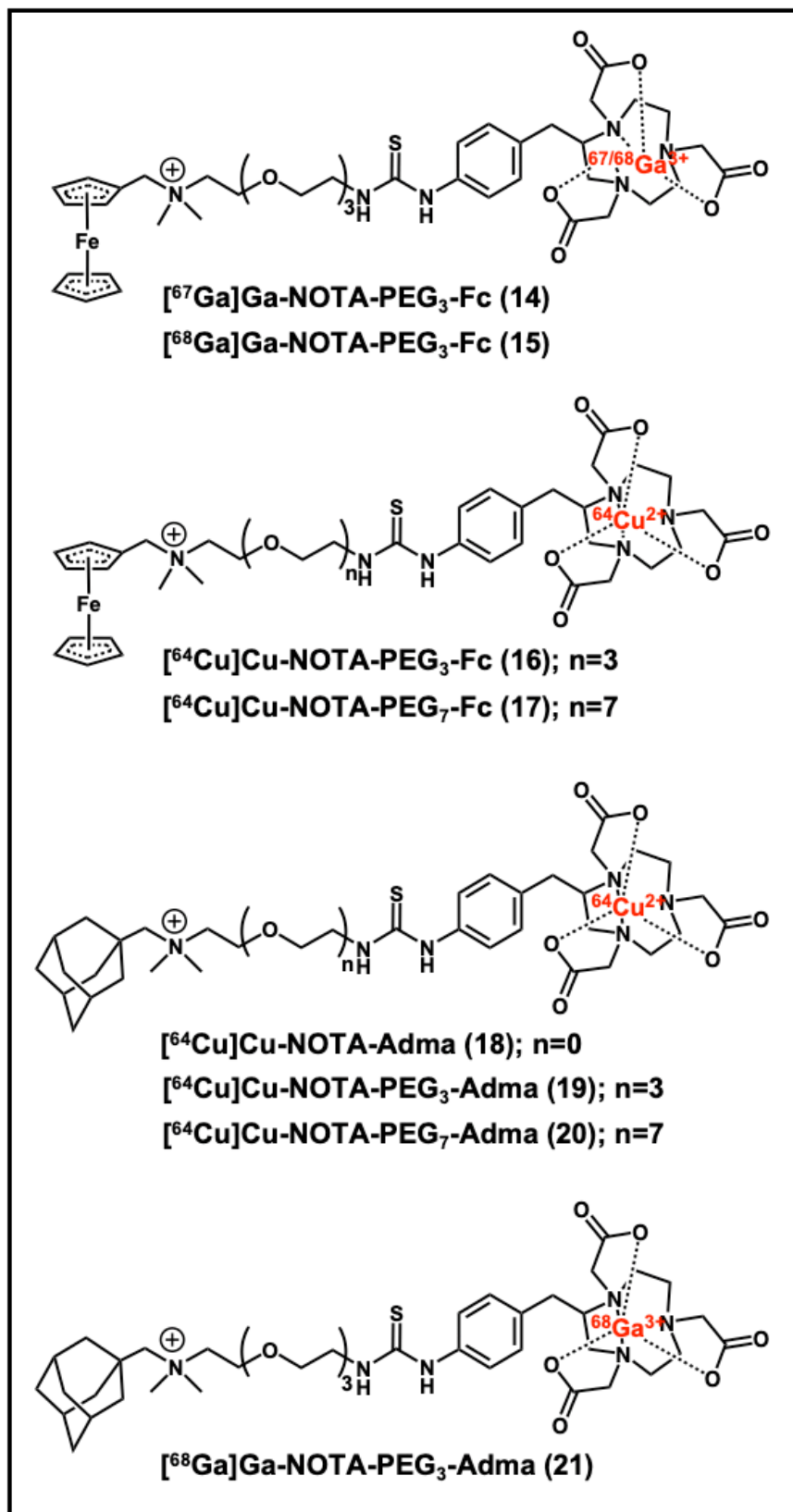
Figure 13. The chemical structure of the guest radioligands (**14-21**).

4.1.5 Radiosynthesis of ^{64}Cu-labeled radioligands

^{64}Cu-labeling of **5**, **6**, **10**-**12**

Copper-64 was produced with a cyclotron *via* ^{64}Ni(p,n)^{64}Cu reaction. The [^{64}Cu]CuCl$_2$ in 0.05 M HCl (4.0-28 μL; 41-290 MBq) was added first to 0.2 M NH$_4$OAc solution (50-200 μL; pH 5.5). Desired amount of **5**, **6** or **10**-**12** was measured (5.0 mg/mL in dimethyl sulfoxide; DMSO) to the prepared solution. The reaction solution was left at RT for 10 min before the labeling efficiency was measured with radio-HPLC. Due to the initial high radiochemical purity (>95 %), no purification was required for the synthesized **16**-**20**. (**Figure 13**)

3.1.6 Distribution coefficient

The distribution coefficient (log D) value for **14**, **16**-**20** was determined with the shake-flask method. Freshly synthesized radioligand (2-30 μL in 0.2 M NH$_4$OAc; 340-730 kBq;) was added to equal volumes of PBS (pH 7.4; 0.70 mL) and 1-octanol (0.70 mL). The mixture was agitated at RT for 10 min (700-900 rpm). Next, the mixture was centrifuged (1000 g), and 0.20 mL collected from each phase to tared tubes. These were reweighed and measured with a gamma counter to determine the relative amount of radioligand in each phase. The log D value was calculated with equation 1. The experiment was done in triplicate.

$$\log D = \log_{10} \frac{\% \text{ radioligand in 1-octanol}}{\% \text{ radioligand in PBS7.4}} \tag{1}$$

4.1.7 *In vitro* stability and plasma protein binding

The *in vitro* stability of **14**, **16**-**20** was analyzed in PBS7.4 and in bovine or human plasma at 37 ºC up to 4 (**14**, **16** and **17)** or 24 h (**18**-**20)**. Firstly, for the PBS7.4 stability studies, freshly synthesized radioligand, **14** or **16**-**20** (24-38 μL in 0.2 M NH$_4$OAc; 0.29-5.2 Mq) was added to an Eppendorf containing 0.12-1.5 mL of PBS (pH 7.4). The solution was incubated at 37 °C and 3-4 samples were taken between 30 min and 24 h after the start time of the incubation. The % of intact radioligand was determined by radio-HPLC. Secondly for the plasma stability studies, freshly synthesized **16**-**17** or **18**-**20** (5-8 μL in 0.2 M NH$_4$OAc; 1.4-2.4 MBq) was added to 150 μL of bovine or human plasma (prepared in PBS7.4) respectively. A sample was incubated at 37 °C and prepared for analysis between 1 to 24 h post incubation start time. For analysis, the sample was placed on ice and 150 μL of cold ACN was added to the sample followed by centrifuging it (5 min; 10 000 rpm). The supernatant was collected, and the formed pellet was considered as the protein bound fraction and its activity was measured with a dose calibrator and compared to the sample's total initial activity to determine protein bound fraction. The collected supernatant was centrifuged again (5 min; 10 000rpm) and the newly formed supernatant was collected and diluted with 200 μL of mQ water. The sample was injected to a radio-HPLC chromatography system to determine the % of intact radioligand. Both stability experiments were performed in triplicate.

4.1.8 Cell internalization

Freshly synthesized **16**, **19** or [^{64}Cu]CuCl$_2$ in PBS7.4 (350 kBq ; 3.9 μL) was mixed with RPMI-1640 cell culturing media (12 mL) containing 1% (vol/vol) Penicillin-Streptomycin

and 10% (vol/vol) fetal bovine serum. 1 mL of the media containing one of the radioactive agents was measured to wells of a 6 well plate which had been plated with 0.75×10^6 BxPC3 cells one day prior. The cells were incubated in the media for 2, 4 or 6 h at 37 °C. After the incubation period the unbound radioactive agent, the media was removed and the cells were washed with PBS7.4 (2×1 mL). To remove the surface bound agents, the cells were incubated in 0.05 M glycine (pH 2.9; 1 mL) over ice for 5 minutes. The glycine solution was removed, the cells were again washed with PBS7.4 (2×1 mL). Finally, the cells were lysed with 1 M NaOH (1 mL) over a 5 min period in room temperature. The cells were again washed with PBS7.4 (2×1 mL). The media, glycine solution, NaOH solution and the PBS washes were collected to separate Eppendorf tubes and measured on a gamma counter to determine the percentage of the unbound, membrane bound and internalized **16**, **19** or [^{64}Cu]CuCl$_2$. The experiment was done in triplicate for all timepoints.

4.1.9 *In vivo* profile of radioligands in healthy mice

<u>Blood half-life</u>

Blood half-life of **14**, **16-20** in healthy female nude mice (n=3/ligand) was measured by injecting one of the radioligands (0.82-7.4 MBq/nmol; 4.2-15 MBq in 100-200 μL of PBS7.4) to the tail vein intravenously. Because of the additional purification of **14**, the prepared doses of **14** included 20 % EtOH. Blood was drawn at six timepoints (2-120 min) from the saphenous vein. The blood collection tubes were preweighed to determine the mass of the collected blood. Activity of each sample was measured with a gamma counter. The percentage of injected dose per gram (%ID/g) values were presented as a function of time and a two-phase decay curved was formed from the plotted data. The y_0

was set to equal 50 %ID/g, because the total mass of the mouse blood pool was estimated to be 2.0 g based on the total weight of a nude mouse (20 g). The blood half-life was calculated with weighted average with equation 2, using the half-life values of the fast and slow phases ($t_{1/2fast}$ and $t_{1/2slow}$) and their relative percentage ($\%_{fast}$ and $\%_{slow}$) derived from the formed two-phase decay curve.

$$t_{1/2} = \frac{(t_{1/2\ slow} \times \%_{fast}) + (t_{1/2\ fast} \times \%_{slow})}{100} \tag{2}$$

In vivo PET imaging of **16** and **17**

Excretion and the pharmacokinetic profile of **16** and **17** were studied with PET imaging in healthy female nude mice. The injections of the radioligands were performed as described previously for the blood half-life experiments. The mice (n=3/radioligand) were imaged at three timepoints post radioligand injection (4, 8, 24 h) with either a 10- or 30-minute static scan.

4.2 DEVELOPMENT OF CB7 MODIFIED ANTIBODY

4.2.1 Synthesis of CB7 modified antibody

hT84.66-M5A antibody (M5A; 3.0 mg; 0.60 mL; 20 nmol; 1.0 eq.) in PBS7.4 was buffer exchanged into 2.0 mL of PBS (pH 8.7) with a PD10 desalting column (GE Healthcare). DBCO-C6-NHS ester (0.017 mg; 0.039 μmol; 2.0 eq.) in DMSO (3.1 μL) was added to the antibody solution and the reaction was agitated at 300 rpm for 60 min at 37 °C. The DBCO conjugated M5A (DBCO-M5A) antibody was purified with a PD10 column using

PBS7.4 for elution, which resulted in antibody recovery of 2.5 mg (yield: 83.0%). CB7-azide (0.11 mg; 0.083 μmol; 5.0 eq.) in DMSO (19 μL) was added to eluted DBCO-M5A (2.5 mg; 1 mL). The reaction solution was agitated at 300 rpm overnight at RT. The CB7-M5A was purified with a PD10 column using PBS (pH 7.4) for elution, which yielded 2.3 mg in of the modified antibody (overall recovery yield 77.0%).
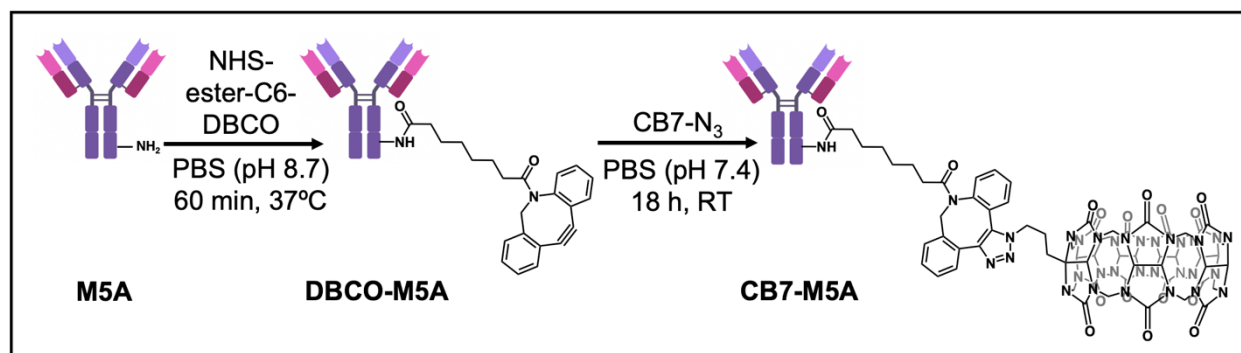
Figure 14. The reaction synthesis of the cucurbit[7]uril (CB7) modified hT84.66-M5A (CB7-M5A).

4.2.2 Characterization of CB7 modified antibody

To confirm that no aggregation or fragmentation of antibodies occurred during the CB7 modification procedure, CB7-M5A was ran on a fast protein liquid chromatography (FPLC) instrument using size exclusion chromatography (SEC).

The immunoreactive fraction of the CB7-M5A was determined via cellular binding assay (Lindmo assay) using CEA expressing BxPC3 cell line.[106,107] First, CB7-M5A (3.3 nmol) in 1 mL of PBS7.4 was radiolabeled by incubating it with **14** (10.6 nmol, 4.29 MBq, 0.40 MBq/nmol) for 5 min at RT. This was followed by purification of the CB7-M5A bound **14** with a PD10 size exclusion column. The radiochemical purity of the formed **14**-CB7-M5A

was determined with radio-TLC using iTLC-SG strips and 50 mM EDTA as the mobile phase. The antibody solution was diluted to 0.019 MBq/mL using 1% BSA in PBS7.4.

For the Lindmo assay, increasing numbers of BxPC3 cells were incubated with a standard amount of radiolabeled antibody (950 Bq). After 1 h incubation period, the cells were washed twice with cold PBS7.4 and the relative amount of radioactivity bound to the cells was measured with a gamma counter. The total added activity to the bound activity of each sample was presented as function of normalized cell concentration. Immunoreactivity was determined as the Y-intercept value which corresponds to the total activity to bound activity in a theoretical infinite number of cells.

The number of CB7 moieties per M5A was determined by fluorescence spectroscopy as follows. CB7-M5A (0.10 mg; 0.67 nmol; 1.0 eq.) was mixed with **13** (18 μg; 33 nmol; 50 eq.). The solution was left to incubate for 45 min at RT. The CB7-M5A bound **13** was purified with a Zeba Spin Desalting Column (7K MWCO, 0.5 mL, Fisher Scientific). The absorbance of the collected eluate was measured at 280 nm and 495 nm with a UV-Vis Spectrophotometer (Thermo Scientific NanoDrop). The number of **13** molecules bound to the CB7-M5A structure was calculated with the equation 3.

$$\frac{\text{Adma-FL}}{\text{CB7-anti-CEA M5A}} = \frac{\frac{\text{Abs(495 nm)}}{\varepsilon_{\text{fluorescein}}}}{\frac{\text{Abs(280 nm)-(CF(fluorscein)*Abs(495 nm)}}{\varepsilon_{\text{mAb}}}} \qquad (3)$$

The correction factor (CF) for fluorescein (FL) is 0.3 and its extinction coefficient ($\varepsilon_{\text{fluorescein}}$) is 68 000 M^{-1}cm^{-1}. It was assumed that each CB7 moiety was occupied by **13,** due to

large excess of the ligand (50 eq.) used. Non-specific binding of **13** to the M5A was also measured as described earlier.

4.3 DEVELOPMENT OF [⁸⁹Zr]Zr-DFO-M5A

4.3.1 Synthesis of DFO modified antibody

M5A (5.0 mg; 33 nmol; 1.0 eq.) in PBS7.4 was buffer exchanged to PBS (pH 8.4) using a PD10 desalting column. p-SCN-Bn-Deferoxamine (0.12 mg; 160 nmol; 5.0 eq.) in DMSO (12 μL) was added to the antibody solution (2.0 mL). The solution was incubated at 37 °C for 1 h. DFO-M5A was purified with PD10 desalting column using PBS (pH 7.4) for elution. The DFO-M5A solution was concentrated using an Amicon Ultra-4 centrifugal filter unit (50 kDa).
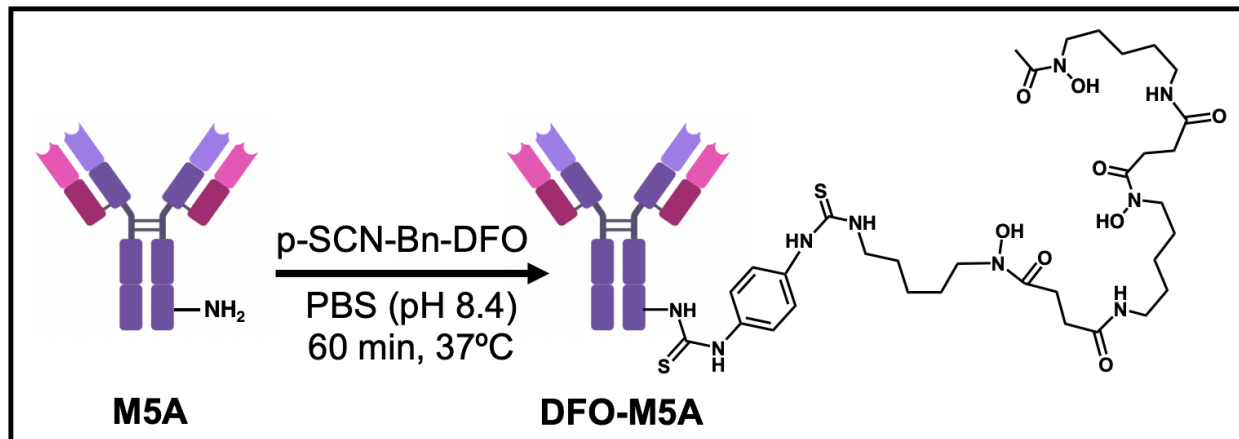
Figure 15. The reaction synthesis of the deferoxamine (DFO) modified hT84.66-M5A (DFO-M5A).

4.3.2 ^{89}Zr-radiolabeling

Zirconium-89 was produced with a cyclotron *via* ^{89}Y(p,n)^{89}Zr reaction. [^{89}Zr]Zr(C$_2$O$_4$)$_2$ (63-140 MBq; 20-30 μL) was pH adjusted to pH 7.4 using 1 M Na$_2$CO$_3$ and PBS7.4 (final volume of 200-500 μL). DFO-M5A (0.2-2.0 mg, 1.3-13 nmol, 4.3 mg/mL) was added to the pH adjusted solution. The solution was incubated at RT for 30-60 minutes. The labeling was monitored with radio-TLC using iTLC-SG strips with 50 mM EDTA as the mobile phase. The [^{89}Zr]Zr-DFO-M5A was purified using a PD10 desalting column and eluted with PBS7.4. The radiochemical purity was determined with radio-TLC using the same method as for labeling monitoring.

4.3.3 Characterization of DFO modified antibody

To confirm that no aggregation or fragmented antibody byproducts were formed during the DFO modification procedure, DFO-M5A was ran on an FPLC instrument using SEC. The immunoreactivity of the DFO-M5A was determined via Lindmo cellular binding assay with BxPC3 cell line using a [^{89}Zr]Zr-DFO-M5A. The assay was performed as described in section 4.2.2.

The number of conjugated DFO moieties per M5A was analyzed by a Bruker Impact II quadrupole time-of-flight (QTOF, Bruker Daltonics, Massachusetts, USA) system with an electrospray ionization (ESI) source. The DFO-M5A and M5A reference samples in PBS7.4 were desalted with a PD10 desalting column prior to the experiment. The elution of the samples off of the PD10 column were done with water resulting in final concentration of 1.0 mg/mL. The prepared antibody samples were introduced to the mass spectrometry system by UHPLC instrument. Data were collected in positive ion mode.

The average mass difference between the DFO-M5A and M5A was calculated and deconvoluted. The mAb samples were run in triplicate.

4.4 CEA EXPRESSION

To confirm and establish the CEA expression of two pancreatic cancer cells, Western Blotting was performed with the cell lysates of BxPC3 and MIAPaCa-2. The lysates were obtained by incubating the cells with the Cell Lysis Buffer II containing PMSF protease inhibitor and HaltTM Protease inhibitor cocktail. Protein quantification was performed with Pierce™ BCA Protein Assay Kit. The protein lysates were prepared in NuPAGE LDS Sample buffer. Each protein sample (20 μg) was separated by SDS-PAGE using a NuPAGE™ 4 to 12%, Bis-Tris, 1.0–1.5 mm, Mini Protein Gels at 100V for 15 minutes followed by an increase to 150V for an additional 60 minutes. Proteins were transferred electrophoretically onto Invitrolon™ PVDF/Filter Paper Sandwiches at 100 V for 60 minutes. Membranes were blocked in 5% Non-Fat Dry Milk prepared in TBS Tween™20 Buffer for 1 hour and incubated with the primary antibodies overnight at 4°C. The primary antibodies used were CEA Monoclonal Antibody (H.426.3) (ThermoFisher Scientific), beta Tubulin Loading Control Monoclonal Antibody (BT7R) (ThermoFisher Scientific) and hT84.66-M5A. The membranes were washed with TBS Tween™20 Buffer followed by incubation with the respective secondary antibodies (Goat anti-Mouse IgG (H+L), Superclonal Recombinant Secondary Antibody, HRP and Goat anti-human IgG FC Antibody, Horseradish Peroxidase HRP conjugate, cross absorbed) at room temperature for 1 hour. Western blots were developed using Pierce™ Fast Western Blot Kit, ECL

Substrate. Immunoreactivity was detected on a Konica Minolta SRX-101A Medical Film Processor.

4.5 BIODISTIRBUTION AND IMAGING STUDIES IN XENOGRAFT MODELS

The mice were housed in static microisolator caging with corn cob bedding (The Anderson Bed-o'Cobs 1/8"). The food provided was Lab Diet 5053 Irradiated PicoLab Rodent Diet 20. The mice were housed in 12-hour light/dark cycles. The mice were maintained in maximum isolation rooms, which are health monitored quarterly for pathogens and ecto/endo parasites. For experiments including xenografts, the mice were injected subcutaneously with BxPC3 or MIAPaCa-2 cells (5-6 $\times$ 10^6 cells in cells' media and matrigel, 1:1 %V/V; 150 μL) on their right shoulder or flank. The mice were used once the tumor volume reached ~100 mm^3 which occurred 5-6 weeks after implantation of the xenografts.

All the injections of modified mAbs and radioligands were performed intravenously *via* the tail vein. All the described *in vivo* biodistribution experiments were performed as follows. The mice were euthanized by inhalation of 5 % isoflurane with a 2.0 mL/min flow followed by a cervical dislocation. Blood, tumor, heart, lungs, stomach, liver, pancreas, spleen, small intestine, large intestine, kidneys, muscle and bone were harvested and placed to preweighed tubes. The contents of the small and large intestines were collected along with the tissue material. To determine each organ sample's %ID/g value, the samples were weighed and counted with a gamma counter.

Prior to the PET imaging experiments, the mice were anesthetized by inhalation of 2.5 % isoflurane with a 2.0 mL/min flow. The mice were kept under anesthesia and kept warm

with an infrared lamp for the duration of the scan. The imaging was performed with a Siemens Inveon PET/CT. The energy and time coincidence windows used for the scans were 350 – 650 keV and 3.432 ns. Data from all possible lines of response (LOR) were saved in the list mode raw data format. The raw data was then binned into 3D sinograms with a span of 3 and ring difference of 79. The images were reconstructed into transaxial slices (128 x 128 x 159) with voxel sizes of 0.800000 x 0.800000 x 0.7999150 mm^3, using the MAP algorithm with 16 subsets and 18 iterations at a beta value of 0.00427838.

4.5.1 *In vivo* profile of [^{89}Zr]Zr-DFO-M5A

To study M5A antibody's pharmacokinetic and excretion profile over several day period *in vivo*, [^{89}Zr]Zr-DFO-M5A was injected to BxPC3 tumor bearing male nude mice. The experimental cohorts (n=3-4) received varying amounts of the [^{89}Zr]Zr-DFO-M5A (0.33 nmol, 0.67 nmol or 1.0 nmol; 5.3-6.7 MBq in 100 μL PBS 7.4). The control, blocking cohort received the highest dose of the antibody (2.3 nmol; 5.4 MBq). The mice were euthanized for *in vivo* biodistribution either 4, 24, 72, 120 or 240 h post radiotracer injection. The biodistribution studies with the two earliest timepoints (4, 24 h) were only performed with a 0.67 nmol dose in order to get a more comprehensive *in vivo* profile of the antibody for a dosimetry analysis with one of the doses. The mice from the last timepoint of the 1.0 nmol dose cohort were imaged with a PET scanner (15 min static scan) 72, 120 or 240 h post injection.

The *in vivo* biodistribution of [^{89}Zr]Zr-DFO-M5A was also studied in another mouse model of MIAPaCa-2 tumor bearing female nude mice which acted as the negative control: The mice (n=4) were injected with [^{89}Zr]Zr-DFO-M5A (0.67 nmol; 3.3 MBq) and imaged with a

PET scanner (15 min static scan) 72 h post injection followed by sacrificing them for *in vivo* biodistribution studies.

4.5.2 Pretargeting studies of ferrocene radioligands

<u>Pretargeting with **15**</u>

The experimental groups including three cohorts of BxPC3 tumor bearing nude mice (n=3-4) were administered CB7-M5A (150 μg, 1.0 nmol; 150 μL in PBS7.4). 72 h later the mice received **15** (6.3-7.9 MBq/nmol, 1.5 nmol, 9.4-12 MBq) in PBS7.4. Mice were sacrificed at 1, 2 or 4 hours after the radioligand injection. Mice in the 4 h timepoint cohort were imaged on a PET scanner at 2 h and 4 h post injection, prior to euthanizing for biodistribution studies. In addition, a fourth cohort of BxPC3 tumor bearing mice (n=3) received only **15** (6.3-7.9 MBq/nmol, 1.5 nmol, 9.4-12 MBq). This control cohort was sacrificed 2 h after the radioligand injection.

<u>Pretargeting with **16** and **17**</u>

Experimental cohorts (n=4-5) of BxPC3 tumor bearing female nude mice received CB7-M5A (0.67 nmol; 100 μg; 100 μL in PBS7.4) followed by injection of either **16** or **17** (2.8-3.3 MBq; 1.5 nmol, 100 μL of PBS 7.4) 72 h later. Control cohorts of the same mouse model (n=4-5) received only **16** or **17** with no prior injection of CB7-M5A. Mice were sacrificed 1, 4, 8 or 24 h post radioligand injection for *in vivo* biodistribution. The biodistribution timepoints of 1 and 4 h were included only in the pretargeting studies of

16, to obtain a comprehensive *in vivo* profile of one of the pretargeted ligands for a dosimetry study.

Pretargeting with varying lag times

BxPC3 tumor bearing female nude mice (n=4) first received CB7-M5A (0.67 nmol; 100 μg; 100 μL in PBS7.4). Then, after a 72, 144 or 216 h lag time, mice were injected with **16** (11 MBq, 1.5 nmol in 150 μL of PBS7.4). Mice were sacrificed 8 or 24 h post radioligand injection for *in vivo* biodistribution studies. Mice in the 24 h timepoint cohorts were additionally imaged with a PET scanner 8 and 24 h post radioligand injection prior to the biodistribution studies.

Pretargeting with varying CB7-M5A dosing

Three cohorts of BxPC3 tumor bearing female nude mice (n=4) were injected with varying amounts of CB7-M5A (1.0 nmol; 150 μg / 1.4 nmol; 200 μg / 2.0 nmol; 300 μg in 100 μL in PBS 7.4). Then, after a 144 h lag time, the mice were administered with **16** (11-12 MBq, 1.5 nmol in 150 μL of PBS 7.4). Mice were sacrificed 24 h post radioligand injection for *in vivo* biodistribution studies.

4.5.3 Pretargeting studies of adamantane radioligands

Pretargeting with **18**-**20** in BxPC3 xenografts

Experimental cohorts of BxPC3 tumor bearing female nude mice (n=4-5) were injected with CB7-M5A (0.67 nmol; 100 μg in 150 μL in PBS7.4) followed by 72 hours later with an injection of **18/19/20** (1.5 nmol; 10.2-13.9 MBq in 150 μL in PBS7.4). The cohorts were

euthanized for *in vivo* biodistribution 4, 8 or 24 h post radioligand injection. An additional cohort/timepoint for pretargeted **19** was assigned, which was euthanized 2 h post radioligand injection. The mice in the 24 h timepoint cohorts were imaged with a small animal PET scanner 4, 8 and 24 h post radioligand injection. The corresponding control cohort (n=4) for each ligand was injected only with the radioligand. The control cohorts were sacrificed for *in vivo* biodistribution 24 h post injection.

Pretargeting with **19** in MIAPaca-2 xenografts

A cohort of MIAPaCa-2 tumor bearing female nude mice (n=4) were injected with CB7-M5A (0.67 nmol; 100 μg in 150 μL in PBS7.4) 72 h before the mice were injected with **19** (1.5 nmol; 8.8-10 MBq in 150 μL in PBS7.4). The mice were imaged with a PET scanner 24 h post radioligand injection. Followed by the last imaging timepoint, the mice were euthanized for *in vivo* biodistribution studies.

Fractionated dosing of pretargeted **21**

Three experimental cohorts of BxPC3 tumor bearing female nude mice (n=4) were injected with CB7-M5A (0.67 nmol; 100 μg in 150 μL in PBS7.4). Two of the cohorts were administered with a single **21** (1.5 nmol; 12-15 MBq in 150 μL in PBS7.4) dose either 3- or 6-days post CB7-M5A injection. The double dose cohort (fractionated dosing) received an injection of **21** 3- and 6-days post CB7-M5A injection. A fourth cohort, the control cohort, was injected only with **21** with no prior CB7-M5A injection. The single dose cohort with the 6-day lag time administration schedule and the double dose cohort were imaged

with a PET scanner 2 and 4 h after each **21** injection. All the four cohorts were euthanized for *in vivo* biodistribution 4 h post each cohorts' final injection of **21**.

4.6 DOSIMETRY

The estimated dosimetry of [^{89}Zr]Zr-DFO-M5A and pretargeted **16** and **19** in an adult male (70 kg) was estimated based on the *in vivo* biodistribution of the three agents in BxPC3 tumor bearing female nude mice. The data for the dosimetry calculation were based on an average for four animals at each time point of 1, 4, 8 and 24 h for pretargeted **16**, 2, 4, 8 and 24 h for pretargeted **19** or 4, 24, 72, 120 and 240 h for [^{89}Zr]Zr-DFO-M5A. The %ID/g was obtained for all the collected organs. The biodistribution data was fitted using a linear interpolation between the adjacent timepoints. The linear function of each organ was used to interpolate the concentration at intervals of either 1 (copper-64) or 4 h (zirconium-89) to give a better estimate of the kinetics. For [^{89}Zr]Zr-DFO-M5A the integration time was 240 h (approximately 4 half-lives of zirconium-89) and for **16** and **19** the integration time was extended 48 h with the assumption that the %ID/g was constant after the first 24 h and the only change in concentration between 24 and 48 h was due to radioactive decay of copper-64. A trapezoidal approximation was then used to obtain the integral over the time intervals. These residence times were used to estimate the absorbed dose to a human subject using the OLINDA program with the adult human male model and no bladder clearance.[108] The dose to the rest of the body was not used in this calculation.

5. RESULTS

5.1 GUEST RADIOLIGANDS AND THEIR CHARACTERIZATION

5.1.1 The radiosyntheses of ferrocene and adamantane radioligands

All of the radioligands were synthesized with short synthesis times (<40 min) with high radiochemical purity (RCP) and radiochemical yield (RCY). Corresponding RCP and RCY, decay corrected to the start time of the radiosynthesis, for guest radioligands (**14**-**21**) are listed in **Table 4**. The RCY values are decay corrected to the start time on the synthesis.

Table 4. The radiochemical purity (RCP) and radiochemical yield (RCY) of the guest radioligands.

radioligand	RCP (%) n=3	RCY (%) n=3
[^{67}Ga]Ga-NOTA-PEG$_3$-Fc (**14**)	95.5 $\pm$ 0.4	33.9 $\pm$ 13.2
[^{68}Ga]Ga-NOTA-PEG$_3$-Fc (**15**)	96.7 $\pm$ 2.4	78.3 $\pm$ 10.2
[^{64}Cu]Cu-NOTA-PEG$_3$-Fc (**16**)	96.0 $\pm$ 0.5	92.8 $\pm$ 1.4
[^{64}Cu]Cu-NOTA-PEG$_7$-Fc (**17**)	97.8 $\pm$ 1.4	93.4 $\pm$ 1.5
[^{64}Cu]Cu-NOTA-Adma (**18**)	97.5 $\pm$ 1.0	97.6 $\pm$ 1.5
[^{64}Cu]Cu-NOTA-PEG$_3$-Adma (**19**)	98.3 $\pm$ 1.8	98.5 $\pm$ 0.7
[^{64}Cu]Cu-NOTA-PEG$_7$-Adma (**20**)	98.9 $\pm$ 0.7	96.7 $\pm$ 0.0
[^{68}Ga]Ga-NOTA-PEG$_3$-Adma (**21**)	95.7 (n=1)	95.1 (n=1)

5.1.2 Distribution coefficient

The *in vitro* lipophilicity of a compound can be characterized by measuring the compound's distribution coefficient (log D). As presented in the equation 1, the lower the

compound's log D value is, the more hydrophilic the molecule is. The log D value of each guest radioligand is listed in **Table 5**.

Table 5. Distribution coefficient (log D) and the overall molecular charge of the guest radioligands.

radioligand	log D	overall molecular charge
[^{67}Ga]Ga-NOTA-PEG$_3$-Fc (**14**)	-3.2 $\pm$ 0.1	+1
[^{64}Cu]Cu-NOTA-PEG$_3$-Fc (**16**)	-2.3 $\pm$ 0.3	0
[^{64}Cu]Cu-NOTA-PEG$_7$-Fc (**17**)	-2.2 $\pm$ 0.3	0
[^{64}Cu]Cu-NOTA-Adma (**18**)	-2.6 $\pm$ 0.0	0
[^{64}Cu]Cu-NOTA-PEG$_3$-Adma (**19**)	-1.9 $\pm$ 0.3	0
[^{64}Cu]Cu-NOTA-PEG$_7$-Adma (**20**)	-1.6 $\pm$ 0.2	0

The distribution coefficient of all the radioligands varied between -3.2 and -1.6. All the gallium-68-labeled and copper-64-labeled compounds had an overall molecular charge of +1 or 0 respectively. Amongst the synthesized ferrocene radioligands, as expected, **14** with an overall molecular charge +1 did possess a lower log D value compared to the other two ferrocene radioligands (**16**,**17**) which had an overall molecular charge of 0. When comparing the two ferrocene radioligands, **16** and **17**, with otherwise identical chemical structure, except in their number of PEG units, a difference in their log D value was not observed. However, a trend between the length PEG-linker and the log D value was observed between the adamantane ligands which again had similar chemical structure to them other than the length of their respective PEG-linkers. As the number of PEG-units increased from **18** to **19** to **20**, the log D value of the compound increased (-

2.6 ± 0.0; -1.9 ± 0.3; -1.6 ± 0.2). In the literature, the length of the PEG-linker of the compound is reported to positively correspond with its log D value however the opposite was detected here.[73]

5.1.3 *In vitro* stability and plasma protein binding

All in all, the *in vitro* stability of the ferrocene radioligands was measured to be lower compared to the adamantane radioligands. (**Figure 16**) By the last monitored timepoint at 4 h, the percentage of intact ferrocene radioligands in PBS7.4 varied between 76-87% and the corresponding values in bovine plasma were 76-86%. For the adamantane radioligands, the closest acquired monitoring timepoint to the 4 h was 6 h. At that timepoint, 93-99% of the adamantane ligands were intact in PBS7.4 and 94-99% respectively in human plasma. Moreover, the measured stability of the adamantane ligands remained extremely high >90% up to 24 h.

Based on the stability analysis of the samples with radio-HPLC, the observed degradation products of the radioligands did not include free gallium-67 or copper-64. The main observed degradation product of the ferrocene radioligands was suspected to be each ligand's more hydrophilic oxidized ferrocenium form. Ferrocene is reported to oxidize rapidly to ferrocenium in human plasma.[109]

At 1 h timepoint, plasma protein binding of the ferrocene and adamantane guest radioligands did not significantly differ even though higher plasma protein binding was observed with the adamantane ligands (**18**: 23.8 ± 6.6 % & **16**: 9.2 ± 2.0 %). Additionally, with the adamantane radioligands, the fraction of protein bound radioligand grew over

time to the last timepoint of 24 h (27.8 ± 2.1 (**18**); 30.5 ± 3.7 (**19**); 23.2 ± 2.1 (**20**)) Again,

the difference was determined not to be significant amongst these molecules (p>0.05).
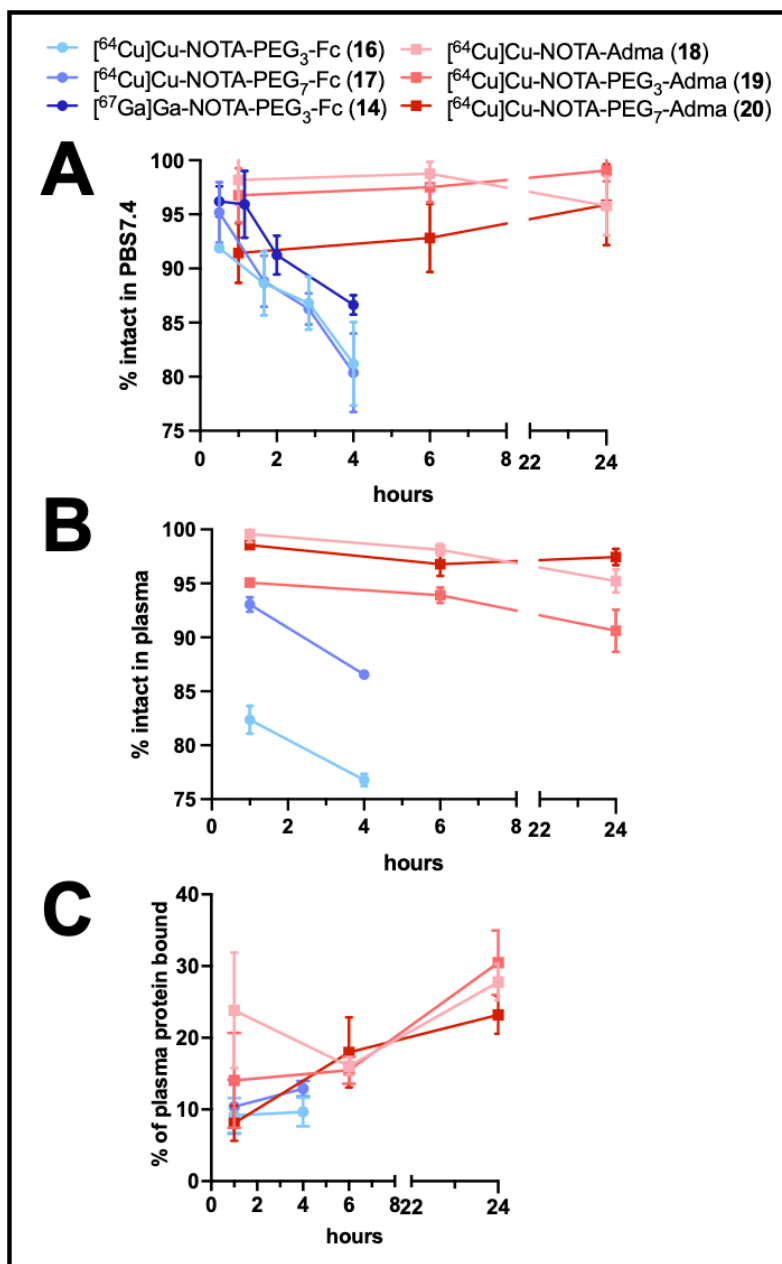
Figure 16. The *in vitro* stability of the radioligands in PBS7.4 (**A**) and in bovine or

human plasma (**B**) at 37 ºC as a function of time and their respective % plasma protein

binding (**C**).

5.1.4 Cell internalization of the radioligands

One of each guest radioligand type (a ferrocene and an adamantane) was chosen to determine the cell internalization capacity of the compounds. Neither of the studied radioligands, **16** or **19** showed any interaction with the BxPC3 cells. (**Figure 17**) Only 0.1 $\pm$ 0.0 % and 0.1 $\pm$ 0.1 % of **16** and **19** bound to the cell membrane and 0.2 $\pm$ 0.0 % and 0.0 $\pm$ 0.0 % got internalized after 6 h incubation period with the cells.

The experiment included the incubation of $[^{64}Cu]CuCl_2$ with the BxPC3 cell also to assess how 'free' copper-64 behaves with the cells. The cell internalization and membrane binding of $[^{64}Cu]CuCl_2$ was significantly higher compared to **16** (p=0.007 and p=0.002 at 6 h) and **19** (p=0.006 and p=0.002) indicating that both ligands remained intact for the duration of the experiment.
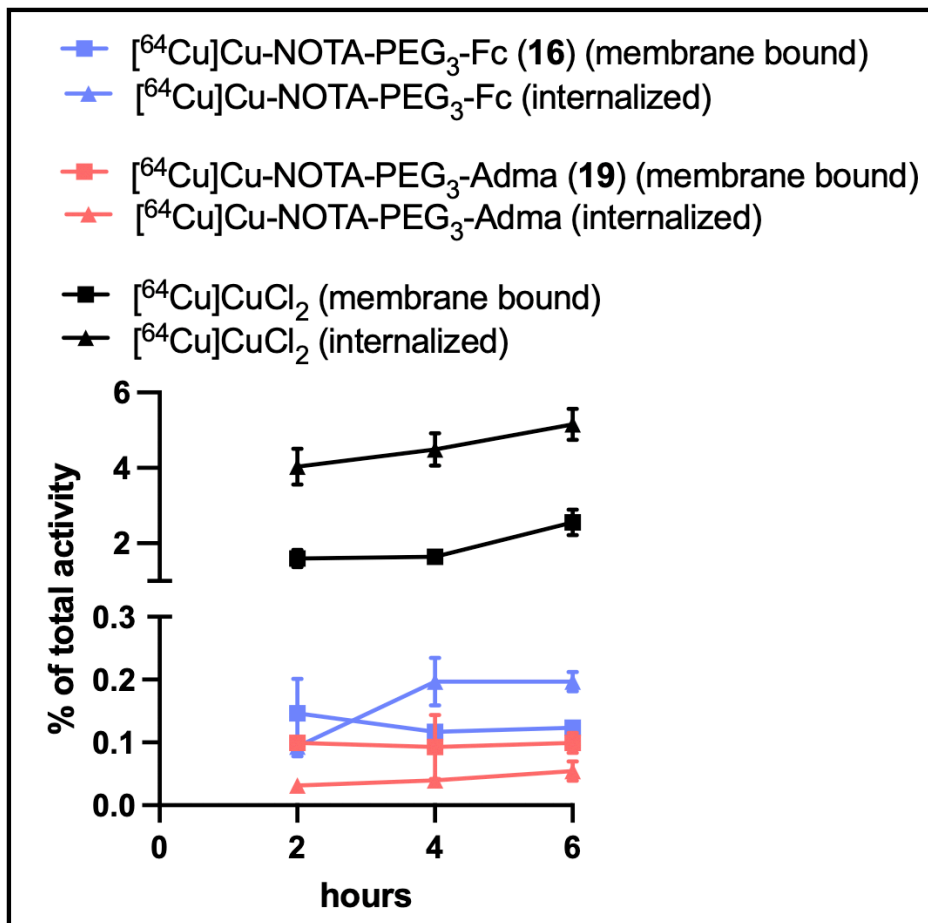
Figure 17. Cell internalization of the guest radioligands**.** The percentage of internalized and membrane bound [^{64}Cu]Cu-NOTA-PEG$_3$-Fc (**16**), [^{64}Cu]Cu-NOTA-PEG$_3$-Adma (**19**) and [^{64}Cu]CuCl$_2$ of the total added activity as a function of time with BxPC3 cells at 37 °C.

5.1.5 *In vivo* characterization of the radioligands

The blood half-life of all the radioligands **14**, **16-20** varied between 6.1-17.4 min. (**Table 6**) As with the distribution coefficient values of the radioligands, it was expected that the charge of the compound and the length of the PEG-linker would affect the blood half-life of the compound. Compound with a non-zero charge have shown to have a shorter blood

half-life compared to molecules with no charge. Comparing compounds **14** and **16**, which possess the same guest moiety (ferrocene) and PEG$_3$-linker but vary in the radiometal-chelator complex, **14** with a +1 charge has a slightly shorter blood half-life (10.0 min) than **16** (11.0 min) whose charge is zero. Additionally we can note that compounds with longer PEG-linkers have shorter blood half-lives. This trend was observed with ferrocene (**16** and **17**) and adamantane radioligands (**18**-**20**). Again, the assumption is that longer PEG-linkers would result in longer blood half-life values, due to their more hydrophilic nature. However, as it was discussed earlier, based on the log D values of the ligands, longer PEG-linkers produced less hydrophilic compounds. (**Table 5**) Hence, when the radioligands' log D values and blood half-life values are compared, the trend observed in their blood half-life values support the findings in the literature.[73]

Table 6. The blood half-life of the guest radioligands in healthy nude mice

radioligand	blood half-life (min)	overall molecular charge
[^{67}Ga]Ga-NOTA-PEG$_3$-Fc (**14**)	10.0	+1
[^{64}Cu]Cu-NOTA-PEG$_3$-Fc (**16**)	11.0	0
[^{64}Cu]Cu-NOTA-PEG$_7$-Fc (**17**)	6.7	0
[^{64}Cu]Cu-NOTA-Adma (**18**)	17.4	0
[^{64}Cu]Cu-NOTA-PEG$_3$-Adma (**19**)	13.8	0
[^{64}Cu]Cu-NOTA-PEG$_7$-Adma (**20**)	6.1	0

The whole-body *in vivo* profile of **16** and **17** in healthy female nude mice was assessed with PET imaging. Both radioligands expressed similar *in vivo* profile at the chosen imaging timepoints (4, 8 and 24 h post injection) (**Figure 18**). **16** and **17** were both

excreted through the hepatobiliary system relatively slowly. However, by the 24 h timepoint, signal from the gastrointestinal track had decreased to background levels as was the case with other organs.
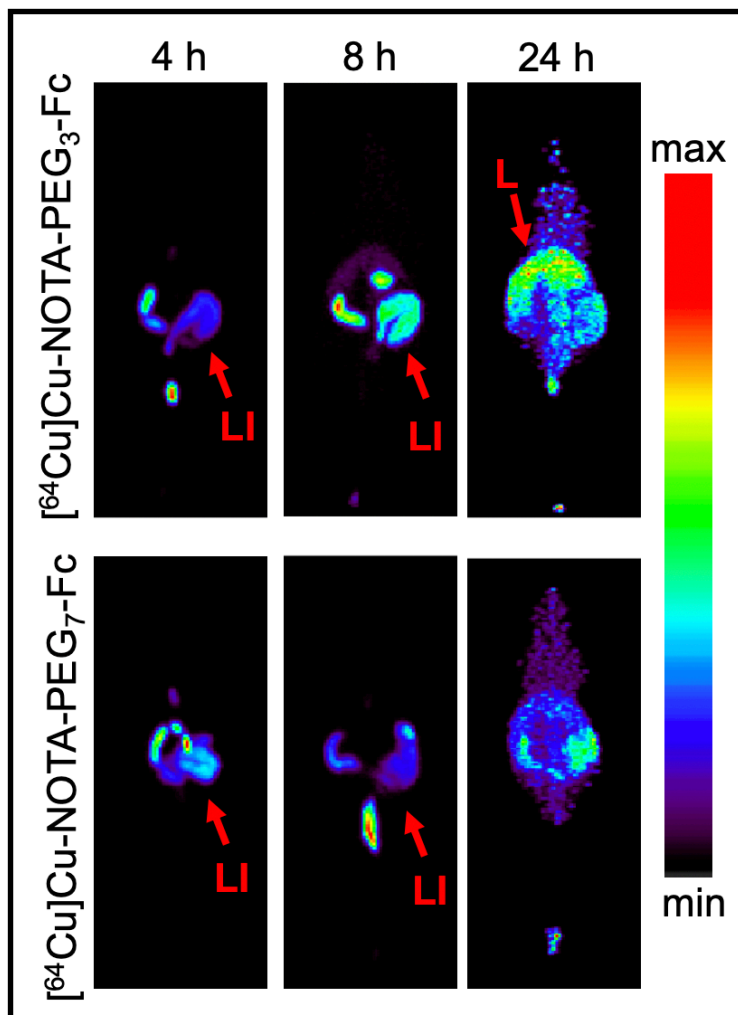
Figure 18. PET imaging of ferrocene radioligands in healthy mice. The maximum intensity projection PET images of the radioligand [^{64}Cu]Cu-NOTA-PEG$_3$-Fc (**16**) and [^{64}Cu]Cu-NOTA-PEG$_7$-Fc (**17**) in healthy female nude mice at 4, 8 and 24 h post radioligand injection. LI; large intestine, L; liver

5.2 CB7 MODIFIED ANTIBODY AND ITS CHARACTERIZATION

The two step CB7-M5A synthesis resulted in 77.0 % overall recovery yield. Based on the quality control of the modified antibody on SEC FPLC chromatography, the antibody did not aggregate or form any antibody fragments during the modification process. (**Figure 19**).

Figure 19. Quality control of CB7-M5A. FPLC chromatograph of the non-modified M5A (left) and the purified CB7-M5A (right) with detection of absorption of 280 nm.

Based on the spectrophotometry experiment with the purified CB7-M5A bound **13**, it was determined that each antibody was conjugated with an average of 0.8 ± 0.0 CB7 moieties. Once **13** was incubated with non-modified M5A, the degree of labeling was calculated to be -0.1 ± 0.0 and it was concluded that no non-specific binding of **13** to M5A occurred. (**Table 7**; **Figure 20**)

Table 7. The absorption at 280 nm and 495 nm for the purified M5A samples (DOL; degree of labeling)

	A $\lambda_{280\,nm}$	A $\lambda_{495\,nm}$	DOL
water	-0.00033 ± 0.0038	-0.0093 ± 0.0031	N/A
M5A + **13**	1.0700 ± 0.0174	-0.0303 ± 0.0126	-0.0867 ± 0.0309
CB7-M5A + **13**	1.0360 ± 0.0094	0.2407 ± 0.0042	0.7733 ± 0.0094
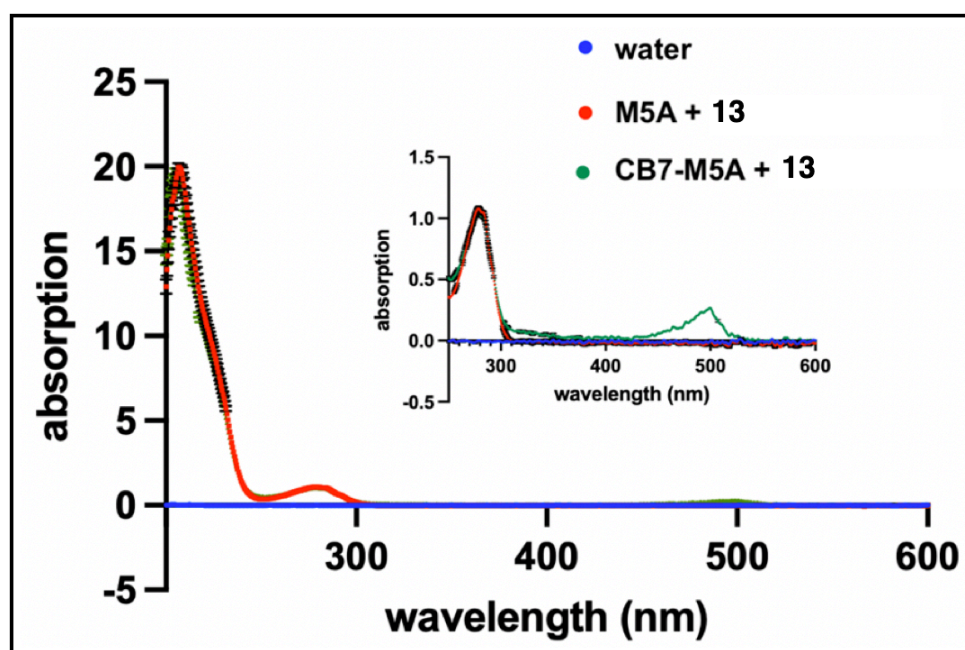
Figure 20. Absorption spectrum of the CB7-M5A bound adamantane-fluorescein (**13**). The absorption at two wavelengths, 280 nm and 495 nm were used to determine the number of CB7 moieties per M5A antibody.

After the CB7 conjugation, the immunoreactivity of the CB7-M5A antibody was measured with the Lindmo assay to remain high, 96 ± 0.70 % (n=3). The immunoreactivity was calculated based on the y-intercept of the line which was formed based on the cell

samples' total added activity/bound activity as a function of normalized cell concentration. (**Figure 21**)

CB7-M5A

$$y = 5.0359x + 1.0392$$
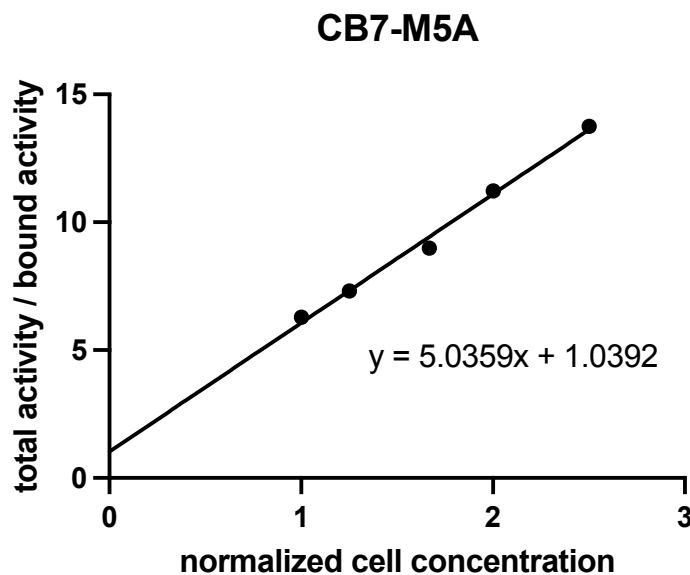
Figure 21. The cellular binding assay (Lindmo) of CB7-M5A with BxPC3 cells. Total activity/bound activity of the cells is presented as the function of normalized cell concentration.

5.3 DFO MODIFIED ANTIBODY AND ITS CHARACTERIZATION

DFO-M5A was synthesized with an overall recovery yield of 85.0 %. The quality control revealed the antibody remained intact during the modification process. (**Figure 22**) The number of DFO moieties per produced DFO-M5A was measured to be 1.0 ± 0.2. The results aligned with previously published data confirming that when the described conjugation conditions were used (p-SCN-DFO equivalents, pH, reaction time and temperature), a full-length antibody is conjugated with an average of one DFO moiety.[110]

The immunoreactivity of the DFO-M5A measured via [^{89}Zr]Zr-DFO-M5A was studied to be 90 ± 2.1% (n=3). (**Figure 23**)
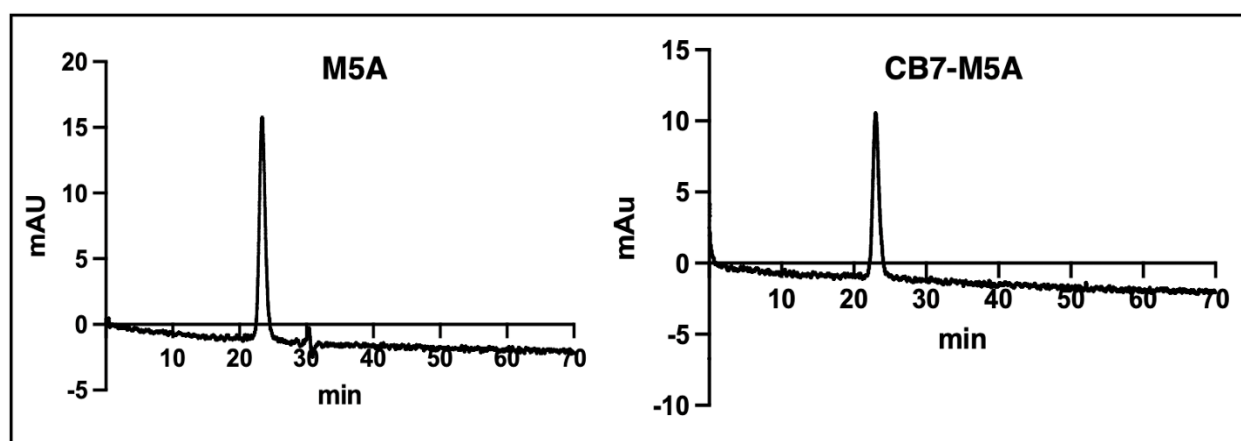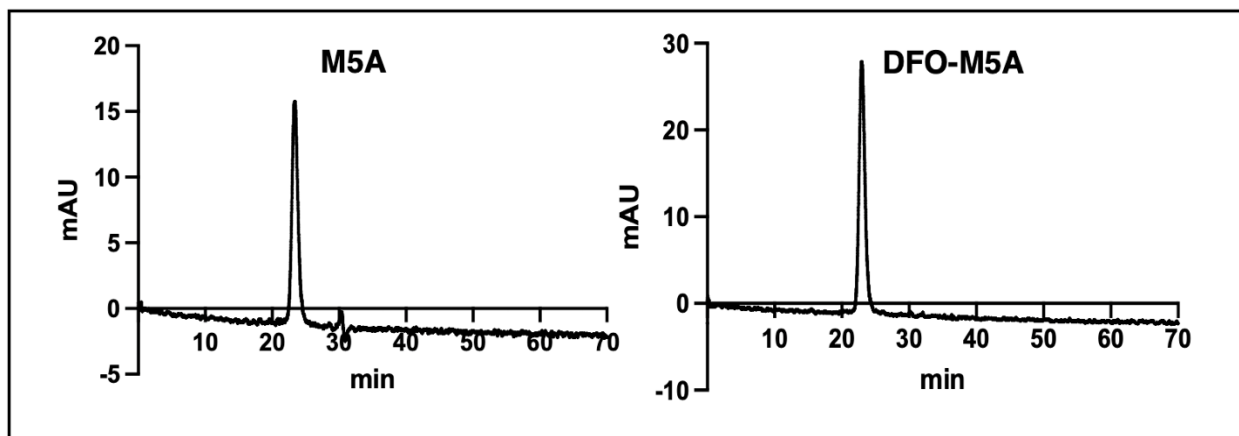

Figure 22. Quality control of DFO-M5A. FPLC chromatograph of the non-modified M5A (left) and the purified DFO-M5A (right) with detection of absorption of 280 nm.
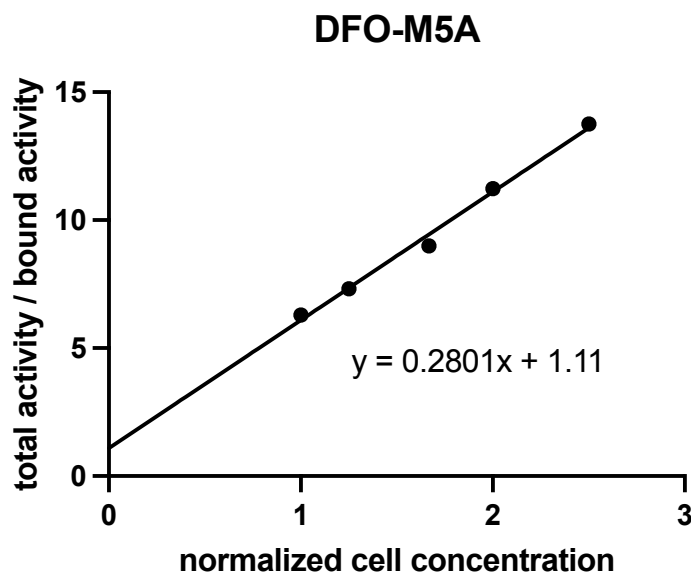
Figure 23. The cellular binding assay (Lindmo) of DFO-M5A with BxPC3 cells. Total activity/bound activity of the cells is presented as the function of normalized cell concentration.

5.4 CEA EXPRESSION

Based on the western blotting the BxPC3 cells are positive for CEA expression unlike the MIAPaCa-2. The findings align with previously published data.[107,111] The two primary anti-CEA antibodies used for blotting were commercial H.426.3 and a non-commercial hT84.66-M5A antibody. The latter was used throughout the discussed *in vivo* studies. Both of the antibodies demonstrated similar CEA expression for both of the cell lines. Because of the varying glycosylation patterns of different CEA isoforms, the band detected with BxPC3 was broad from 250 kDa to 50 kDa for hT84.66-M5A and 250 kDa to 100 kDa for H.426.3. (**Figure 24**)
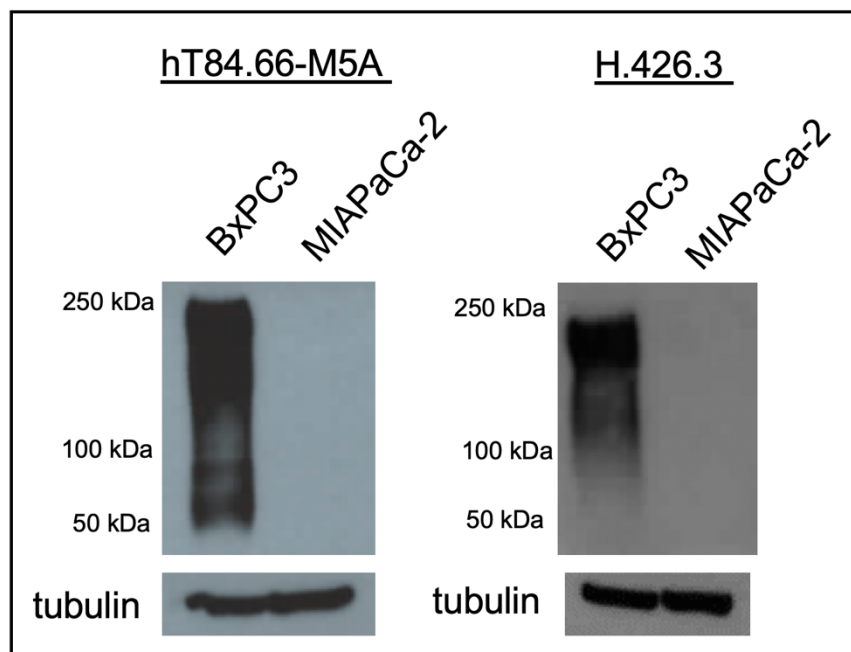
Figure 24. The Western Blotting of carcinoembryonic antigen (CEA). Expression studied in BxPC3 and MIAPaCa-2 cell lysates using two anti-CEA antibodies, ht84.66-M5A and H.426.3 as the primary antibodies.

5.5 BIODISTRIBUTION AND IMAGING STUDIES IN XENOGRAFT MODELS

5.5.1 *In vivo* profile of [^{89}Zr]Zr-DFO-M5A

The *in vivo* profile of [^{89}Zr]Zr-DFO-M5A in BxPC3 xenografted mice was determined by *in vivo* biodistribution at three different timepoints (72, 120 and 240 h). The *in vivo* profile of different antibody doses (0.33-1.0 nmol) were explored to assess what the ideal antibody dosing for the pretargeting strategy would be. Differing doses of [^{89}Zr]Zr-DFO-M5A did not affect tumor uptake in a statistically significant manner (**Figure 25**). The only statistical difference in the experimental cohorts' tumor uptake was observed with the lower tumor uptake of the 0.33 nmol dose compared to 0.67 nmol at the 120 h time point (31 ± 5.4

%ID/g & 66 ± 12 %ID/g; p=0.04). The tumor uptake for the 2.3 nmol dose, which was considered a blocking dose, was significantly lower (18 ± 1.0 %ID/g) compared to the 1.0 nmol dose (32 ± 5.8 %ID/g; p=0.02).

As expected, the presence of the antibody in the blood pool was significantly higher with the 1.0 nmol dose at 120 h (15 ± 0.6 %ID/g) and 240 h (13 ± 0.21 %ID/g) compared to the lower dose cohorts 0.3 nmol (120 h; 4.4 ± 2.9 %ID/g; p=0.03 and 240 h; 4.5 ± 1.1 %ID/g; p=0.007) and 0.67 nmol (120 h; 8.8 ± 0.9 %ID/g; p=0.002 and 240 h; 1.7 ± 1.6 %ID/g; p=0.01). Due to this trend, the highest [^{89}Zr]Zr-DFO-M5A dosing (1.0 nmol) resulted in lower tumor-to-blood ratios at 120 h (2.0 ± 0.62) and 240 h (3.5 ±0.11) timepoints compared to the 0.33 nmol (120 h; 27 ± 18 & 240 h; 12 ± 4.3) or 0.67 nmol (120 h; 7.8 ± 2.2 & 240 h; 37 ± 28) doses. (**Figure 26**) However, the differences were not found to be statistically significant.
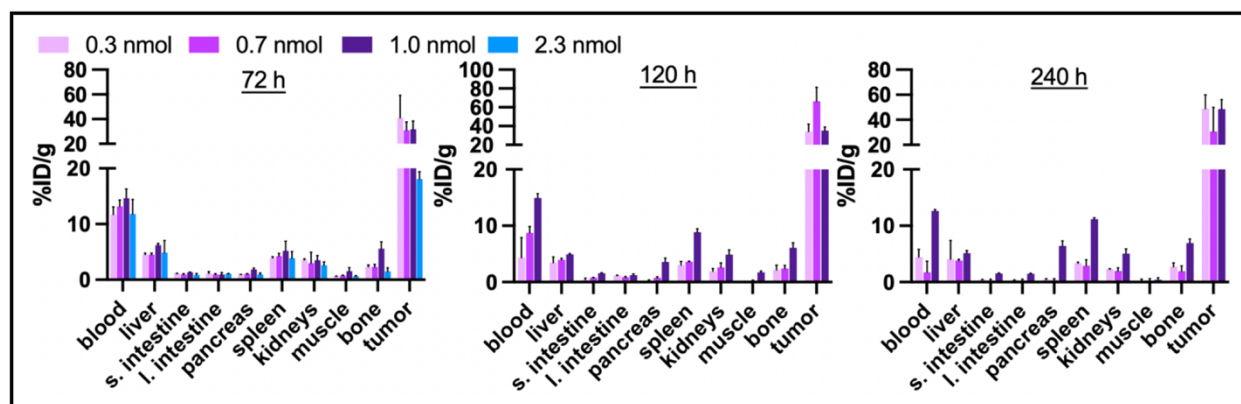
Figure 25. Activity biodistribution of varying amounts (0.3; 0.7; 1.0; 2.3 nmol) of [^{89}Zr]Zr-DFO-M5A in BxPC3 tumor bearing nude mice. The mice were sacrificed for *in vivo* biodistribution 72, 120 or 240 h post tracer injection.
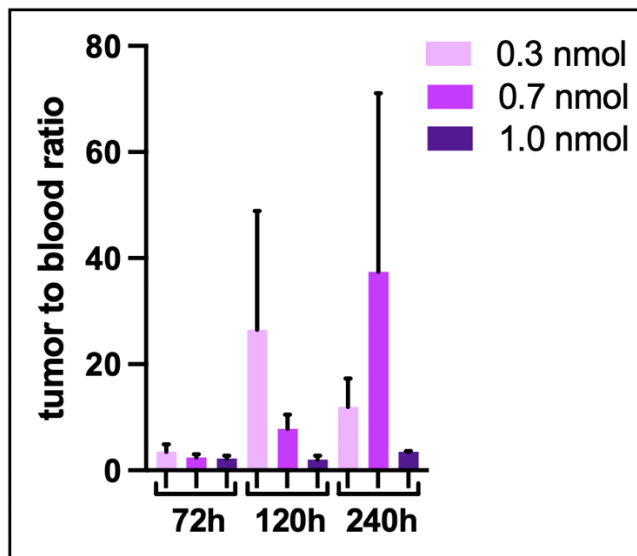
Figure 26. Tumor-to-blood ratio values of [^{89}Zr]Zr-DFO-M5A in BxPC3 tumor bearing male nude mice.
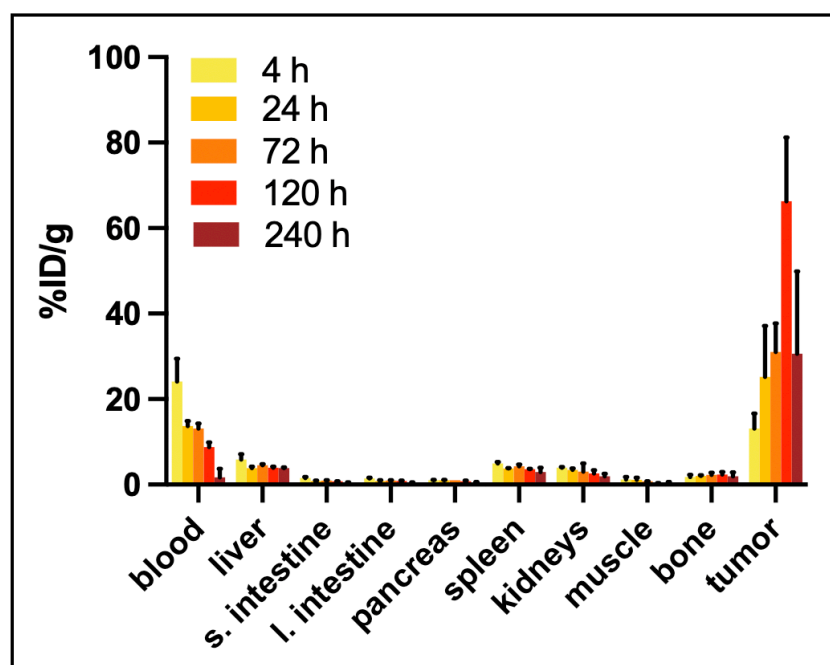
Figure 27. The full *in vivo* biodistribution of [^{89}Zr]Zr-DFO-M5A (0.67 nmol) in BxPC3 tumor bearing male nude mice. The biodistribution was performed at 4, 24, 72, 120 and 240 h post injection.

The two additional timepoints (4, 24 h) performed using the antibody dose of 0.67 nmol revealed as expected, that the presence of [^{89}Zr]Zr-DFO-M5A in the blood pool was significantly higher 4 h post injection (24 $\pm$ 4.6 %ID/g) compared to 24 h timepoint (14 $\pm$ 1.1 & p=0.03). However, the tumor uptake did not increase significantly between 4 and 24 h timepoints (13 $\pm$ 3.0 & 25 $\pm$ 9.7 %ID/g ; p=0.2) (**Figure 27**)

The *in vivo* biodistribution data aligned with the results obtained with the PET imaging of [^{89}Zr]Zr-DFO-M5A in the same mouse tumor model. (**Figure 28**) From the PET images, the tumor on the left flank was easily delineated on all the imaged mice. Based on the images, the tumor uptake varied between 62.0-71.2 %ID/mL, 41.3-47.1 %ID/mL and 56.6-64.8 %ID/mL at 72, 120 and 240 h timepoints respectively.
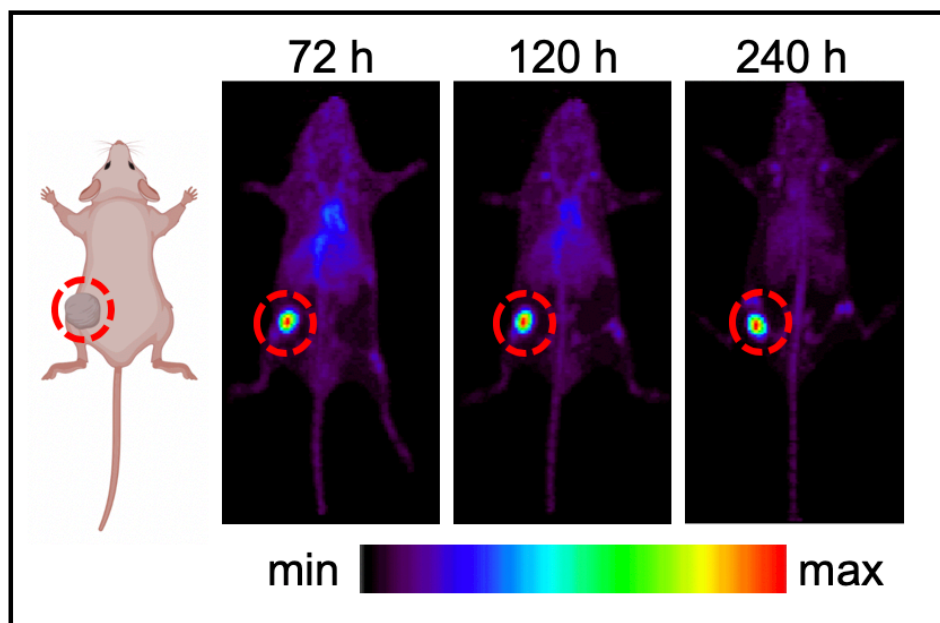
Figure 28. Maximum intensity projection PET images of [^{89}Zr]Zr-DFO-M5A (1.0 nmol; 7.4 MBq) in BxPC3 tumor bearing male nude mice. The subcutaneous tumor on the left flank is highlighted with a red circle.

The CEA positive, BxPC3 xenografts demonstrated higher tumor uptake compared to the CEA negative xenografts of MIAPaCa-2 (54 ± 10 %ID/g & 7.3 ± 0.3 %ID/g; p=0.004) (**Figure 27**,**29A**). The tumor mass was observed in all the imaged mice. (**Figure 29B**) The observed MIAPaCa-2 tumor uptake in the imaging and biodistribution experiments is expected to be result of permeability and retention effect which has been reported to occur in MIAPaCa-2 xenografts with full length antibodies.[112]
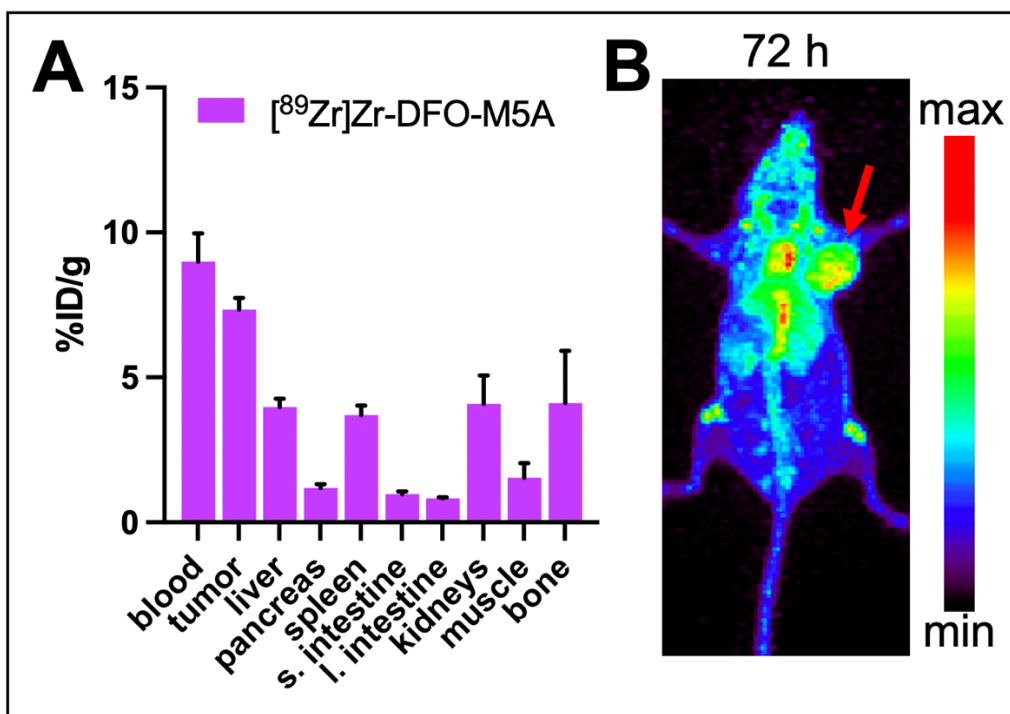
Figure 29. The *in vivo* profile of [^{89}Zr]Zr-DFO-M5A in MIAPaCa-2 tumor bearing female nude mice. **A**: The *in vivo* biodistribution of [^{89}Zr]Zr-DFO-M5A at 72 h post injection **B**: The maximum intensity projection PET image of [^{89}Zr]Zr-DFO-M5A at 72 h post injection. The location of the subcutaneous tumor on the right shoulder is highlighted with a red arrow.

5.5.2 Pretargeted ferrocene and adamantane radioligands

The presented work involved the development of a pretargeting platform based on a host-guest complexation *in vivo*. The first goal was to establish, that it was possible to utilize this non-covalent interaction for *in vivo* pretargeting and that the host and guest molecule bound to each other *in vivo*. Once this was established with pretargeting agents CB7-M5A and **15** in a xenograft model, the work mostly focused on optimization of the pretargeting strategy by synthesizing a library of radioligands and studying each ligand in *in vivo* pretargeting setting one at a time through rounds of optimization. In addition to optimizing the pretargeting strategy by adjusting the chemical structure of the radioligand, different lag times, dosing amounts and schedules were explored to understand the limitations and potential of this pretargeting methodology.

The results here are presented in the order of which the experiments occurred from establishing the efficacy of the novel pretargeting platform to exploring how different adjustments and changes in the pretargeting strategy affected its overall performance.

Establishing the formation of the host-guest interaction with pretargeted **15**

The purpose of these *in vivo* pretargeting experiments was to investigate the ability of **15** to bind specifically to CB7-M5A in a xenograft model. The goals of this study did not include optimization of the pretargeting parameters, but rather were focused on establishing the feasibility of the CB7-Fc based pretargeting.

Tumor uptake was significantly higher at 2 h p.i. in the pretargeting group (3.3 ± 0.7 %ID/g) compared to control (p=0.021). (**Figure 30**) Uptake in the liver, kidney and small

intestine decreased over the 4 h study period while uptake in the large intestine rose after 2 h.

The PET imaging showed excretion through the bladder and hepatobiliary system, which coupled with the location of the tumor resulted in poor visualization of the tumor 2 h post radioligand injection in two of three mice at the 2 h timepoint. However, after 4 h, the tumor mass was observed for all of the mice. (**Figure 31**)
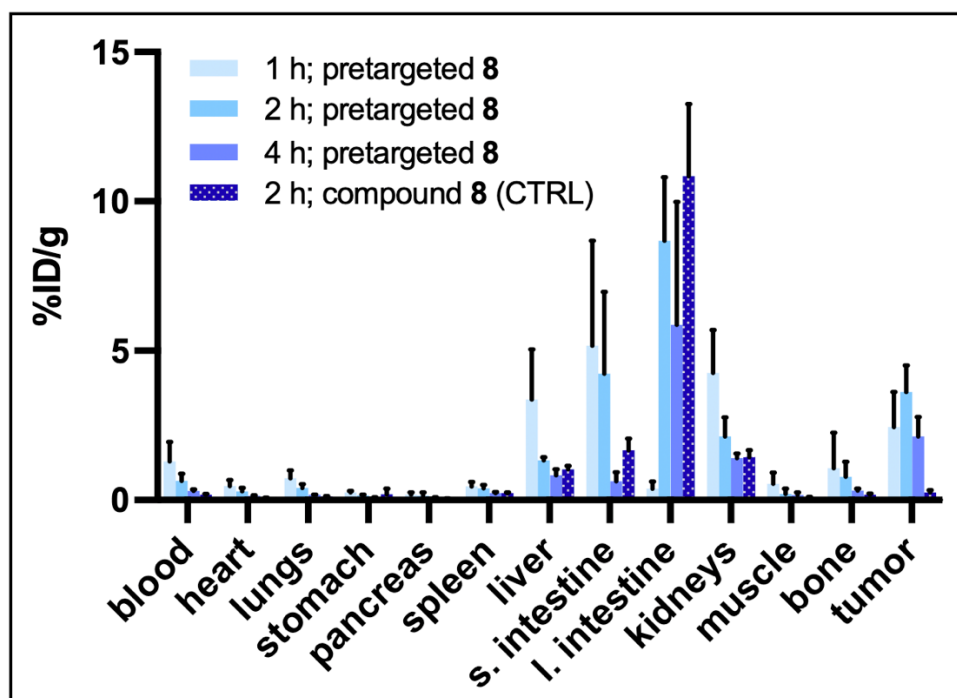
Figure 30. Biodistribution data for [^{68}Ga]Ga-NOTA-PEG$_3$-Fc (**15**) in BxPC3 tumor bearing mice. Mice received either CB7-M5A 72 hours prior to the radioligand administration (pretargeted; shades of blue) or the radioligand without a prior CB7-M5A dose (non-pretargeted; blue spotted pattern). The time values represent the amount of time after the radioligand administration.
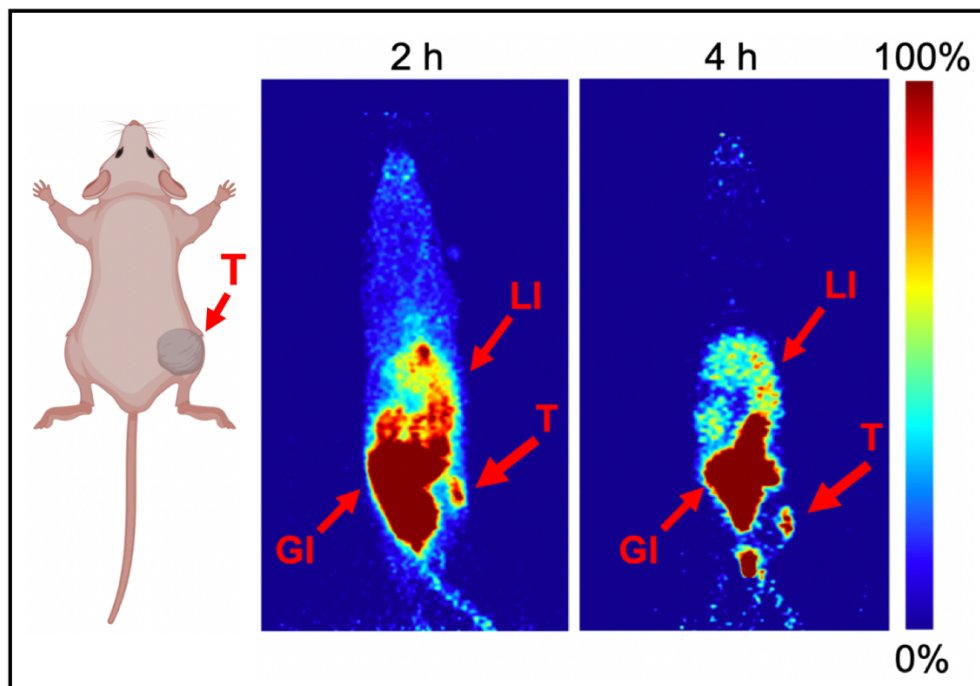
Figure 31. Maximum intensity projection PET images of pretargeted [^{68}Ga]Ga-NOTA-PEG$_3$-Fc (**15**) in female BxPC3 xenografted nude mice. The time values represent the amount of time after the radioligand administration and the arrows indicate the location of tumor (T), liver (LI) and gastrointestinal tract (GI).

Optimization of the CB7-Fc pretargeting strategy with second-generation ferrocene radioligands, **16** and **17**

In total, three sets of pretargeting studies were performed with **16** and **17**. In the first set of experiments, the pretargeting performance of the second-generation Fc-radioligands were compared using a 72 h lag time. Pretargeting with **16** showed specific tumor uptake at both 8 h (3.1 ± 0.6 %ID/g) and 24 h (1.5 ± 0.5 %ID/g) timepoints compared to non-pretargeted control cohorts (8 h: 0.2 ± 0.0 %ID/g p=0.0006 and 24 h: 0.1 ± 0.0 %ID/g p=0.0141) (**Figure 32**). However, pretargeting with **17** resulted in significantly higher

tumor uptake only at 8 h post injection (1.1 ± 0.3 %ID/g) compared to its time corresponding control cohort (0.0 ± 0.0 %ID/g; p=0.003) A drop in the tumor uptake values was observed at 24 h post injection with both of the radioligands. The lowered tumor uptake values of the pretargeted **17** at 24 h post injection resulted in uptake values that were not significantly higher than its corresponding control group at 24 h (0.5 ± 0.4 %ID/g & 0.0 ± 0.0 %ID/g; p=0.1) (**Figure 32B**). Of the two radioligands, **16** resulted in higher tumor uptake values at both investigated timepoints which was expected to be the result of its longer blood half-life value. (**Table 6**)

Both of the pretargeted ligands excreted mostly through the hepatobiliary system. Between the two pretargeted compounds, **16** and **17**, the difference in large intestine uptake was not statistically significant at 8 h (5.2 ± 0.8 %ID/g and 4.8 ± 1.1 %ID/g respectively; p=0.6) or at 24 h (0.1 ± 0.0 %ID/g and 0.1 ± 0.1 %ID/g respectively; p=0.9). At 8 h post injection, the large intestine uptake in the cohort which received the pretargeted **17** was significantly higher compared to its control cohort (4.8 ± 1.1 %ID/g & 1.8 ± 1.4 %ID/g; p=0.03).

At the 8 h timepoint, liver and kidney uptake was significantly higher for **16** (liver: 0.4 ± 0.1 %ID/g, kidney: 0.4 ± 0.0 %ID/g) compared to **17** (liver: 0.2 ± 0.1 %ID/g, kidney: 0.2 ± 0.0 %ID/g; p=0.009 and p<0.0001). The difference in compounds' liver and kidney uptake values was observed also at 24 h post radioligand injection (liver: p=0.02; kidneys: p=0.03). As for the signal in the blood pool, it was significantly higher for **16** compared to **17** at 8 h post injection (0.19 ± 0.05 %ID/g and 0.05 ± 0.03 %ID/g; p=0.003).
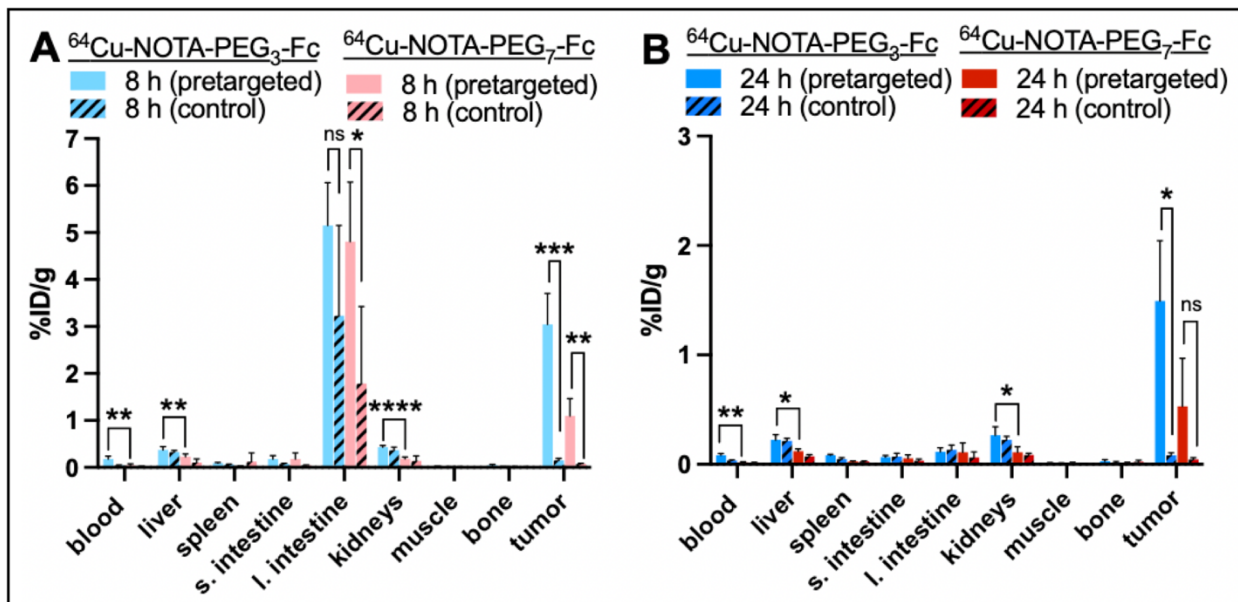
Figure 32. Biodistribution of pretargeted [^{64}Cu]Cu-NOTA-PEG$_3$-Fc (**16**, blue) and [^{64}Cu]Cu-NOTA-PEG$_7$-Fc (**17**, red) in BxPC3 tumor bearing female nude mice. The cohorts of mice were sacrificed at 8 h post injection (**A**) or 24 h post injection (**B**). Mice in pretargeting cohorts were injected with CB7-M5A 72 h prior to the radioligand injection. Mice in control cohorts were administered only the radioligand with no CB7-M5A. * p<0.05; ** p<0.01; *** p<0.001; **** p<0.0001; ns= not significant.

In the second set of our pretargeting experiments, **16** was studied in pretargeting setting *in vivo* with extended lag times. Cohorts of BxPC3 tumor bearing female nude mice first received the CB7-M5A. Then after a 72, 144 or 216 h lag time, **16** was administered. Mice were sacrificed 8 or 24 h post radioligand injection for biodistribution (**Figure 33**). Based on the *in vivo* biodistribution data, tumor uptake decreased as lag time increased (72 h; 3.1 ± 0.6 %ID/g; 144 h; 2.2 ± 1.1 %ID/g; 216 h; 1.1 ± 0.4 %ID/g at 8 h). With all the studied lag times, it was observed again that tumor uptake was higher at 8 h than at 24 h post injection (72 h; 1.7 ± 0.9 %ID/g; 144 h; 0.6 ± 0.1 %ID/g; 216 h; 0.4 ± 0.1 %ID/g at 24 h),

but the difference was significant only in cohorts which received the radioligand with 216 h lag time (p=0.02). As pretargeting lag time was increased, it was observed that it correlated negatively with the large intestine uptake (72 h; 5.2 ± 0.8 %ID/g, 144 h; 2.3 ± 0.3 %ID/g, 216 h; 1.3 ± 0.6 %ID/g at 8 h). At 24 h post radioligand injection, however, signal in large intestine decreased to similar levels (<0.3 %ID/g) across all three lag times. Difference in the tumor-to-blood ratio values between the cohorts was not found to be statistically significant (**Figure 33C**).
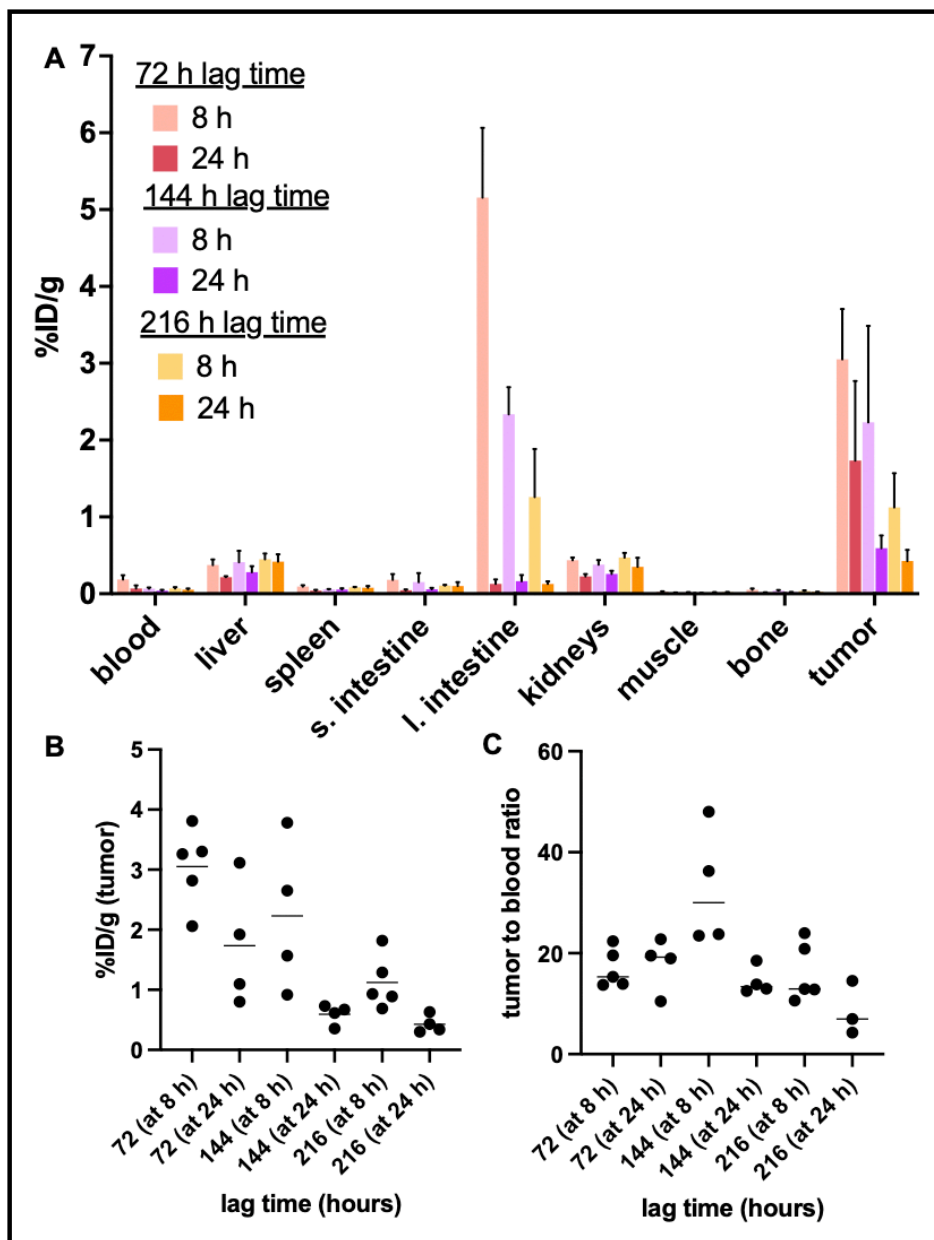
Figure 33. Pretargeted [^{64}Cu]Cu-NOTA-PEG$_3$-Fc (**16**) in BxPC3 tumor bearing mice with applied lag times of 72, 144 or 216 h. The biodistribution of the pretargeted **16** at 8 h and 24 h post injection (**A**), scatter plot of the radioligand tumor uptake at different timepoints with the investigated lag times (**B**) and the scatter plot displaying the tumor-to-blood ratio values of the different cohorts (**C**).

PET imaging experiments confirmed the findings of the lag time biodistribution studies. (**Figure 34**) Tumor signal could be clearly delineated from background signal at all three lag times. Based on the PET imaging study, at 8 h post radioligand injection, tumor uptake ranged from 6.9 ± 2.4 %ID/mL at the 72 h lag time to 2.6 ± 0.2 %ID/mL at the 216 h lag time. In turn at 24 h post radioligand injection, tumor uptake varied from 2.6 ± 0.9 %ID/mL at the 72 h lag time to 0.7 ± 0.1 %ID/mL at the 216 h lag time
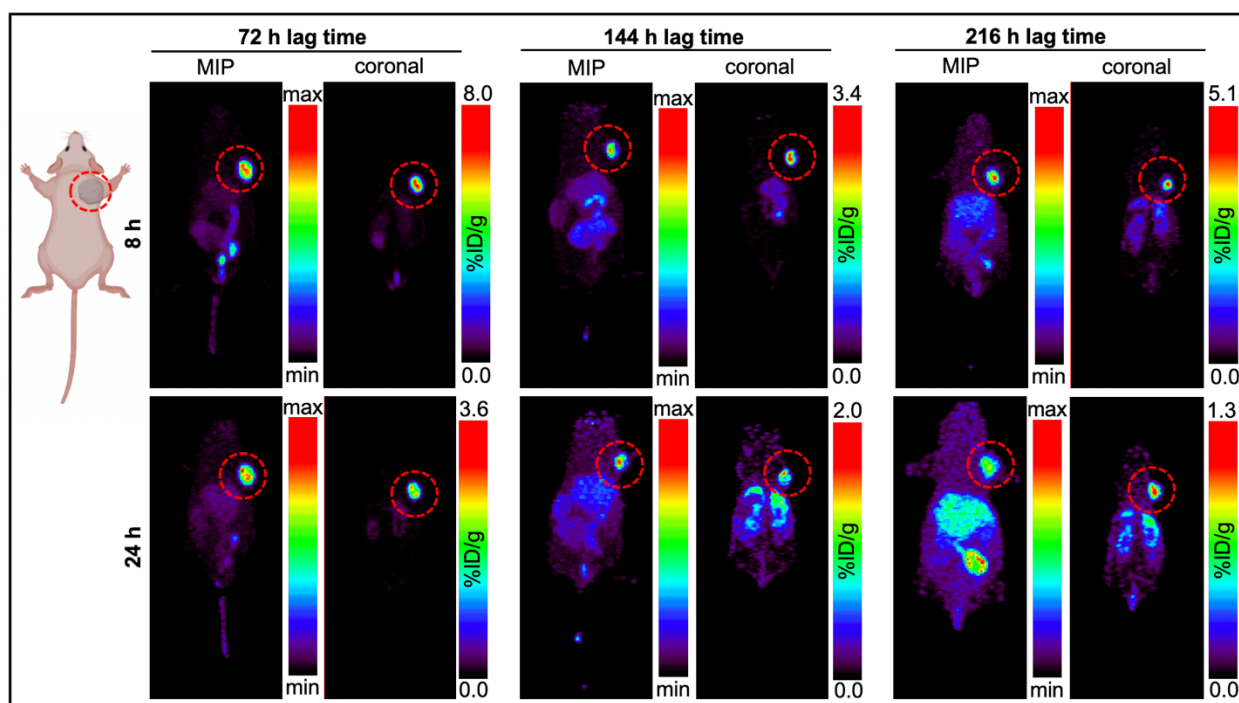
Figure 34. PET imaging of extended lag time pretargeting with CB7-M5A and [^{64}Cu]Cu-NOTA-PEG$_3$-Fc (**16**) in BxPC3 tumor bearing nude female mice. Lag time represents the amount of time between administration of CB7-M5A and **16**. The location of the subcutaneous tumor on the right shoulder is highlighted with a red circle. %ID/g; percentage of injected dose per gram & MIP; maximum intensity projection

The third and final pretargeting study with **16** explored the effects of varying the amount of CB7-M5A (1.0 nmol / 1.4 nmol / 2.0 nmol) used as part of the pretargeting protocol. We found that increasing CB7-M5A dose did not result in significantly higher tumor uptake. At the time the biodistribution was performed, 24 h post injection, tumor uptake was higher in the highest (2.0 nmol) dose (2.0 ± 0.5 %ID/g) cohort compared to both the 1.0 nmol (1.5 ± 0.4 %ID/g) and the 1.4 nmol dose (1.2 ± 0.3 %ID/g), though this difference was not statistically significant (1.0 nmol: p=0.5 & 1.4 nmol: p=0.1). However, these tumor uptake values were all higher than that of the 0.67 nmol CB7-M5A dose used in the two previous pretargeting experiments. Looking at the 0.67 nmol dose, we did find the 2.0 nmol dose to result in significantly higher tumor uptake (0.67 nmol: 0.6 ± 0.1 %ID/g, p=0.02). Signal in the blood was significantly higher in the cohort which received 2.0 nmol of CB7-M5A compared to lower doses. For instance, blood signal was 200 % higher for the 2.0 nmol dose (0.06 ± 0.01 %ID/g) compared to the 1.4 nmol dose (0.04 ± 0.01 %ID/g, p=0.02). (**Figure 35**)
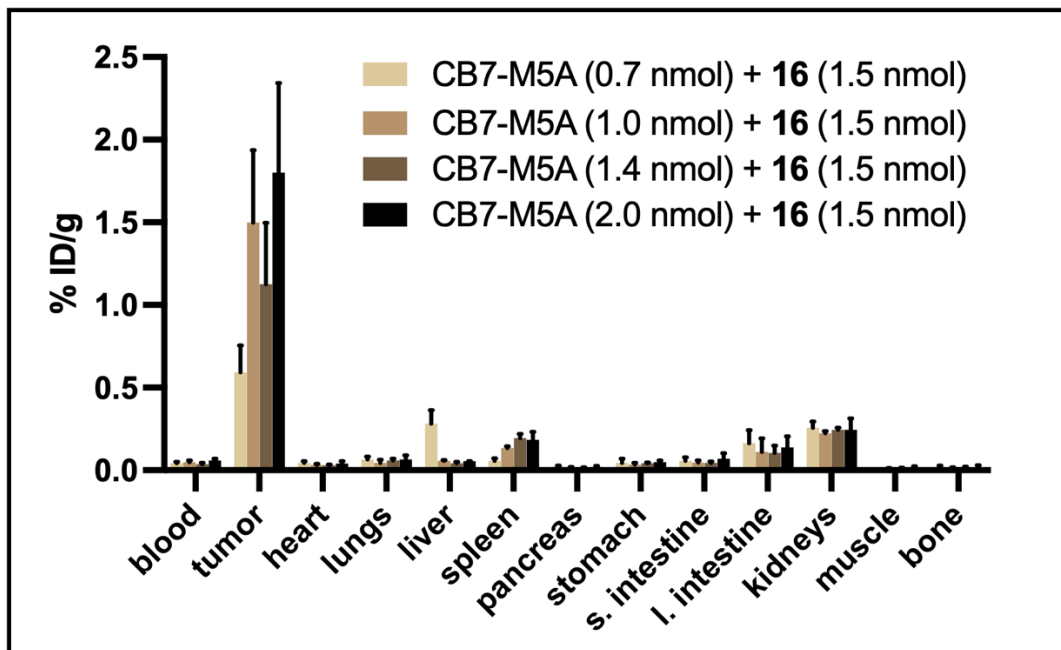
Figure 35. The *in vivo* biodistribution of the pretargeted [^{64}Cu]Cu-NOTA-PEG$_3$-Fc (**16**) in BxPC3 tumor bearing nude mice with varying CB7-M5A doses. The mice were administered with 0.7, 1.0, 1.4 or 2.0 nmol of CB7-M5A 144 hours prior to the injection of the radioligand. The biodistribution was done 24 hours post radioligand injection.

Switch from ferrocene to adamantane based guest ligands, **18**-**20**

Of the three Adma-radioligands, only pretargeted **18** and **19** demonstrated significantly higher tumor uptake compared to their respective control cohorts at 24 hours (**18**: p=0.005 & **19**: p=0.003, **Figure 36**). At 24 hours, pretargeted **20** resulted in almost 4 times higher average tumor uptake compared to its corresponding cohort (3.9 $\pm$ 2.1 %ID/g & 0.0 $\pm$ 0.0 %ID/g). However due to the high variance between the experimental samples, the tumor uptake between the cohorts was not significant (p=0.053). The tumor uptake increased overtime in all the cohorts, yet the highest average tumor uptake was reached with pretargeted **19** (**18**: 8.9 $\pm$ 2.0 %ID/g & **19**: 12.0 $\pm$ 0.9 %ID/g & **20**: 3.9 $\pm$ 2.1 %ID/g; **Figure**

37). The difference in tumor uptakes at 24 hours was not found to be statistically significant between pretargeted **18** and **19** (p=0.08).

The presence of all the Adma-radioligands in the blood pool was significantly higher in the pretargeting cohorts compared to their corresponding control cohorts (p=0.001, p=0.0006 and p=0.01 respectively for **18**, **19** and **20**) revealing that the Adma-radioligands bind to the CB7-M5A still circulating in the blood pool.

All the three pretargeted radioligands got excreted mostly through the gastrointestinal tract. The excretion was the slowest for pretargeted **20**. At 8 h post injection, the presence of **20** in the large intestine was significantly higher compared to **19**. However, by 24 h post injection the excretion was complete for all of the ligands (**18**: 0.1 $\pm$ 0.0%ID/g & **19**: 0.1 $\pm$ 0.0 %ID/g & **20**: 0.2 $\pm$ 0.1 %ID/g in large intestine).

Tumor-to-blood ratios increased overtime with all the pretargeted ligands. (**Figure 37**) The difference between the first and last timepoint was significant only with pretargeted **19** (4 h: 2.6 $\pm$ 1.5 & 24 h: 5.8 $\pm$ 0.4; p=0.008). Despite the higher tumor uptake values, of the pretargeted **18** and **19**, the tumor-to-blood ratio was similar for all the ligands at 24 hours (**18**: 4.7 $\pm$ 1.8; **19**: 5.8 $\pm$ 0.4; **20**: 4.5 $\pm$ 1.9), due to the lower presence of pretargeted **20** in the blood pool which was expected due to its shorter blood half-life.
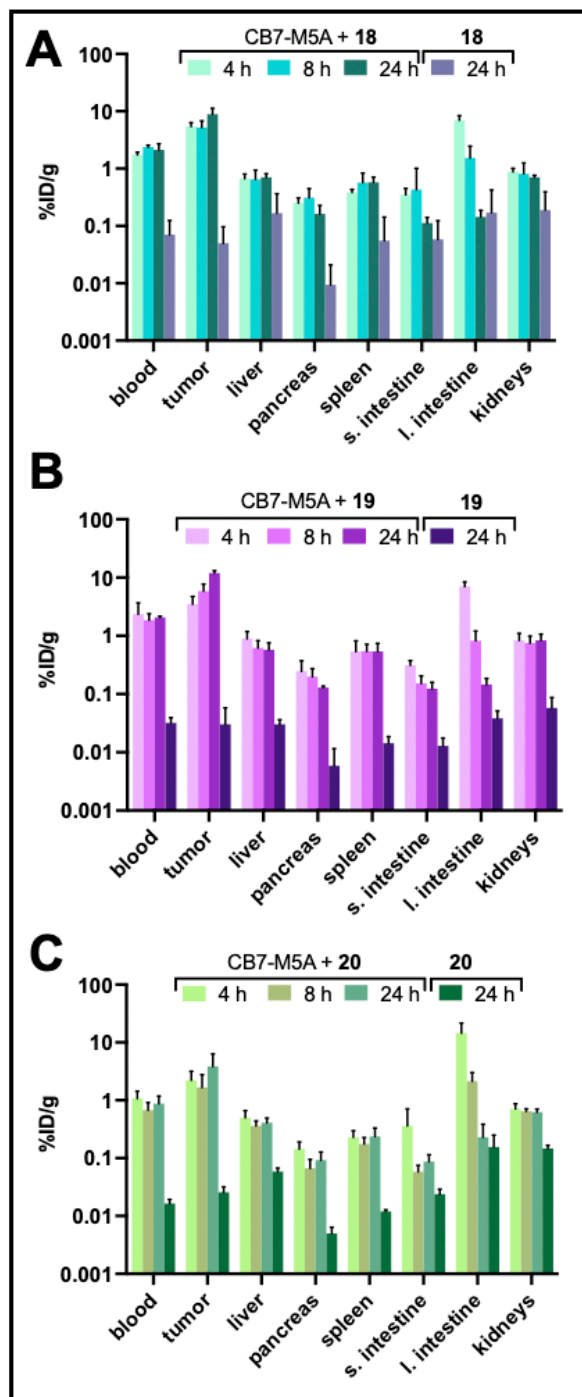
Figure 36. The *in vivo* biodistribution of pretargeted [^{64}Cu]Cu-NOTA-Adma (**18**), [^{64}Cu]Cu-NOTA-PEG$_3$-Adma (**19**) and [^{64}Cu]Cu-NOTA-PEG$_7$-Adma (**20**) in BxPC3 tumor bearing nude mice 4, 8 and 24 h post injection. %ID/g; percentage of injected dose.
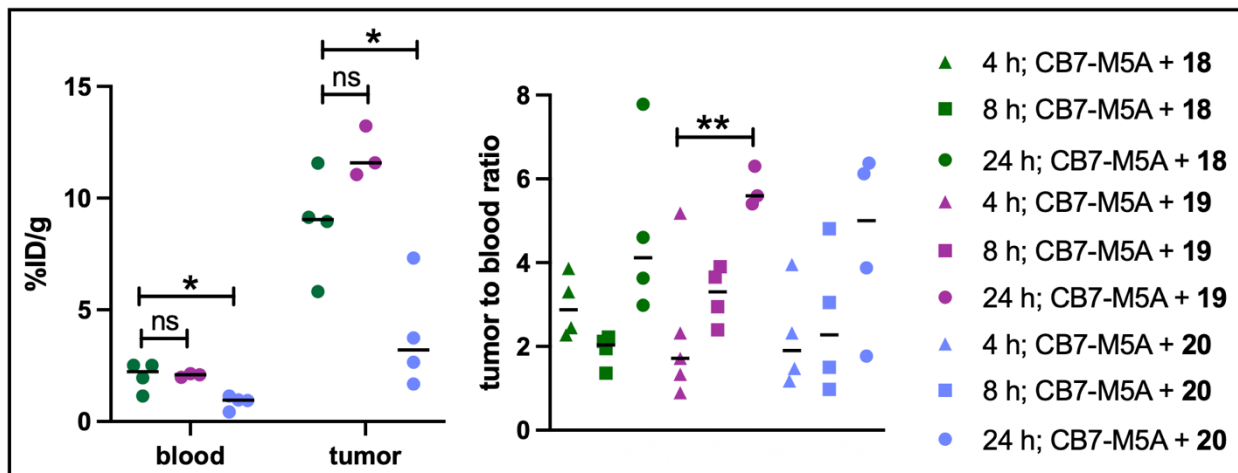
Figure 37. Scatter plot of the blood and tumor uptake and the tumor-to-blood ratios of pretargeted [^{64}Cu]Cu-NOTA-Adma (**18**), [^{64}Cu]Cu-NOTA-PEG$_3$-Adma (**19**) and [^{64}Cu]Cu-NOTA-PEG$_7$-Adma (**20**) at 4, 8 or 24 h post injection.

The PET imaging of the pretargeted **18**-**20** resulted in successful delineation of the tumor mass at all investigated timepoints (**Figure 38**). The images confirmed the *in vivo* biodistribution data, showing that the tumor uptake and tumor-to-background signal increased overtime up to the last timepoint. The tumor uptake of the pretargeted **18**-**20** varied between 3.8-17.1; 14.5-24.0; 2.8-13.1; %IDg/mL respectively at 24 hours post radioligand injection.
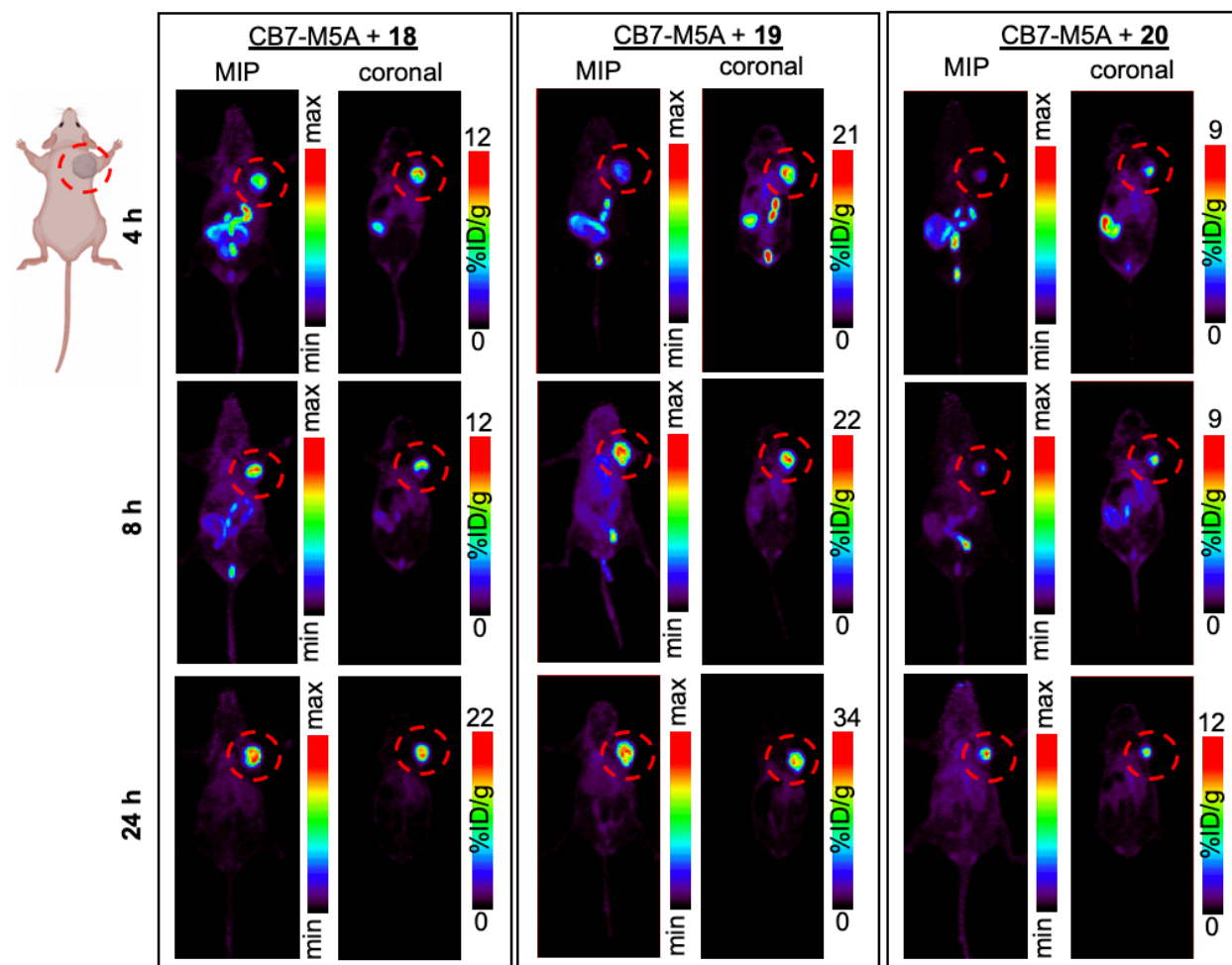
Figure 38. PET imaging of pretargeted adamantane radioligands in xenografted mice. Maximum intensity projection (MIP) and coronal slice PET images of the pretargeted [^{64}Cu]Cu-NOTA-Adma; **18**, [^{64}Cu]Cu-NOTA-PEG$_3$-Adma; **19** and [^{64}Cu]Cu-NOTA-PEG$_7$-Adma; **20** in BxPC3 tumor bearing nude mice at 4, 8 and 24 hours post radioligand injection. The mice were injected with CB7-M5A 72 h prior to the radioligand injection. The location of the tumor on the right shoulder is highlighted with a red circle.

Fractionated pretargeting with **21**

The tumor uptake was significantly higher in both pretargeted single dose cohorts compared to the control cohorts (3-day lag: p=0.0003 & 6 day lag: p=0.03). There was no

significant difference in the tumor uptake in any of the pretargeting cohorts (p>0.15 amongst all the cohorts). (**Figure 39**) Presence of **21** in the blood pool was significantly higher in the 3-day lag single dose cohort compared to the 6-day lag cohort (3-day lag: 2.0 ± 0.4 %ID/g & 6-day lag: 1.0 ± 0.4 %ID/g; p=0.03) This was expected due to the reduced presence of circulating CB7-M5A in the blood stream 6 vs. 3 days p.i. The reduced amount of **21** resulted in higher tumor to blood ratio for the 6-day lag pretargeting cohort compared to that with a 3-day lag (3.5 ± 0.4 vs. 2.6 ± 0.3; p=0.03).
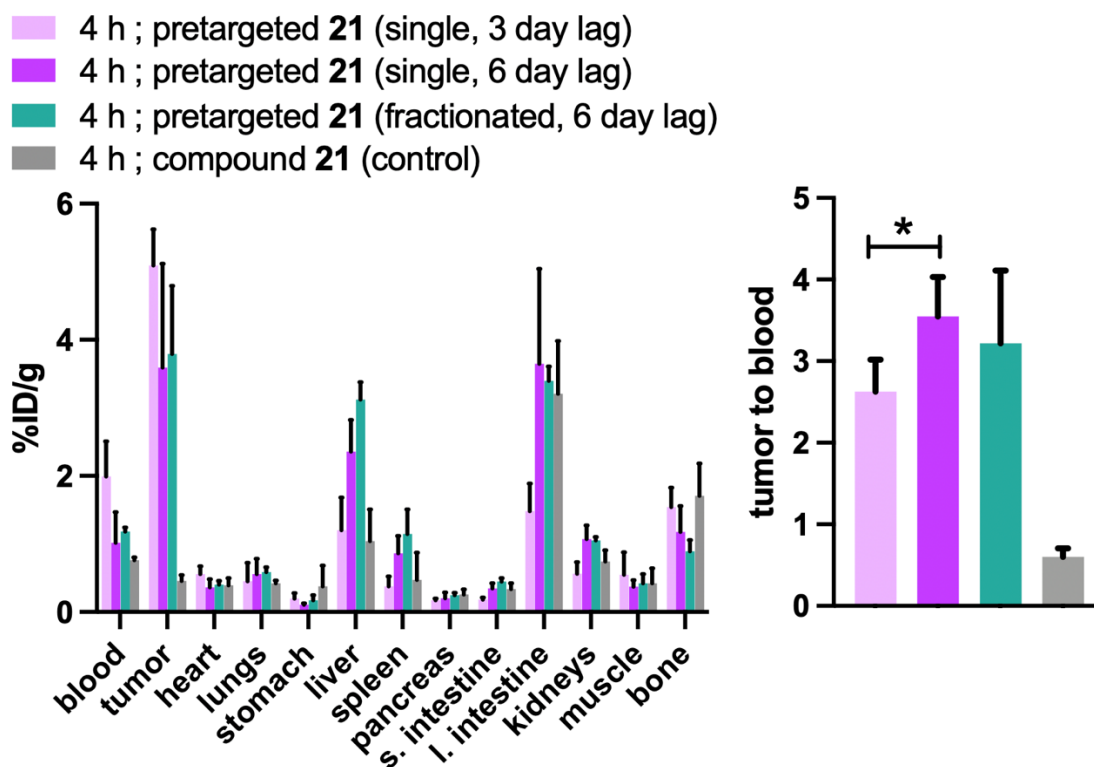
Figure 39. *In vivo* biodistribution of pretargeted [^{68}Ga]Ga-NOTA-PEG$_3$-Adma (**21**; single and double dose) with a 3- and 6-day lag times and the corresponding tumor-to-blood ratios at 4 h post injection of **21**. * p <0.05

The PET imaging of BxPC3 tumor bearing nude mice which were administered with a first or a second dose of pretargeted **21** 3 or 6 days p.i. of CB7-M5A resulted in the similar *in vivo* profile which was observed earlier in the *in vivo* biodistribution experiments. (**Figure 40**) The tumor was successfully delineated in all the mice that were imaged.
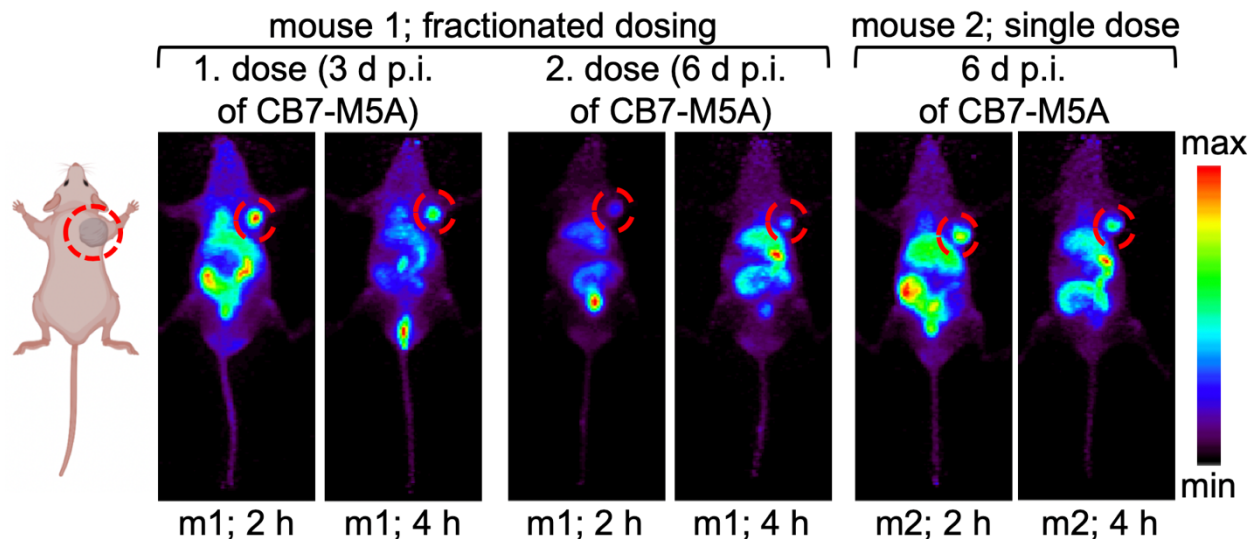
Figure 40. Maximum intensity projection (MIP) PET images pretargeted [^{68}Ga]Ga-NOTA-PEG$_3$-Adma (**21**) 2 and 4 h post injection. Mouse 1 (m1) was administered with two doses of **21**, 3 and 6 days post CB7-M5A injection. The m2 received only one dose of **21** 6 days post CB7-M5A injection. p.i.; post injection.

5.6 DOSIMETRY COMPARISON

The estimated radiation dose of an adult male from pretargeted **16** or **19** based on the mouse *in vivo* biodistribution demonstrated that both pretargeting approaches resulted in lower organ doses compared to the use of [^{89}Zr]Zr-DFO-M5A. (**Table 8**) In all the organs, the dose of the pretargeted **16** and **19** was at least one magnitude lower compared to

the directly radiolabeled M5A. The dose limiting organ for the use of the directly radiolabeled antibodies in humans is often red marrow and osteogenic cells.[6] Importantly, the estimated dose received from pretargeted **16** and **19** to the red marrow is only 0.7 and 1.4 % respectively of the red marrow dose estimated for the use of [^{89}Zr]Zr-DFO-M5A. Additionally the corresponding numbers for osteogenic cell doses were 0.7 and 1.3 %. The total body dose was lower for the pretargeted **16** compared to pretargeted **19** (1.26 vs 2.03 µSv/MBq). This was expected due to the longer presence of the pretargeted **19** in the blood pool compared to **16**.

Table 8. The estimated organ dose values of an adult human male from a dose of [^{89}Zr]Zr-DFO-M5A, pretargeted [^{64}Cu]Cu-NOTA-PEG$_3$-Fc (**16**) or pretargeted [^{64}Cu]Cu-NOTA-PEG$_3$-Adma (**19**) (µSv/MBq).

target organ	[^{89}Zr]Zr-DFO-M5A (µSv/MBq)	pretargeted [^{64}Cu]Cu-NOTA-PEG$_3$-Fc (**16**) (µSv/MBq)	pretargeted [^{64}Cu]Cu-NOTA-PEG$_3$-Adma (**19**) (µSv/MBq)
adrenals	280	2.3	2.5
brain	3.5	0.0010	0.016
esophagus	150	0.53	1.0
eyes	3.9	0.012	0.022
gallbladder wall	280	2.9	2.7
left colon	580	130	94
small intestine	230	23	10
stomach wall	220	1.9	2.7
right colon	410	70	50
rectum	57	0.88	1.0
heart wall	640	2.2	12
kidneys	520	9.0	14
liver	530	4.4	7.2
lungs	140	0.64	1.8
pancreas	280	3.7	5.1
prostate	46	0.59	3.3
salivary glands	6.4	0.021	0.037
red marrow	58	0.40	0.83
osteogenic cells	37	0.28	0.49
spleen	310	2.1	5.1
tumor	18000	130	670
thymus	160	0.29	0.97
thyroid	32	0.083	0.20
urinary bladder wall	73	0.48	2.2
total body	62	1.3	2.0
effective dose	860	16	40

6. DISCUSSION

6.1 COMPARISON OF THE GUEST RADIOLIGANDS

Three factors effecting lipophilicity

The distribution coefficient or lipophilicity is often considered to be an important parameter in the design of a radiotracer. The log D, measured *in vitro*, value can indicate the behavior of the molecule *in vivo*. Radiotracers that are very hydrophilic (low log D) are not able to diffuse through the cell membrane from the blood vessels as efficiently which limits the accumulation of the radiotracer to the target site. On the other hand, radiotracers with very high lipophilicity (high log D) express higher amount of non-specific binding and are more likely bind to plasma proteins, which in large amounts increases the background signal of a PET image. Due to these two undesirable extremes, the log D value of a radiotracer should not be too low or high. Often times log D values between 1-3 have proven to result in desirable target accumulation and background signal. However, exceptions to this rule exist.[113]

Three structural components were expected to have an effect on the lipophilicity of the guest radioligands: the overall molecular charge, the number of PEG-units incorporated to the compound, and the guest moiety (ferrocene/adamantane). The library of guest radioligands that were analyzed for their lipophilicity (**Table 5**) allows to compared ligands that are structurally similar in all other aspects expect on either their guest moiety (**16** vs **19**), number of PEG-units (**18** vs **19** vs **20**) or molecular charge (**14** vs **16**). Firstly, by comparing **16** and **19**, the adamantane guest moiety resulted in the molecule having a higher log D value, demonstrating the adamantane to be more lipophilic construct

104

compared to ferrocene. The findings were not surprising, due to low polarity of carbon-carbon bonds which an adamantane molecule is solely formed of. A ferrocene is composed of a Fe^{2+} cation that is sandwiched by two negatively charged cyclopentadienyl rings. It is reasoned that these formally charged moieties of a compound would make a molecule less lipophilic due to the enhanced solvation by water molecules via formed charge-dipole interactions.[73]

Secondly, by comparing the adamantane ligands with varying PEG-linker lengths (**18**-**20**) revealed surprisingly that higher number of PEG-units produced a more lipophilic compound. Based on the polarity of a PEG-linker, an opposite trend was expected. PEG-linkers are often used in medicine to alter and decrease the lipophilicity of a compound: The oxygen atoms of the ethylene glycol monomers make the PEG-linker a hydrophilic component due to the hydrogen bonding of the oxygen atoms between water molecules. The same trend was again not observed with two ferrocene radioligands, with varying PEG-linker lengths (**16**,**17**), which possessed similar log D values.

Finally, the molecular charge on the ligand resulted in a difference in the compounds' lipophilicity. **14** equipped with an overall molecular charge of +1 proved to have reduced lipophilicity compared to **16**, which possessed an overall molecular charge of 0. Positively or negatively charged compounds are often more hydrophilic than zero-charged compounds due to the ion-dipole intermolecular interactions that are formed between the charged moiety of the compound and the polar water molecules. This trend has been reported earlier in the literature.[73]

To further confirm and expand the trends which were observed in the lipophilicities of the different guest radioligands, ideally more compounds should be added to the compound

library. Since only one compound had a non-zero overall molecular charge, guest ligands with different overall molecular charges, negative and positive, should be included in the library to evaluate the effects of the charge on the lipophilicity of the compound.

<u>The compromised *in vitro* stability of ferrocene radioligands</u>

Establishing the stability of the guest radioligands was a major priority in understanding their potential as the radioligand component of the host-guest pretargeting strategy. In order for the pretargeting to occur the radioligand needs to remain intact and sustain the capability to interact with the modified antibody.

The *in vitro* stability of three ferrocene and adamantane radioligands were evaluated in PBS7.4 and bovine/human plasma at 37 ºC. With both ligand types the radionuclide-chelator complex remained intact. However the ferrocene guest moiety proved to have lower stability *in vitro* compared to adamantane moiety. Ferrocene is reported to quickly oxidize to ferrocenium form *in vivo* in rats.[109] After an intravenous dosing of a ferrocene derivative, the oxidation to ferrocenium is complete after only 5 min. In our studies, the main product noted on the radio-HPLC trace, was a more hydrophilic degradation product, which was expected to be an oxidized derivative of **14**, **16** and **17**. The formation of oxidized ferrocenium radioligand however is not a major concern in the application of pretargeting, since the reported dissociation constants between CB7 and plain ferrocene or ferrocenium lay in the same range ($K_{CB7 \cdot Fc} \geq 4 \times 10^5\,M^{-1}$ & $K_{CB7 \cdot Fc+} \geq 10^6\,M^{-1}$).[114] According to the electrostatic potential (ESP) profile of a CB7 molecule, the inner cavity remains relatively electronegative allowing the formation of host-guest complexes with positively

charged molecules and moieties such as ferrocenium with an overall charge of +1. The ESP of the outer surface of the CB7 cavity is significantly more positive.[91]

Certainly, due to the extremely high *in vitro* stability of the adamantane ligands, the adamantane-based radioligands appear more superior compared to ferrocene-based ligands. (**Figure 16**) Additionally the stability of an adamantane *in vivo* has been widely established previously in the myriad of drug applications involving adamantane moieties.[115]

Negligible cell internalization of radioligands

Neither of the studied ferrocene or adamantane based ligands (**16**, **19**) showed any cell internalization or cell membrane binding. (**Figure 17**) For compounds designed to act as a radioligand of a pretargeting strategy, non-internalization limits their use in certain antibody based pretargeting applications. **16** and **19** can only be utilized in pretargeting schemes that involve the use of non-internalizing or slowly internalizing antibodies. So far none of the existing pretargeting platforms have been designed specifically for internalizing antibodies and based on preclinical studies, pretargeting with internalizing antibodies results in very modest target accumulation of the radioligand due to its limited access to the internalized antibody. To potentially alter the internalization rate of the guest radioligands, adjusting the zero charge of **16** and **19** to a positive one, could increase the internalization of both compounds. In general for small molecules internalization often occurs *via* diffusion hence molecules with lower polarity are more likely to permeate the phospholipid bilayer membrane. However, compounds with a positive charge have shown to have increased permeability.[116]

6.2 COMPARISON OF THE PRETARGETED RADIOLIGANDS *IN VIVO*

In the development of the host-guest chemistry based pretargeting platform for PET, two main characteristics were used to evaluate the performance of each radioligands for *in vivo* pretargeting: the overall tumor uptake over time and the radioligand's clearance time from non-target tissue. In general, in all PET imaging, tumor-to-background signal is a vital factor in deciding if a PET tracer can provide the desired information on the molecular profile of different tissues. In pretargeted nuclear medicine, where the aim is to reduce the radiation dose of the non-target tissue, not only does the tumor-to-background signal need to be high enough, but the signal from the non-target tissue should be as low as possible.

Four main components were concluded to have an effect on the tumor uptake of the radioligand and its clearance profile: the guest moiety of the radioligand, the radioligand's blood half-life, the lag time used between the antibody and the radioligand injections and finally the amount of administrated antibody.

Guest moiety

With all the studied adamantane based ligands, their build up at the tumor site was higher compared to the ferrocene ligands. This can be concluded from the pretargeting experiments of **16** and **19** which were performed in identical conditions (animal model, antibody and its dosing and scheduling) except in regards to the guest moiety of radioligand (**16**; ferrocene & **19**; adamantane). Pretargeting with **16** reached tumor uptakes of 8 h: 3.1 ± 0.6 %ID/g & 24 h: 1.5 ± 0.5 %ID/g compared to **19**, 8 h: 5.9 ± 1.6 %ID/g & 24 h: 12.0 ± 0.9 ID/g. Based on earlier reports, ferrocene and adamantane guest

molecules separated by a methylene bridge from an adjacent positive charge, a ferrocene guest possess two magnitudes lower association constant to the CB7 cavity compared to an adamantane guest ($K_{Fc}=10^{12.60}$ & $K_{Adma}=10^{14.88}$).[82] (**Table 3**) The difference in the K_a values could partly explain the difference observed in the radioligands' tumor uptake. An additional factor that could have resulted in lower tumor uptake of the ferrocene radioligand was its compromised stability. In its *in vitro* stability studies, hydrophilic degradation products were detected already after few hours. However **19** remained well intact even after 24 h (>90 %). The chemical structure of the degradation products of **16** was not characterized, but potentially the binding of these byproducts to the CB7 cavity might be compromised. In order to confirm this, further *in vivo* stability studies of the **16**-CB7 and **19**-CB7 complexes are needed.

The same trend of lower tumor uptake with ferrocene ligands was also observed with the gallium-68 labeled versions of the ligands, **15** and **21**. In these sets of *in vivo* experiments the pretargeting conditions were identical except in the amount of administered CB7-M5A, which was for the pretargeted **15** and **21** respectively 1.0 and 0.7 nmol. Despite the higher injected dose of CB7-M5A for the ferrocene radioligand (**15**) the tumor uptake at 4 h post injection was lower compared to pretargeted **21** at the same timepoint (2.1 ± 0.6 %ID/g vs. 5.1 ± 0.5 %ID/g). Based on what we have concluded with the CB7-Adma pretargeting studies, higher injected dose of CB7-M5A increases the tumor uptake, presumably due to the expected higher number of available CB7 moieties at the tumor site. (**Figure 35**)

What further bolsters the hypothesis that adamantane ligands formed host-guest complexes more avidly with the CB7 cavity compared to ferrocene ligands is observed in their presence in the blood pool. By comparing again an adamantane and ferrocene

radioligands with similar individual blood half-lives, **16** ($t_{1/2}$=11.0 min) and **19** ($t_{1/2}$=13.8 min), the presence of each radioligand in the blood stream after a 3-day prior CB7-M5A injection varied significantly (at 8 h post injection: **16** (0.2 $\pm$ 0.1 %ID/g) and **19** (1.9 $\pm$ 0.5 %ID/g); p=0.008). Even the adamantane ligand with the shortest individual blood half-life (**20**, $t_{1/2}$=6.3 min) is more abundant in the blood pool (at 8 h p.i. **20** (0.7 $\pm$ 0.2 %ID/g)) compared to **16** with a longer blood half-life. The longer blood pool presence times for **19** and **20** are most likely explained by their binding to the excess, non-target bound CB7-M5A which was still circulating the blood pool.

The adamantane ligands not only possessed higher tumor uptake, but they also remained at the tumor site longer and their tumor uptake increased over time. (**Figure 36**) The opposite trend was experienced with the ferrocene radioligands. (**Figure 32**) Both of the copper-64 ferrocene radioligands **16** and **17** had lower tumor uptake at 24 h p.i. compared to their respective 8 h timepoints, indicating that the some of the CB7 bound ferrocene radioligands disassociated from the cavity over time. However, with the copper-64 adamantane radioligands, **18**-**20**, the tumor uptake increased over time. These trends can also be a result of the differences in the ligands' association constants. Additionally the fact that the adamantane ligands' tumor uptake still increased all the way up to the last monitored timepoint of 24 h is also due to the ligands' longer blood half-life values discussed next.

Blood half-life

With ferrocene and adamantane guest ligands, the blood half-life of the ligands decreased as the length of the PEG-linker increased. (**Table 6**) In turn, the decrease in blood half-

life resulted in decreased tumor uptake, and the difference was observed to be significant. As the ligand's time in the blood pool is reduced, it has less time to get accumulated to the tumor site. Additionally, ligands with longer blood half-lives also have more time to bind to the excess CB7-M5A modified antibody in the blood pool. The adamantane ligand with the shortest blood half-life, **20**: ($t_{1/2}$=6.3 min) had the lowest presence in the blood pool after 24 h p.i. of CB7-M5A out of all the adamantane radioligands. In turn, pretargeted **20** also had the lowest tumor uptake out of all the copper-64-labeled adamantane ligands at all timepoints, since less of the free **20** and CB7-M5A bound **20** accumulated to the target site.

Lag time

One of the major points of interest for the development of the host-guest pretargeting platform was to study how well the system performs with varying lag times. As it has been discussed earlier, due to the long biological half-life of macromolecules in humans, full length antibodies remain in the blood circulation for weeks. Potentially higher target-to-background signal could be reached with extended lag times, since less of the radioligand would bind to the antibody still circulating in the blood pool. The lag times applied in the clinical pretargeting studies has varied between 1-7 days and increasing the lag time has proven to result in lower toxicity, better image quality and decreased red marrow dose.[45] Most preclinical studies are performed with lag times of 1 to 3 days. Few studies exploring longer lag times (5 days) have resulted in decreased tumor uptake due the poor long-term stability of the pretargeting agents.[28,72]

Based on our pretargeting studies with a ferrocene (**16**) and an adamantane guest ligand (**21**) using varying lag times (3-9 days) we observed again that the adamantane ligands performed better compared to the ferrocene radioligands. Three lag times which were explored with pretargeted **16** revealed that the tumor uptake decreased as the lag time was increased from 3 to 6 to 9 days. (**Figure 33**) In turn, this resulted in tumor-to-blood ratios values not changing between the different lag time cohorts. With the pretargeted **21**, the lag time schedule of 3 and 6 days produced the same tumor uptake profile. Excitingly the longer lag time also resulted in reduced presence of the **21** in the blood pool and hence in increased tumor-to-blood ratio. (**Figure 39**)

The fact that the CB7-Adma driven pretargeting performed well with varying lag times and resulted in higher tumor-to-background ratios with longer lag times, indicates that the presented platform would excel without the use of a clearing agent. Clearing agents have been explored in preclinical and clinical studies to shorten the needed and required lag times due to the instability of the pretargeting agents. Since the CB7-M5A can be let naturally clear from the blood pool before the injection of the radioligand, this additional, uninviting step of administrating a third agent, the clearing agent is not needed as part of the CB7-Adma pretargeting strategy.

7. CONCLUSIONS AND FUTURE DIRECTIONS

7.1 CONCLUSIONS

The aim of the presented work was the development of a host-guest chemistry driven pretargeting platform. The study involved the successful development and characterization of sets of ferrocene- and adamantane-based radioligands labeled with gallium-68 or copper-64. The efficacy of the guest radioligands was evaluated with an antibody based pretargeting strategy: A full length antibody M5A was successfully modified to carry a CB7 moiety to allow the host-guest complex formation to occur at the site of the targeted antibody *in vivo*.

All the reported guest radioligands exhibited effective pretargeting of the CB7-M5A in tumor bearing mice. Major improvements in the host-guest pretargeting strategy occurred with the use of adamantane based guest ligands compared to first-generation ferrocene ligands. CB7-Adma driven pretargeting resulted in several times higher tumor uptake and the formed CB7-Adma complexes *in vivo* were more stable which was manifested as long-lasting tumor uptake of the adamantane radioligands. An additional benefit which was noted with adamantane radioligands was their faster excretion through the hepatobiliary system.

One of the major benefits of the CB7-Adma driven pretargeting methodology is that it excels with extended lag times. This unique feature of the host-guest pretargeting methodology has not been established with other pretargeting platforms in the past. This advancement allows to perform pretargeting with flexible radioligand dosing schedules and more importantly potentially decrease even further the radiation burden of

macromolecule based nuclear medicine treatments. Additionally, applying longer lag times eliminates the need to use a clearing agent.

7.2 LIMITATIONS

One of the major concerns of any antibody based pretargeting approach is the internalization of these macromolecules. Most clinically relevant antibodies for cancer treatment express internalization at some rate. Faster internalization of an antibody limits the length of the appropriate lag times, and in turn shorter lag times could diminish the efficacy of pretargeting strategy as the radiation burden decreasing technique. Two clinically relevant internalizing antibodies, trastuzumab and cetuximab, have been investigated for pretargeted strategy in preclinical studies with very minimal success. The main issues have been either non-existent or low tumor uptake of the radioligands.[117-119] Based on the cell internalization studies of **16** and **19**, neither the ferrocene nor the adamantane radioligand expressed any internalization. In order to expand the use of host-guest pretargeting strategy for internalizing antibodies as well, further optimization of the radioligand structure is needed. However recently other approaches to address the internalization of the antibodies have been proposed. These include modulation of the internalizing target antigen with the use of additional agents that alter their internalization rate.[120]

All the investigated radioligands mostly got excreted through the hepatobiliary system, which was observed as presence of the radioligand in the intestine even after several hours post injection of the radioligand. For the copper-64-labeled radioligands, the slow excretion did not present to be an issue, due to the relatively long physical half-life of

copper-64 ($t_{1/2}$=12.7 h) which allowed later imaging timepoints (8, 24 h). The shorter half-life of gallium-68 ($t_{1/2}$=68 min), permitted to perform imaging only up to 4 h p.i., which was not a sufficient time for the non-target bound radioligand to get excreted from the intestine in order to acquire high tumor-to-background ratio. (**Figure 40**) The use of short-lived radionuclides, such as gallium-68 and fluorine-18 ($t_{1/2}$=109 min) for pretargeted PET is ideal from the radiation dose and safety point of view, which is why further optimization of the gallium-68 labeled guest radioligands is needed. Potentially, by directing the excretion to occur through the kidneys by adjusting the molecular charge of the compounds, could enhance the rate of the excretion also. By having a radioligand which would get excreted through the renal system, would also allow a wider use of the approach and to target also cancer tissue located in the abdomen area.

7.3 FUTURE DIRECTIONS

The presented work focused on the development and optimization the host-guest pretargeting strategy through synthesizing a library of guest radioligands and studying their efficacy and *in vivo* profile differences in the pretargeting setting. The optimization of the other pretargeting component, the CB7-modified antibody, was not explored. The CB7-M5A antibody developed for the pretargeting methodology had relatively low number of CB7-moities (~0.8). By increasing the number of CB7 cavities conjugated to the antibody, the tumor uptake of the guest radioligands could potentially be increased. This phenomenon has been reported with other pretargeting methodologies.[121] However, by increasing the number of moieties on the antibody would eventually decrease the

immunoreactivity of the antibody, which is why exploring site-specifically modified antibodies could be beneficial also.

Additionally, it would be valid to study how increasing the number of CB7 moieties on the antibody potentially affect its *in vivo* profile. Due to the relatively large size (~1160 g/mol) and hydrophobicity of the CB7 moiety, formation of hydrophobic antibody aggregates might occur if the number of CB7/antibody is increased too much. Modification of antibodies with other hydrophobic functionalities has reported to lead in build-up of the antibody aggregates in the liver and spleen and result in reduced tumor uptake.[110]

At this point, the efficacy of the host-guest pretargeting approach has been established for pretargeted PET: the formation of stable host-guest complex between the antibody and the radioligand is proven. The next obvious step to explore is the therapeutic application of the methodology. By labeling the adamantane guest radioligand with a beta- (lutetium-177 or copper-67) or an alpha-emitting (actinium-225 or lead-212) therapeutic radionuclide, we could study if the tumor payload of the radioligand is sufficient to result in a therapeutic response. The fractionated dosing approach, which was already recognized as a viable approach with the host-guest pretargeted PET, should also be explored as part of the therapy studies. Importantly these studies would expand the understanding on the stability of the host-guest complex *in vivo*, due to the long physical half-life of some of the suggested therapeutic radionuclides ($t_{1/2}$(^{177}Lu)= 6.6 d, $t_{1/2}$(^{225}Ac)= 9.9 d).

REFERENCES

1.   Kohler G, Milstein C. Continuous cultures of fused cells secreting antibody of predefined specificity. Nature. 1975;256(5517):495-7.

2.   Larson SM, Carrasquillo JA, Reynolds JC. Radioimmunodetection and radioimmunotherapy. Cancer Invest. 1984;2(5):363-81.

3.   Goldenberg DM, DeLand F, Kim E, Bennett S, Primus FJ, van Nagell JR, Jr., et al. Use of radiolabeled antibodies to carcinoembryonic antigen for the detection and localization of diverse cancers by external photoscanning. N Engl J Med. 1978;298(25):1384-6.

4.   Wei W, Rosenkrans ZT, Liu J, Huang G, Luo QY, Cai W. ImmunoPET: Concept, Design, and Applications. Chem Rev. 2020;120(8):3787-851.

5.   Ovacik M, Lin K. Tutorial on Monoclonal Antibody Pharmacokinetics and Its Considerations in Early Development. Clin Transl Sci. 2018;11(6):540-52.

6.   Larson SM, Carrasquillo JA, Cheung NK, Press OW. Radioimmunotherapy of human tumours. Nat Rev Cancer. 2015;15(6):347-60.

7.   Wittrup KD, Thurber GM, Schmidt MM, Rhoden JJ. Practical theoretic guidance for the design of tumor-targeting agents. Methods Enzymol. 2012;503:255-68.

8.   Freise AC, Wu AM. In vivo imaging with antibodies and engineered fragments. Mol Immunol. 2015;67(2 Pt A):142-52.

9.   Scott AM, Akhurst T, Lee FT, Ciprotti M, Davis ID, Weickhardt AJ, et al. First clinical study of a pegylated diabody (124)I-labeled PEG-AVP0458 in patients with tumor-associated glycoprotein 72 positive cancers. Theranostics. 2020;10(25):11404-15.

10.   Price EW, Orvig C. Matching chelators to radiometals for radiopharmaceuticals. Chem Soc Rev. 2014;43(1):260-90.

11.   Adumeau P, Sharma SK, Brent C, Zeglis BM. Site-Specifically Labeled Immunoconjugates for Molecular Imaging--Part 1: Cysteine Residues and Glycans. Mol Imaging Biol. 2016;18(1):1-17.

12.   Adumeau P, Sharma SK, Brent C, Zeglis BM. Site-Specifically Labeled Immunoconjugates for Molecular Imaging--Part 2: Peptide Tags and Unnatural Amino Acids. Mol Imaging Biol. 2016;18(2):153-65.

13.   Cook BE, Adumeau P, Membreno R, Carnazza KE, Brand C, Reiner T, et al. Pretargeted PET Imaging Using a Site-Specifically Labeled Immunoconjugate. Bioconjug Chem. 2016;27(8):1789-95.

14.   Adumeau P, Davydova M, Zeglis BM. Thiol-Reactive Bifunctional Chelators for the Creation of Site-Selectively Modified Radioimmunoconjugates with Improved Stability. Bioconjug Chem. 2018;29(4):1364-72.

15.   Vivier D, Fung K, Rodriguez C, Adumeau P, Ulaner GA, Lewis JS, et al. The Influence of Glycans-Specific Bioconjugation on the FcgammaRI Binding and In vivo Performance of (89)Zr-DFO-Pertuzumab. Theranostics. 2020;10(4):1746-57.

16.   Pringle TA, Chan CD, Luli S, Blair HJ, Rankin KS, Knight JC. Synthesis and In Vivo Evaluation of a Site-specifically Labeled Radioimmunoconjugate for Dual-Modal (PET/NIRF) Imaging of MT1-MMP in Sarcomas. Bioconjug Chem. 2022;33(8):1564-73.

17.   Poty S, Francesconi LC, McDevitt MR, Morris MJ, Lewis JS. alpha-Emitters for Radiotherapy: From Basic Radiochemistry to Clinical Studies-Part 1. J Nucl Med. 2018;59(6):878-84.

18.   Poty S, Membreno R, Glaser JM, Ragupathi A, Scholz WW, Zeglis BM, et al. The inverse electron-demand Diels-Alder reaction as a new methodology for the synthesis of (225)Ac-labelled radioimmunoconjugates. Chem Commun (Camb). 2018;54(21):2599-602.

19.   Manafi-Farid R, Ataeinia B, Ranjbar S, Jamshidi Araghi Z, Moradi MM, Pirich C, et al. ImmunoPET: Antibody-Based PET Imaging in Solid Tumors. Front Med (Lausanne). 2022;9:916693.

20.   Kaur S, Venktaraman G, Jain M, Senapati S, Garg PK, Batra SK. Recent trends in antibody-based oncologic imaging. Cancer Lett. 2012;315(2):97-111.

21.   Reardon DA, Akabani G, Coleman RE, Friedman AH, Friedman HS, Herndon JE, 2nd, et al. Salvage radioimmunotherapy with murine iodine-131-labeled antitenascin monoclonal antibody 81C6 for patients with recurrent primary and metastatic malignant brain tumors: phase II study results. J Clin Oncol. 2006;24(1):115-22.

22.   Reardon DA, Zalutsky MR, Akabani G, Coleman RE, Friedman AH, Herndon JE, 2nd, et al. A pilot study: 131I-antitenascin monoclonal antibody 81c6 to deliver a 44-Gy resection cavity boost. Neuro Oncol. 2008;10(2):182-9.

23.   Kaplon H, Muralidharan M, Schneider Z, Reichert JM. Antibodies to watch in 2020. MAbs. 2020;12(1):1703531.

24.   Schaefer NG, Ma J, Huang P, Buchanan J, Wahl RL. Radioimmunotherapy in non-Hodgkin lymphoma: opinions of U.S. medical oncologists and hematologists. J Nucl Med. 2010;51(6):987-94.

25.   Altai M, Membreno R, Cook B, Tolmachev V, Zeglis BM. Pretargeted Imaging and Therapy. J Nucl Med. 2017;58(10):1553-9.

26.   Bailly C, Bodet-Milin C, Rousseau C, Faivre-Chauvet A, Kraeber-Bodere F, Barbet J. Pretargeting for imaging and therapy in oncological nuclear medicine. EJNMMI Radiopharm Chem. 2017;2(1):6.

27.   Jallinoja V, Houghton JL. Current Landscape in Clinical Pretargeted Radioimmunoimaging and Therapy. J Nucl Med. 2021.

28.   Houghton JL, Zeglis BM, Abdel-Atti D, Sawada R, Scholz WW, Lewis JS. Pretargeted Immuno-PET of Pancreatic Cancer: Overcoming Circulating Antigen and Internalized Antibody to Reduce Radiation Doses. J Nucl Med. 2016;57(3):453-9.

29.   Membreno R, Cook BE, Fung K, Lewis JS, Zeglis BM. Click-Mediated Pretargeted Radioimmunotherapy of Colorectal Carcinoma. Mol Pharm. 2018;15(4):1729-34.

30.   Jallinoja VIJ, Carney BD, Bhatt K, Abbriano CH, Schlyer DJ, Yazaki PJ, et al. Investigation of Copper-64-Based Host-Guest Chemistry Pretargeted Positron Emission Tomography. Mol Pharm. 2022.

31.   Kraeber-Bodere F, Faivre-Chauvet A, Ferrer L, Vuillez JP, Brard PY, Rousseau C, et al. Pharmacokinetics and dosimetry studies for optimization of anti-carcinoembryonic antigen x anti-hapten bispecific antibody-mediated pretargeting of Iodine-131-labeled hapten in a phase I radioimmunotherapy trial. Clin Cancer Res. 2003;9(10 Pt 2):3973S-81S.

32.   Grana C, Chinol M, Robertson C, Mazzetta C, Bartolomei M, De Cicco C, et al. Pretargeted adjuvant radioimmunotherapy with yttrium-90-biotin in malignant glioma patients: a pilot study. Br J Cancer. 2002;86(2):207-12.

33.   Chandler CS, Bell MM, Chung SK, Veach DR, Fung EK, Punzalan B, et al. Intraperitoneal Pretargeted Radioimmunotherapy for Colorectal Peritoneal Carcinomatosis. Mol Cancer Ther. 2022;21(1):125-37.

34.   Rossin R, Lappchen T, van den Bosch SM, Laforest R, Robillard MS. Diels-Alder reaction for tumor pretargeting: in vivo chemistry can boost tumor radiation dose compared with directly labeled antibody. J Nucl Med. 2013;54(11):1989-95.

35.   Meyer JP, Tully KM, Jackson J, Dilling TR, Reiner T, Lewis JS. Bioorthogonal Masking of Circulating Antibody-TCO Groups Using Tetrazine-Functionalized Dextran Polymers. Bioconjug Chem. 2018;29(2):538-45.

36.   Reardan DT, Meares CF, Goodwin DA, McTigue M, David GS, Stone MR, et al. Antibodies against metal chelates. Nature. 1985;316(6025):265-8.

37.   Salaun PY, Campion L, Bournaud C, Faivre-Chauvet A, Vuillez JP, Taieb D, et al. Phase II trial of anticarcinoembryonic antigen pretargeted radioimmunotherapy in progressive metastatic medullary thyroid carcinoma: biomarker response and survival improvement. J Nucl Med. 2012;53(8):1185-92.

38.   Cheal SM, Xu H, Guo HF, Zanzonico PB, Larson SM, Cheung NK. Preclinical evaluation of multistep targeting of diasialoganglioside GD2 using an IgG-scFv bispecific antibody with high affinity for GD2 and DOTA metal complex. Mol Cancer Ther. 2014;13(7):1803-12.

39.   Bodet-Milin C, Faivre-Chauvet A, Carlier T, Rauscher A, Bourgeois M, Cerato E, et al. Immuno-PET Using Anticarcinoembryonic Antigen Bispecific Antibody and 68Ga-Labeled Peptide in Metastatic Medullary Thyroid Carcinoma: Clinical Optimization of the Pretargeting Parameters in a First-in-Human Trial. J Nucl Med. 2016;57(10):1505-11.

40.   Touchefeu Y, Bailly C, Frampas E, Eugene T, Rousseau C, Bourgeois M, et al. Promising clinical performance of pretargeted immuno-PET with anti-CEA bispecific antibody and gallium-68-labelled IMP-288 peptide for imaging colorectal cancer metastases: a pilot study. Eur J Nucl Med Mol Imaging. 2020.

41.   Cheal SM, McDevitt MR, Santich BH, Patel M, Yang G, Fung EK, et al. Alpha radioimmunotherapy using (225)Ac-proteus-DOTA for solid tumors - safety at curative doses. Theranostics. 2020;10(25):11359-75.

42.   Orcutt KD, Slusarczyk AL, Cieslewicz M, Ruiz-Yi B, Bhushan KR, Frangioni JV, et al. Engineering an antibody with picomolar affinity to DOTA chelates of multiple radionuclides for pretargeted radioimmunotherapy and imaging. Nucl Med Biol. 2011;38(2):223-33.

43.   Bodet-Milin C, Ferrer L, Rauscher A, Masson D, Rbah-Vidal L, Faivre-Chauvet A, et al. Pharmacokinetics and Dosimetry Studies for Optimization of Pretargeted Radioimmunotherapy in CEA-Expressing Advanced Lung Cancer Patients. Front Med (Lausanne). 2015;2:84.

44.   Schoffelen R, Boerman OC, Goldenberg DM, Sharkey RM, van Herpen CM, Franssen GM, et al. Development of an imaging-guided CEA-pretargeted radionuclide treatment of advanced colorectal cancer: first clinical results. Br J Cancer. 2013;109(4):934-42.

45.   Schoffelen R, Woliner-van der Weg W, Visser EP, Goldenberg DM, Sharkey RM, McBride WJ, et al. Predictive patient-specific dosimetry and individualized dosing of pretargeted radioimmunotherapy in patients with advanced colorectal cancer. Eur J Nucl Med Mol Imaging. 2014;41(8):1593-602.

46.   Rousseau C, Goldenberg DM, Colombie M, Sebille JC, Meingan P, Ferrer L, et al. Initial Clinical Results of a Novel Immuno-PET Theranostic Probe in Human Epidermal Growth Factor Receptor 2-Negative Breast Cancer. J Nucl Med. 2020;61(8):1205-11.

47.   Labrijn AF, Janmaat ML, Reichert JM, Parren P. Bispecific antibodies: a mechanistic review of the pipeline. Nat Rev Drug Discov. 2019;18(8):585-608.

48.   Hnatowich DJ, Virzi F, Rusckowski M. Investigations of avidin and biotin for imaging applications. J Nucl Med. 1987;28(8):1294-302.

49.   Knox SJ, Goris ML, Tempero M, Weiden PL, Gentner L, Breitz H, et al. Phase II trial of yttrium-90-DOTA-biotin pretargeted by NR-LU-10 antibody/streptavidin in patients with metastatic colon cancer. Clin Cancer Res. 2000;6(2):406-14.

50.   Weiden PL, Breitz HB. Pretargeted radioimmunotherapy (PRIT) for treatment of non-Hodgkin's lymphoma (NHL). Crit Rev Oncol Hematol. 2001;40(1):37-51.

51.   Breitz HB, Weiden PL, Beaumier PL, Axworthy DB, Seiler C, Su FM, et al. Clinical optimization of pretargeted radioimmunotherapy with antibody-streptavidin conjugate and 90Y-DOTA-biotin. J Nucl Med. 2000;41(1):131-40.

52.   Paganelli G, Grana C, Chinol M, Cremonesi M, De Cicco C, De Braud F, et al. Antibody-guided three-step therapy for high grade glioma with yttrium-90 biotin. Eur J Nucl Med. 1999;26(4):348-57.

53.   Cremonesi M, Ferrari M, Chinol M, Stabin MG, Grana C, Prisco G, et al. Three-step radioimmunotherapy with yttrium-90 biotin: dosimetry and pharmacokinetics in cancer patients. Eur J Nucl Med. 1999;26(2):110-20.

54. Kalofonos HP, Rusckowski M, Siebecker DA, Sivolapenko GB, Snook D, Lavender JP, et al. Imaging of tumor in patients with indium-111-labeled biotin and streptavidin-conjugated antibodies: preliminary communication. J Nucl Med. 1990;31(11):1791-6.

55. Le Doussal JM, Chetanneau A, Gruaz-Guyon A, Martin M, Gautherot E, Lehur PA, et al. Bispecific monoclonal antibody-mediated targeting of an indium-111-labeled DTPA dimer to primary colorectal tumors: pharmacokinetics, biodistribution, scintigraphy and immune response. J Nucl Med. 1993;34(10):1662-71.

56. Paganelli G, Magnani P, Zito F, Villa E, Sudati F, Lopalco L, et al. Three-step monoclonal antibody tumor targeting in carcinoembryonic antigen-positive patients. Cancer Res. 1991;51(21):5960-6.

57. Forero A, Weiden PL, Vose JM, Knox SJ, LoBuglio AF, Hankins J, et al. Phase 1 trial of a novel anti-CD20 fusion protein in pretargeted radioimmunotherapy for B-cell non-Hodgkin lymphoma. Blood. 2004;104(1):227-36.

58. Paganelli G, Bartolomei M, Ferrari M, Cremonesi M, Broggi G, Maira G, et al. Pre-targeted locoregional radioimmunotherapy with 90Y-biotin in glioma patients: phase I study and preliminary therapeutic results. Cancer Biother Radiopharm. 2001;16(3):227-35.

59. Shen S, Forero A, LoBuglio AF, Breitz H, Khazaeli MB, Fisher DR, et al. Patient-specific dosimetry of pretargeted radioimmunotherapy using CC49 fusion protein in patients with gastrointestinal malignancies. J Nucl Med. 2005;46(4):642-51.

60. Kuijpers WH, Bos ES, Kaspersen FM, Veeneman GH, van Boeckel CA. Specific recognition of antibody-oligonucleotide conjugates by radiolabeled antisense nucleotides:

a novel approach for two-step radioimmunotherapy of cancer. Bioconjug Chem. 1993;4(1):94-102.

61. Oroujeni M, Tano H, Vorobyeva A, Liu Y, Vorontsova O, Xu T, et al. Affibody-mediated PNA-based pretargeted co-treatment improves survival of trastuzumab-treated mice bearing HER2-expressing xenografts. J Nucl Med. 2021.

62. Tano H, Oroujeni M, Vorobyeva A, Westerlund K, Liu Y, Xu T, et al. Comparative Evaluation of Novel (177)Lu-Labeled PNA Probes for Affibody-Mediated PNA-Based Pretargeting. Cancers (Basel). 2021;13(3).

63. Honarvar H, Westerlund K, Altai M, Sandstrom M, Orlova A, Tolmachev V, et al. Feasibility of Affibody Molecule-Based PNA-Mediated Radionuclide Pretargeting of Malignant Tumors. Theranostics. 2016;6(1):93-103.

64. Westerlund K, Vorobyeva A, Mitran B, Orlova A, Tolmachev V, Karlstrom AE, et al. Site-specific conjugation of recognition tags to trastuzumab for peptide nucleic acid-mediated radionuclide HER2 pretargeting. Biomaterials. 2019;203:73-85.

65. Liu G, Dou S, Baker S, Akalin A, Cheng D, Chen L, et al. A preclinical 188Re tumor therapeutic investigation using MORF/cMORF pretargeting and an antiTAG-72 antibody CC49. Cancer Biol Ther. 2010;10(8):767-74.

66. Liu G, He J, Dou S, Gupta S, Vanderheyden JL, Rusckowski M, et al. Pretargeting in tumored mice with radiolabeled morpholino oligomer showing low kidney uptake. Eur J Nucl Med Mol Imaging. 2004;31(3):417-24.

67. Rossin R, Verkerk PR, van den Bosch SM, Vulders RC, Verel I, Lub J, et al. In vivo chemistry for pretargeted tumor imaging in live mice. Angew Chem Int Ed Engl. 2010;49(19):3375-8.

68.   Reiner T, Zeglis BM. The inverse electron demand Diels-Alder click reaction in radiochemistry. J Labelled Comp Radiopharm. 2014;57(4):285-90.

69.   Zeng D, Zeglis BM, Lewis JS, Anderson CJ. The growing impact of bioorthogonal click chemistry on the development of radiopharmaceuticals. J Nucl Med. 2013;54(6):829-32.

70.   Vugts DJ, Vervoort A, Stigter-van Walsum M, Visser GW, Robillard MS, Versteegen RM, et al. Synthesis of phosphine and antibody-azide probes for in vivo Staudinger ligation in a pretargeted imaging and therapy approach. Bioconjug Chem. 2011;22(10):2072-81.

71.   Qiu L, Tan H, Lin Q, Si Z, Mao W, Wang T, et al. A Pretargeted Imaging Strategy for Immune Checkpoint Ligand PD-L1 Expression in Tumor Based on Bioorthogonal Diels-Alder Click Chemistry. Mol Imaging Biol. 2020;22(4):842-53.

72.   Zeglis BM, Brand C, Abdel-Atti D, Carnazza KE, Cook BE, Carlin S, et al. Optimization of a Pretargeted Strategy for the PET Imaging of Colorectal Carcinoma via the Modulation of Radioligand Pharmacokinetics. Mol Pharm. 2015;12(10):3575-87.

73.   Meyer JP, Kozlowski P, Jackson J, Cunanan KM, Adumeau P, Dilling TR, et al. Exploring Structural Parameters for Pretargeting Radioligand Optimization. J Med Chem. 2017;60(19):8201-17.

74.   Poty S, Carter LM, Mandleywala K, Membreno R, Abdel-Atti D, Ragupathi A, et al. Leveraging Bioorthogonal Click Chemistry to Improve (225)Ac-Radioimmunotherapy of Pancreatic Ductal Adenocarcinoma. Clin Cancer Res. 2019;25(2):868-80.

75. Membreno R, Keinanen OM, Cook BE, Tully KM, Fung KC, Lewis JS, et al. Toward the Optimization of Click-Mediated Pretargeted Radioimmunotherapy. Mol Pharm. 2019;16(5):2259-63.

76. Houghton JL, Membreno R, Abdel-Atti D, Cunanan KM, Carlin S, Scholz WW, et al. Establishment of the In Vivo Efficacy of Pretargeted Radioimmunotherapy Utilizing Inverse Electron Demand Diels-Alder Click Chemistry. Mol Cancer Ther. 2017;16(1):124-33.

77. Keinanen O, Fung K, Brennan JM, Zia N, Harris M, van Dam E, et al. Harnessing (64)Cu/(67)Cu for a theranostic approach to pretargeted radioimmunotherapy. Proc Natl Acad Sci U S A. 2020;117(45):28316-27.

78. Keinanen O, Brennan JM, Membreno R, Fung K, Gangangari K, Dayts EJ, et al. Dual Radionuclide Theranostic Pretargeting. Mol Pharm. 2019;16(10):4416-21.

79. Cook BE, Archbold J, Nasr K, Girmay S, Goldstein SI, Li P, et al. Non-invasive Imaging of Antisense Oligonucleotides in the Brain via In Vivo Click Chemistry. Mol Imaging Biol. 2022.

80. Rossin R, van den Bosch SM, ten Hoeve W, Carvelli M, Versteegen RM, Lub J, et al. Highly Reactive trans-Cyclooctene Tags with Improved Stability for Diels–Alder Chemistry in Living Systems. Bioconjugate Chemistry. 2013;24(7):1210-7.

81. Rossin R, van Duijnhoven SM, Lappchen T, van den Bosch SM, Robillard MS. Trans-cyclooctene tag with improved properties for tumor pretargeting with the diels-alder reaction. Mol Pharm. 2014;11(9):3090-6.

82. Barrow SJ, Kasera S, Rowland MJ, del Barrio J, Scherman OA. Cucurbituril-Based Molecular Recognition. Chem Rev. 2015;115(22):12320-406.

83.   Li Q, Qiu SC, Zhang J, Chen K, Huang Y, Xiao X, et al. Twisted Cucurbit[n]urils. Org Lett. 2016;18(16):4020-3.

84.   Buschmann HJ, Cleve E, Jansen K, Wego A, Schollmeyer E. Complex Formation between Cucurbit[n]urils and Alkali, Alkaline Earth and Ammonium Ions in Aqueous Solution. Journal of inclusion phenomena and macrocyclic chemistry. 2001;40(1):117-20.

85.   Kim S-Y, Jung I-S, Lee E, Kim J, Sakamoto S, Yamaguchi K, et al. Macrocycles within Macrocycles: Cyclen, Cyclam, and Their Transition Metal Complexes Encapsulated in Cucurbit[8]uril. Angewandte Chemie International Edition. 2001;40(11):2119-21.

86.   Isaacs L. Cucurbit[n]urils: from mechanism to structure and function. Chem Commun (Camb). 2009(6):619-29.

87.   Lagona J, Mukhopadhyay P, Chakrabarti S, Isaacs L. The cucurbit[n]uril family. Angew Chem Int Ed Engl. 2005;44(31):4844-70.

88.   Shetty D, Khedkar JK, Park KM, Kim K. Can we beat the biotin-avidin pair?: cucurbit[7]uril-based ultrahigh affinity host-guest complexes and their applications. Chem Soc Rev. 2015;44(23):8747-61.

89.   Rekharsky MV, Mori T, Yang C, Ko YH, Selvapalam N, Kim H, et al. A synthetic host-guest system achieves avidin-biotin affinity by overcoming enthalpy-entropy compensation. Proc Natl Acad Sci U S A. 2007;104(52):20737-42.

90.   Cao L, Sekutor M, Zavalij PY, Mlinaric-Majerski K, Glaser R, Isaacs L. Cucurbit[7]urilguest pair with an attomolar dissociation constant. Angew Chem Int Ed Engl. 2014;53(4):988-93.

91.   Lee JW, Samal S, Selvapalam N, Kim HJ, Kim K. Cucurbituril homologues and derivatives: new opportunities in supramolecular chemistry. Acc Chem Res. 2003;36(8):621-30.

92.   Das D, Assaf KI, Nau WM. Applications of Cucurbiturils in Medicinal Chemistry and Chemical Biology. Front Chem. 2019;7:619.

93.   Lazar AI, Biedermann F, Mustafina KR, Assaf KI, Hennig A, Nau WM. Nanomolar Binding of Steroids to Cucurbit[n]urils: Selectivity and Applications. J Am Chem Soc. 2016;138(39):13022-9.

94.   Ma D, Hettiarachchi G, Nguyen D, Zhang B, Wittenberg JB, Zavalij PY, et al. Acyclic cucurbit[n]uril molecular containers enhance the solubility and bioactivity of poorly soluble pharmaceuticals. Nat Chem. 2012;4(6):503-10.

95.   Walker S, Oun R, McInnes FJ, Wheate NJ. The Potential of Cucurbit[n]urils in Drug Delivery. Israel Journal of Chemistry. 2011;51(5-6):616-24.

96.   Saleh N, Koner AL, Nau WM. Activation and stabilization of drugs by supramolecular pKa shifts: drug-delivery applications tailored for cucurbiturils. Angew Chem Int Ed Engl. 2008;47(29):5398-401.

97.   Marquez C, Nau WM. Two Mechanisms of Slow Host-Guest Complexation between Cucurbit[6]uril and Cyclohexylmethylamine: pH-Responsive Supramolecular Kinetics. Angew Chem Int Ed Engl. 2001;40(17):3155-60.

98.   Park KM, Suh K, Jung H, Lee DW, Ahn Y, Kim J, et al. Cucurbituril-based nanoparticles: a new efficient vehicle for targeted intracellular delivery of hydrophobic drugs. Chem Commun (Camb). 2009(1):71-3.

99.   Chen H, Chen Y, Wu H, Xu JF, Sun Z, Zhang X. Supramolecular polymeric chemotherapy based on cucurbit[7]uril-PEG copolymer. Biomaterials. 2018;178:697-705.

100.   Wheate NJ. Improving platinum(II)-based anticancer drug delivery using cucurbit[n]urils. J Inorg Biochem. 2008;102(12):2060-6.

101.   Reedijk J. Why does Cisplatin reach Guanine-n7 with competing s-donor ligands available in the cell? Chem Rev. 1999;99(9):2499-510.

102.   Wheate NJ, Day AI, Blanch RJ, Arnold AP, Cullinane C, Collins JG. Multi-nuclear platinum complexes encapsulated in cucurbit[n]uril as an approach to reduce toxicity in cancer treatment. Chem Commun (Camb). 2004(12):1424-5.

103.   Jeon YJ, Kim SY, Ko YH, Sakamoto S, Yamaguchi K, Kim K. Novel molecular drug carrier: encapsulation of oxaliplatin in cucurbit[7]uril and its effects on stability and reactivity of the drug. Org Biomol Chem. 2005;3(11):2122-5.

104.   Uzunova VD, Cullinane C, Brix K, Nau WM, Day AI. Toxicity of cucurbit[7]uril and cucurbit[8]uril: an exploratory in vitro and in vivo study. Org Biomol Chem. 2010;8(9):2037-42.

105.   Hettiarachchi G, Nguyen D, Wu J, Lucas D, Ma D, Isaacs L, et al. Toxicology and drug delivery by cucurbit[n]uril type molecular containers. PLoS One. 2010;5(5):e10514.

106.   Lindmo T, Bunn PA, Jr. Determination of the true immunoreactive fraction of monoclonal antibodies after radiolabeling. Methods Enzymol. 1986;121:678-91.

107.   Girgis MD, Olafsen T, Kenanova V, McCabe KE, Wu AM, Tomlinson JS. Targeting CEA in Pancreas Cancer Xenografts with a Mutated scFv-Fc Antibody Fragment. EJNMMI Res. 2011;1(1):24.

108.　Stabin MG, Sparks RB, Crowe E. OLINDA/EXM: the second-generation personal computer software for internal dose assessment in nuclear medicine. J Nucl Med. 2005;46(6):1023-7.

109.　Daum S, Toms J, Reshetnikov V, Ozkan HG, Hampel F, Maschauer S, et al. Identification of Boronic Acid Derivatives as an Active Form of N-Alkylaminoferrocene-Based Anticancer Prodrugs and Their Radiolabeling with (18)F. Bioconjug Chem. 2019;30(4):1077-86.

110.　Sharma SK, Glaser JM, Edwards KJ, Khozeimeh Sarbisheh E, Salih AK, Lewis JS, et al. A Systematic Evaluation of Antibody Modification and (89)Zr-Radiolabeling for Optimized Immuno-PET. Bioconjug Chem. 2021;32(7):1177-91.

111.　Boonstra MC, Tolner B, Schaafsma BE, Boogerd LS, Prevoo HA, Bhavsar G, et al. Preclinical evaluation of a novel CEA-targeting near-infrared fluorescent tracer delineating colorectal and pancreatic tumors. Int J Cancer. 2015;137(8):1910-20.

112.　Houghton JL, Zeglis BM, Abdel-Atti D, Aggeler R, Sawada R, Agnew BJ, et al. Site-specifically labeled CA19.9-targeted immunoconjugates for the PET, NIRF, and multimodal PET/NIRF imaging of pancreatic cancer. Proc Natl Acad Sci U S A. 2015;112(52):15850-5.

113.　Lewis J, Windhorst A, Zeglis B. Radiopharmaceutical Chemistry. 2019. DOI: 10.1007/978-3-319-98947-1.

114.　Ong W, Kaifer AE. Unusual Electrochemical Properties of the Inclusion Complexes of Ferrocenium and Cobaltocenium with Cucurbit[7]uril. Organometallics. 2003;22(21):4181-3.

115.   Wanka L, Iqbal K, Schreiner PR. The lipophilic bullet hits the targets: medicinal chemistry of adamantane derivatives. Chem Rev. 2013;113(5):3516-604.

116.   Mosquera J, Garcia I, Liz-Marzan LM. Cellular Uptake of Nanoparticles versus Small Molecules: A Matter of Size. Acc Chem Res. 2018;51(9):2305-13.

117.   Knight JC, Mosley M, Uyeda HT, Cong M, Fan F, Faulkner S, et al. In Vivo Pretargeted Imaging of HER2 and TAG-72 Expression Using the HaloTag Enzyme. Molecular Pharmaceutics. 2017;14(7):2307-13.

118.   Keinanen O, Fung K, Pourat J, Jallinoja V, Vivier D, Pillarsetty NK, et al. Pretargeting of internalizing trastuzumab and cetuximab with a (18)F-tetrazine tracer in xenograft models. EJNMMI Res. 2017;7(1):95.

119.   Evans HL, Nguyen QD, Carroll LS, Kaliszczak M, Twyman FJ, Spivey AC, et al. A bioorthogonal (68)Ga-labelling strategy for rapid in vivo imaging. Chem Commun (Camb). 2014;50(67):9557-60.

120.   Pereira PMR, Mandleywala K, Ragupathi A, Carter LM, Goos J, Janjigian YY, et al. Temporal Modulation of HER2 Membrane Availability Increases Pertuzumab Uptake and Pretargeted Molecular Imaging of Gastric Tumors. J Nucl Med. 2019;60(11):1569-78.

121.   Cook BE, Membreno R, Zeglis BM. Dendrimer Scaffold for the Amplification of In Vivo Pretargeting Ligations. Bioconjug Chem. 2018;29(8):2734-40.

APPENDIX

<u>Instruments</u>

The HPLC instrument used for the purification of **1-4** was comprised of Gilson a 159 UV-VIS detector, Gilson 322 Pump and Kinetex 5μm EVO C18 100Å LC column 150 × 21.2 mm. Purification of **5-13** was performed on an Agilent HPLC 1260 Infinity II LC System comprised of a 1260 Quat Pump VL, 1260 DAD WR and LabLogic Flow-RAM radio-HPLC Detector equipped with a LabLogic Systems Limited NaI Detector with Luna 5μm C18(2) 100Å LC column 250 × 10 mm (Phenomenex) column detecting absorption at 254 nm. Chemical purity or radiochemical purity of **1-13** and **14**, **16-20** was measured with the same HPLC instrument using an analytical Kinetex 5μm EVO C18 100 Å column, 150 × 4.6 mm (Phenomenex).

Radiochemical purity of **15**, **21** and [89Zr]Zr-DFO-M5A was determined using BioScan AR-2000 radio-TLC scanner. Activity of organ biodistribution, blood half-life, log D, cellular binding assay and cell internalization samples were measured with Hidex Automatic Gamma Counter. Radioactivity of injected doses was measured with CRC-55tR Capintec Inc dose calibrator. All antibody concentration measurements were done with Thermo Scientific Nanodrop One.

High-resolution mass spectrometry for the small molecules was done with Q-Exactive HF (Thermo-Fisher) Orbi-trap mass spectrometer. The DFO conjugated antibody samples were analyzed with Bruker Impact II quadrupole time-of-flight (QTOF, Bruker Daltonics, Billerica). Proton nuclear magnetic resonance spectroscopy was performed either with a 400 or 500 MHz Bruker Avance III instrument.

Chromatography methods

For the purification of **1**-**4** the RP-HPLC method included H_2O (solvent A) and acetonitrile (solvent B) as the mobile phases as part of a gradient method where solvent B percentage was increased from 10 % to 95 % over 12 minutes with 20 mL/min flow rate. The RP-HPLC method used for purification of **5**-**6** involved using 0.1% trifluoroacetic acid (TFA) in H_2O (solvent A) and 0.1% TFA in acetonitrile (solvent B) as part of a gradient increasing solvent B percentage from 5% to 50% over 33 minutes with a 4 mL/min flow rate. As for the RP-HPLC purification method of **7**-**12**, it involved the use of 0.1 % trifluoroacetic acid (TFA) in H_2O (solvent A) and 0.1 % TFA in acetonitrile (solvent A), where % solvent B remained at 5 for the first minute followed by increasing the solvent B % to 95 over a 24 minute gradient with a flow rate of 4 mL/min.

The RP-HPLC method used to determine the chemical purity and radiochemical purity of **1**-**14** and **16**-**20** involved using 0.1% trifluoroacetic acid (TFA) in H_2O (solvent A) and 0.1% TFA in acetonitrile (solvent B) as mobile phases as part of a gradient increasing solvent B percentage from 5% to 95% over 17 minutes with a 1 mL/min flow rate.

The FPLC - size exclusion method used to analyze the purity of the CB7-M5A and DFO-M5A involved the use of PBS7.4 as the only solvent over a 70 minute period with a flow rate of 0.7 mL/min.

The radiochemical purity of **15**, **21** and [^{89}Zr]Zr-DFO-M5A was studied with radio-TLC using iTLC-SG-Glass microfiber chromatography paper and 50 mM ethylenediaminetetraacetic acid (EDTA) as the mobile phase.